
A Lattice QCD study of the ρ resonance and the timelike pion form factor

*Dissertation zur Erlangung des Grades
"Doktor der Naturwissenschaften"
am Fachbereich Physik, Mathematik, Informatik
der Johannes Gutenberg-Universität
in Mainz*

*Felix Benjamin Erben
geboren in Wiesbaden*

Mainz, den 10. September 2018

Felix Benjamin Erben: *A Lattice QCD study of the ρ resonance and the timelike pion form factor*

Tag der Promotionsprüfung: 12. Dezember 2018

Abstract

The ρ resonance with its principal decay into two pions is the subject of many experimental and theoretical investigations. The ρ is the lightest of all vector mesons and has some interesting applications, like giving access to the timelike pion form factor or a contribution to the hadronic vacuum polarisation of the anomalous magnetic moment of the muon, $(g - 2)_\mu$.

In this work we study the ρ resonance using the Lattice formulation of Quantum Chromodynamics (Lattice QCD). Lattice QCD allows us to compute observables at low energies, where perturbation theory does not work due to the large coupling of QCD in this regime. The ρ has become a test piece for the study of resonances in Lattice QCD, which is always a difficult task because in Euclidean space, where Lattice QCD is formulated, we can directly extract only QCD-stable states. Special formalisms are therefore needed which study the impact of a resonance on stable states.

We extract correlator data using state-of-the-art formalisms like Distillation with stochastic Laplacian-Heaviside (LapH) smearing to extract single- and two-meson correlators from the lattice, in a centre-of-mass frame and moving frames with three different total momenta. We then use the variational method in 8 different irreducible representations of those frames and obtain phase-shift information from this spectrum with a Lüscher-type analysis.

Furthermore, we are computing the timelike pion form factor based on the phase-shift information as well as correlators from current operators. We parametrise the form factor using a fit of our data to an Omnès representation of the pion form factor and find that our data is well described both by the 2-subtracted as well as the 3-subtracted version of this representation. This fit allows us to extract the square radius of the pion which we compare to an independent lattice calculation of the spacelike pion form factor, performed on the same lattice ensembles.

We use both the parametrised version of the pion form factor as well as a reconstruction of the light-quark correlator to get two separate estimates of the vector-vector correlator, which we use to constrain the long-time behaviour of $(g - 2)_\mu$. Both methods give consistent results and lower the uncertainty estimate substantially compared to the simpler procedures. Because they do not rely on a fit to the low-energy data they are an independent check of the vector-vector correlator signal.

Zusammenfassung

Die ρ -Resonanz, die erstrangig in zwei Pionen zerfällt, ist das Thema vieler experimenteller sowie theoretischer Studien. Das ρ ist das leichteste aller Vektor-Mesonen hat einige interessante Anwendungen. So kann es verwendet werden, um den zeitartigen Pion-Formfaktor zu berechnen oder einen Beitrag zum anomalen magnetischen Moment des Muon, $(g - 2)_\mu$, zu leisten.

In dieser Arbeit untersuchen wir die ρ -Resonanz mit Hilfe der Gitterformulierung der Quantenchromodynamik (Gitter-QCD). Mit Hilfe der Gitter-QCD können wir Observablen bei niedrigen Energien, wo Störungstheorie aufgrund der großen Kopplung der QCD nicht mehr anwendbar ist, berechnen. Das ρ kann als Referenzsystem für die Untersuchung von Resonanzen in der Gitter-QCD betrachtet werden; eine generell schwierige Aufgabe, da die Gitter-QCD im Euklidischen Raum formuliert ist und nur QCD-stabile Zustände direkt extrahiert werden können. Resonanzen müssen daher mit speziellen Formalismen über ihre Auswirkung auf stabile Zustände untersucht werden.

Wir verwenden moderne Methoden wie die sogenannte *Distillation* und stochastische *Laplacian-Heaviside (LapH)* Schmierung um Ein- und Zwei-Meson-Korrelatoren auf dem Gitter in einem Schwerpunktsystem und drei verschiedenen bewegten Systemen zu extrahieren. Wir verwenden dann die Variationsmethode in acht verschiedenen irreduziblen Darstellungen und erhalten damit Informationen zur Phasenverschiebung mit einer Analyse nach Art des Lüscher-Formalismus.

Weiterhin berechnen wir den zeitartigen Pion-Formfaktor basierend auf dieser Phasenverschiebungsinformation sowie Matrixelemente des elektromagnetischen Stroms. Wir parametrisieren den Formfaktor mit einem Fit unserer Daten an eine Omnès-Darstellung des Pion-Formfaktors und sehen, dass unsere Daten sowohl durch die zweifach als auch durch die dreifach subtrahierte Version dieser Darstellung gut beschrieben werden. Durch diesen Fit können wir den quadratischen Radius des Pions extrahieren, den wir mit den Ergebnissen einer unabhängigen Studie des raumartigen Pion-Formfaktors auf den selben Gitter-Ensembles vergleichen.

Wir verwenden sowohl die parametrisierte Version des Pion-Formfaktors als auch eine Rekonstruktion der Beiträge der leichten Quarks zur Korrelationsfunktion, um zwei verschiedene Abschätzungen des Vektor-Vektor-Korrelators zu erhalten, mit dem wir die Infrarotbeiträge zu $(g - 2)_\mu$ genauer bestimmen. Beide Methoden liefern konsistente Ergebnisse und verringern die Unsicherheitsabschätzung wesentlich, verglichen mit einfacheren Methoden. Da kein Fit an die Niedrigenergie-daten verwendet wird, sind sie auch eine unabhängige Überprüfung des Signals des Vektor-Vektor-Korrelators.

Acknowledgements

We are grateful to our colleagues within the CLS initiative for sharing ensembles. Our calculations were partly performed on the HPC Cluster Clover at the Institute for Nuclear Physics, University of Mainz. We thank Dalibor Djukanovic for technical support. We are grateful for computer time allocated to project HMZ21 on the BG/Q JUQUEEN computer at NIC, Jülich. Thanks also to the Helmholtz-Institut Mainz (HIM) for the financial support during my PhD.

Contents

1	Lattice QCD	3
1.1	Brief introduction to Lattice QCD	6
1.1.1	Discretisation of Euclidean space time	7
1.1.2	The path integral	14
1.2	CLS gauge configurations	16
1.3	Setting the scale	17
1.4	Uncertainty estimate using jackknife	18
2	Hadron spectroscopy	21
2.1	The variational method	22
2.2	Distillation	25
2.3	Stochastic LapH	28
3	Phenomenology of the ρ resonance	35
3.1	Explicit construction of correlation functions	36
3.2	Moving frames and irreducible representations	39
3.3	Lüscher's finite volume method	41
3.4	Explicit formulae for $\pi\pi$ scattering	45
4	Numerical analysis of the spectrum	49
4.1	The pion mass	49
4.2	Energy spectrum from the GEVP	54
4.2.1	Fixed- t_0 method	54
4.2.2	Window method	55
4.3	Phase-shift analysis	62
4.4	Matrix elements $ A_\Psi $	68
5	Applications	73
5.1	Timelike pion form factor	73
5.2	Hadronic vacuum polarisation	82
6	Conclusions	91

A Full energy spectrum	93
A.1 t_{\min} dependence of the fit	93
A.2 Energy spectrum	100
B Ratios	107
C Derivatives	119
D F_π and a_μ^{hvp} in the fixed-t_0 method	123
E Next steps	129
E.1 Computation on a more chiral ensemble	129
E.2 Analysis for more chiral ensembles	130

Introduction

In this thesis we study $\pi\pi$ scattering in the $\rho \rightarrow \pi\pi$, isospin = 1 scattering channel numerically using Lattice Quantum Chromodynamics (Lattice QCD).

Lattice QCD allows to simulate QCD, the theory of the strong force acting between quarks and gluons, in a regularised way on a finitely-sized 4D Euclidean spacetime grid. Because the coupling of QCD is large in the hadronic regime, Lattice QCD serves as an ideal tool to study the properties like masses and decays of hadrons, i.e. for hadron spectroscopy. One interesting aspect of hadron spectroscopy is the study of resonances, which is possible by exploiting the finiteness of the lattice as a tool to map the finite-volume energy spectrum to the infinite-volume resonance scattering information [1,2].

The ρ resonance is interesting, because it can be related to the timelike pion form factor [3], and because it can help to constrain the long-time behaviour of the hadronic vacuum polarisation (HVP) in the anomalous magnetic moment of the muon, $(g - 2)_\mu$. This quantity can be both measured experimentally as well as calculated theoretically to very high precision, with a current tension between the two values of about 3σ [4]. As such, this quantity is a candidate which could point towards new physics beyond the standard model and a very interesting topic of current research.

With the almost exclusive decay channel into two pions [5], the ρ also serves as an ideal starting point to set up the intricate machinery needed to study resonances on the lattice. Another reason why the ρ resonance is of great interest to be studied precisely is that for any kind of process which has the ρ as a final or intermediate state, precise information about two-pion scattering is important. In other words, if one wants to continue and study more complicated resonances using Lattice QCD, there is no way around studying the ρ first.

For all these reasons, the ρ has been subject of many Lattice QCD studies already [6–14]. A recent review of the development of these studies and the spectroscopy of resonances in general can be found in [15].

Resonances have only been subject of comparably recent hadron spectroscopy studies because they are a lot more difficult to analyse than QCD-bound states. In the case of $\pi\pi$ scattering, one of the main reasons for that is that the computation of energy levels of states which include multi-hadron operators is difficult. Only recent developments in this field have rendered the efficient and

precise computation of their energy spectra within Lattice QCD possible. We are using Distillation with the stochastic LapH method [16, 17] to compute our correlation functions.

This thesis is organised as follows: In Chapter 1, we will briefly introduce and motivate Lattice QCD and talk about the CLS ensembles we are using. Chapter 2 will focus on hadron spectroscopy and explain all the technology we need to extract an energy spectrum from correlation functions built from single-meson operators as well as multi-hadron operators, using Distillation and stochastic LapH. The specific setup needed for the $\rho \rightarrow \pi\pi$, isospin= 1 scattering analysis, using a Lüscher-type analysis in several (moving) frames with lattice momenta up to $\mathbf{d}^2 = 3$ will be presented in Chapter 3 and our numerical findings will be shown in Chapter 4. Finally, we will use the scattering information to compute the timelike pion form factor and the long-time contribution to the HVP contribution to $(g - 2)_\mu$ in Chapter 5.

Chapter 1

Lattice QCD

In this thesis we study *hadrons*, composite particles consisting of *quarks* and *gluons*. The fundamental theory which governs the interaction between those quarks and gluons, the so-called *strong force*, is *quantum chromodynamics* (*QCD*). Mathematically, QCD is a Yang-Mills theory (for the gluon part), coupled to fermions (the quarks), i.e. a non-abelian gauge theory, built on the gauge group $SU(3)$. The quarks come in six *flavours* (up, down, strange, charm, bottom, top), carry an electromagnetic charge ($+\frac{2}{3}e$ or $-\frac{1}{3}e$) and transform according to the fundamental representation of $SU(3)$, which is also described by them carrying a strong charge, the so-called *colour charge*. The gluons are the gauge bosons of the strong force, i.e. the particles which mediate its fundamental interaction (analogously to the photons being the gauge bosons of the electromagnetic force). Gluons have zero mass and electromagnetic charge and transform according to the adjoint representation of $SU(3)$.

In the Hamiltonian formulation of continuum QCD, a particle which moves from point y to point x in the time interval τ is described by the *probability amplitude*

$$\langle x|e^{-iH\tau}|y\rangle, \quad (1.1)$$

where H is the Hamilton operator of the system [18]. Equivalently, QCD can be described with the functional integral formalism, based on ideas by Dirac in 1933 [19] but fully developed by Feynman in 1948 [20], who also wrote down the *path integral* for the first time and showed the equivalence to the Hamiltonian formulation:

$$\langle x|e^{-iH\tau}|y\rangle = \int Dx' e^{iS}. \quad (1.2)$$

In here, S is the action, which already shows some connection to statistical mechanics, where we also have an action which describes a particle moving from y to x along some path parametrised by $x(\tau)$. Dx' is an *integration*

measure which integrates along all classical paths, weighted by the action. This concept can also be extended to quantum field theories (like QCD), where we do not have the concept of a classical path any more. Here, the path integral is computed by integrating over the measure $D[\Psi, \bar{\Psi}, A]$, which integrates over all configuration of quark fields $\Psi, \bar{\Psi}$ and gluon fields A . To formulate the correct path integral for QCD, we first have a look at the Lagrangian density,

$$\mathcal{L}(x) = \sum_{f=1}^{N_f} \bar{\Psi}^{(f)}(x) (\gamma_\mu (\partial_\mu + iA_\mu(x)) + m^{(f)}) \Psi^{(f)}(x) + \frac{1}{2g^2} \text{Tr}[F_{\mu\nu}(x)F_{\mu\nu}(x)], \quad (1.3)$$

where $\Psi^{(f)}$ is the field of a quark with flavour f and mass $m^{(f)}$ and $\bar{\Psi}^{(f)}$ is the field of the respective anti-quark; A_μ is the gluon field, g is the (bare) coupling constant and $F_{\mu\nu}$ the field-strength tensor, which arises from QCD being a Yang-Mills theory. In principle, the quark fields should be written $\Psi_{a,\alpha}^{(f)}$ and the gluon fields $A_{\mu,c,d}$ with the Dirac indices α, β, \dots and the colour indices c, d, \dots explicitly spelled out. For brevity, we are omitting them in this chapter. The QCD continuum action can be read off right from this Lagrangian,

$$S_{\text{QCD}}[\bar{\Psi}, \Psi] = \int d^4x \mathcal{L}(x) = S_F[\bar{\Psi}, \Psi] + S_G, \quad (1.4)$$

where S_G is the gauge action and $S_F[\bar{\Psi}, \Psi]$ denotes the fermionic (quark) part which contains the coupling between quarks and gluons. At first, we only look at the fermionic part:

$$S_F = \sum_{f=1}^{N_f} \int d^4x \bar{\Psi}^{(f)}(x) (\gamma_\mu (\partial_\mu + iA_\mu(x)) + m^{(f)}) \Psi^{(f)}(x). \quad (1.5)$$

One obvious feature of this action is that it is a sum over the actions of each quark flavour f . The only difference in these actions are the respective quark masses $m^{(f)}$ of the quark flavours f . Through the other parts of the action the quark flavour does not determine how the quark couples to the gluon field $A_\mu(x)$. The full QCD action also has a gluonic part which looks like:

$$S_G = \frac{1}{2g^2} \int d^4x \text{Tr}[F_{\mu\nu}(x)F_{\mu\nu}(x)]. \quad (1.6)$$

The field-strength tensor

$$F_{\mu\nu}(x) = \partial_\mu A_\nu - \partial_\nu A_\mu + [A_\mu, A_\nu] \quad (1.7)$$

and in particular the non-vanishing commutator $[A_\mu, A_\nu]$ are responsible for terms $\mathcal{O}(A^3)$ and $\mathcal{O}(A^4)$ in the action, i.e. interactions of 3 or 4 gluon fields,

respectively. This self-interaction of the gluons can be visualised in a Feynman diagram as a vertex of 3 or 4 gluons, as shown in Figure 1.1.

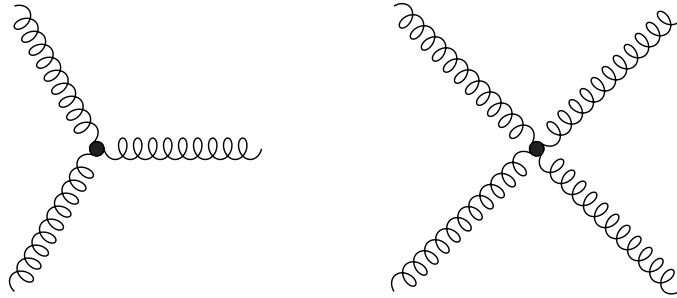


Figure 1.1: Feynman diagrams of the three-gluon and four-gluon vertices describing the gluon self-interaction appearing in the QCD action.

Often, the notation of the QCD Lagrangian or action is shortened a bit further by introducing the covariant derivative,

$$D_\mu \equiv \partial_\mu + iA_\mu(x), \quad (1.8)$$

which couples both to quarks and gluons.

One feature of QCD is the *running coupling*, which means that the coupling constant g changes with the energy of the system. At high energies or short distances this coupling decreases. This feature of QCD is called *asymptotic freedom* [21]. In this region it is possible to reliably extract the features of QCD using a perturbative approach. At lower energies, where g is of a larger order and limits the utility of perturbation theory, quarks and gluons are *confined*, which means that they cannot be observed as individual particles but only in the form of composite particles such as hadrons. Hadrons formed out of a quark and an antiquark ($\bar{q}q$) are called *mesons* and hadrons consisting of three quarks (qqq) are called *baryons*. From a theory point of view there is no argument why other exotic hadrons, consisting of more than 3 quarks, should not exist, as long as they are in a color-singlet state. In current research which goes into finding such states, some potential candidates consistent with tetraquark states and pentaquark states have been reported already: In 2015, the LHCb reported the finding of two states consistent with the $P_c^+(4380)$ and $P_c^+(4450)$ pentaquark states to be observed [22]. In 2016, they reported to have observed another state, labelled $X(4140)$, plus three excited states, which cannot be described by a model only including mesons and baryons and thus claimed to be a tetraquark state [23].

1.1 Brief introduction to Lattice QCD

It has been outlined already that the fact that the QCD coupling is large in the hadronic regime prohibits a perturbative treatment. Chiral perturbation theory is a tool which allows to study hadrons at vanishing quark masses (in the *chiral limit*), but it is unclear how the results from this theory would converge to physical parameters. For a rigorous study of hadrons at non-vanishing quark masses, a different tool is needed. One of the most successful tools to date for this endeavour is *Lattice QCD*, first proposed by Kenneth Wilson in 1974. There are three key ideas behind Lattice QCD as a tool to solve QCD [18]:

- Feynman's path integral
- Euclidean formulation of QCD
- A finite space-time lattice

The Euclidean theory is realised via a *Wick rotation* [24], where Minkowski time τ is rotated into Euclidean time t :

$$\tau \rightarrow -it, \quad t > 0. \quad (1.9)$$

The foundations for this Euclidean formulation have been laid out by Dyson [25], Wick, Schwinger [26] and Symanzik [27]. The advantage of the Euclidean path integral is that it is manifestly real, unlike the Minkowski integral, whose exponential e^{iS} oscillates in time τ . Furthermore, an expectation value of an operator A is exponentially damped in the Euclidean formulation,

$$\text{tr}(e^{-Ht}A) = \sum_{n=0}^{\infty} e^{-E_n t} \langle n|A|n \rangle, \quad (1.10)$$

giving access to a tower of expectation values $\langle n|A|n \rangle$ for different energy eigenstates $|n \rangle$ with energy eigenvalue E_n of the Hamiltonian. Because the energies are ordered, $E_0 < E_1 < \dots$, the ground state can be expected to dominate this sum at large Euclidean times t and can be extracted. There are also methods to extract the excited states of the spectrum, which we will explain and use later. The discretisation of the lattice provides a regularisation and makes this Euclidean path integral a well-defined quantity.

In short, Lattice QCD can be described as a regularised theory which replaces Minkowski-space-time by a Euclidean lattice based on the Euclidean path integral formulation of QCD.

The following arguments closely follow the motivations in and notation from [28], but there are several other textbooks on Lattice QCD available as well [18, 29, 30].

1.1.1 Discretisation of Euclidean space time

First of all, we need a discretised version of space time. For obvious technical reasons any numerical calculation can only be performed in a finite volume and thus a very general form of the lattice Λ with a *lattice spacing* a can be written as

$$\Lambda = \{n = (n_0, n_1, n_2, n_3) \mid n_\mu/a = 1, 2, \dots, N_\mu - 1, \mu = 0, 1, 2, 3\}. \quad (1.11)$$

In general one could also define anisotropic lattices with different lattice spacings a_s, a_t in spatial or temporal directions, but for the purpose of this thesis, this is not considered. We also only consider lattices which have a cubic spatial box, i.e. where $N_L \equiv N_1 = N_2 = N_3$, but allow for a different size of the lattice in the temporal direction, $N_T \equiv N_0$. For all practical calculations the size of this lattice has to be finite with a temporal and spatial extent of

$$T = aN_T, L = aN_L. \quad (1.12)$$

Quark fields $\psi_{\alpha a}(n)$ (and anti-quark fields $\bar{\psi}_{\alpha a}(n)$) in the form of spinors can now be placed on each lattice site n , one for each color-index a and one for each Dirac-index α . Usually, (anti-)periodic boundary conditions are imposed upon them

$$\psi(n + aN_\mu e_\mu) = \pm \psi(n). \quad (1.13)$$

In the lattices used in this work, the boundary conditions in the spatial directions are periodic and the one in the temporal direction is anti-periodic. As a direct result of this periodicity, the lattice momenta p_μ are restricted to be discrete as well:

$$p_\mu \in \left\{ \frac{2\pi}{L_\mu} k_\mu \mid k_\mu \in \mathbb{Z} \right\} \quad (1.14)$$

To obtain a lattice equivalent to the fermionic action (Equation (1.5)), we need to define a derivative of these quark fields on the lattice first. There are different ways to do this, resulting in different discretisation errors. Commonly, a symmetrised version of the derivative is chosen,

$$\partial_\mu \psi(n) = \frac{1}{2a} (\psi(n + \hat{\mu}) - \psi(n - \hat{\mu})), \quad (1.15)$$

using which we can write down a simple lattice version of the free fermion action:

$$S_F[\psi, \bar{\psi}] = a^4 \sum_{n \in \Lambda} \bar{\psi}(n) \left(\sum_{\mu=1}^4 \gamma_\mu \partial_\mu \psi(n) + m\psi(n) \right). \quad (1.16)$$

We can check this action for gauge-invariance by considering a $SU(3)$ gauge transformation $\Omega(n)$ of the fields $\psi(n)$, which transforms the fields according to

$$\psi(n) \rightarrow \psi'(n) = \Omega(n)\psi(n) ; \quad \bar{\psi}(n) \rightarrow \bar{\psi}'(n) = \bar{\psi}(n)\Omega^\dagger(n). \quad (1.17)$$

Such a transformation clearly does not keep the free fermion action from Equation (1.16) invariant. The introduction of a gluon field $U_\mu(n)$, which transforms according to

$$U_\mu(n) \rightarrow U'_\mu(n) = \Omega(n)U_\mu(n)\Omega^\dagger(n + \hat{\mu}), \quad (1.18)$$

allows for the formulation of a gauge-invariant lattice action, the so-called *naive fermion action*:

$$S_F[\psi, \bar{\psi}, U] = a^4 \sum_{n \in \Lambda} \bar{\psi}(n) \left(\sum_{\mu=1}^4 \gamma_\mu \frac{1}{2a} (U_\mu(n)\psi(n + \hat{\mu}) - U_{-\mu}(n)\psi(n - \hat{\mu})) + m\psi(n) \right). \quad (1.19)$$

The fields $U_\mu(n)$ can be thought of as gauge transporters between the neighbouring lattice sites n and $n + \hat{\mu}$, directed from the former towards the latter, and are therefore called *link variables*. In Equation (1.19), a link $U_{-\mu}(n)$ has been used, which has the negative directional index $-\mu$ and thus points in the negative μ direction. Alternatively, this link can be expressed as the hermitian conjugate of a 'positively directed' link:

$$U_{-\mu}(n) = U_\mu(n - \hat{\mu})^\dagger. \quad (1.20)$$

A schematic of a lattice Λ including the fields and links can be seen in Figure 1.2. These link variables can be related to the gauge fields in the continuum formulation of QCD. There, we have the path-ordered exponential integral $G(x, y)$ along a curve C_{xy} of the gauge field A :

$$G(x, y) = P \exp \left(i \int_{C_{xy}} A ds \right), \quad (1.21)$$

where P is the path-ordering operator. Under a gauge transformation $\Omega(x)$, they transform similar to the link variables on the lattice:

$$G(x, y) \rightarrow \Omega(x)G(x, y)\Omega(y)^\dagger. \quad (1.22)$$

Based on this observation, we can think of the link variable $U_\mu(n)$ as the lattice version of a contour integral from n to $n + \hat{\mu}$ up to effects in the order of magnitude of the lattice spacing, i.e. $U_\mu(n) = G(n, n + \hat{\mu}) + \mathcal{O}(a)$. This allows

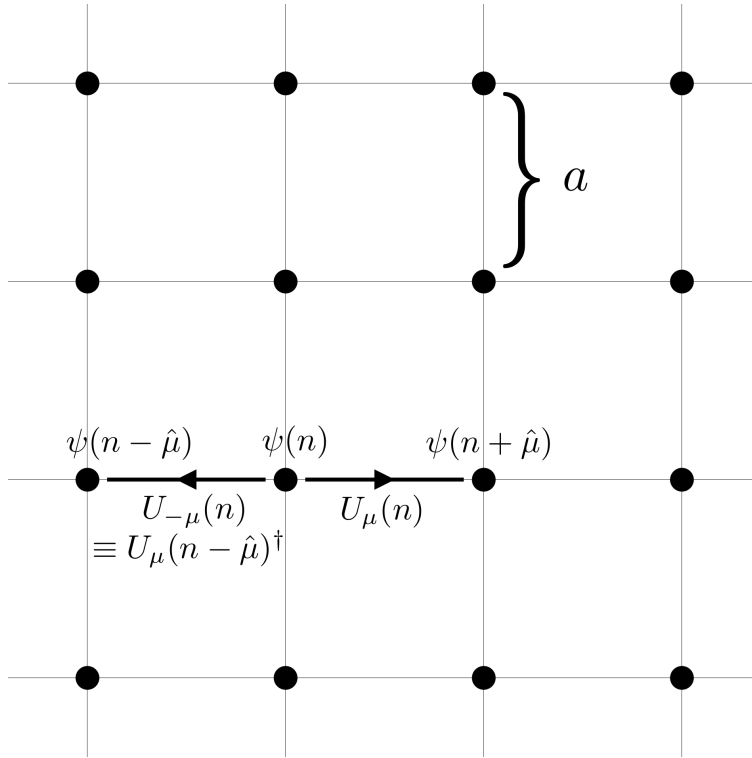


Figure 1.2: A two-dimensional lattice Λ . The gluon fields are represented by link variables, where $U_\mu(n)$ connects the fermion fields $\psi(n)$ and $\psi(n + \hat{\mu})$. The inverse link $U_{-\mu}(n)$ points in the other direction and can be expressed as a hermitian conjugate of the positive link starting at lattice site $n - \hat{\mu}$. The lattice spacing a is the same in each direction for all lattices concerned in this thesis - even though Lattice QCD can be formulated on anisotropic lattices with different lattice spacings a_μ in each direction μ .

the definition of lattice fields $A_\mu(n)$, analogous to the fields A in Equation (1.21),

$$U_\mu(n) = \exp(iaA_\mu(n)) . \quad (1.23)$$

This integral is already calculated up to order $\mathcal{O}(a)$ and corresponds just to the length of the path (the lattice spacing a) times the value of the lattice field $A_\mu(n)$ at lattice site n . Note that the path of this integral is trivially ordered already so that also the path-ordering operator P is not present in this expression.

As the name suggests already, the naive fermion action is still not the final lattice action we would like to use. One problem with it are the so-called *fermion-doublers*. To explain what they are, we have to take a look at the Dirac operator $D(n|m)$, which appears in the lattice fermion action

$$S_F = a^4 \sum_{n,m} \bar{\psi}(n) D(n|m) \psi(m) . \quad (1.24)$$

For the naive fermion action, this Dirac operator reads

$$D(n|m) = \sum_{\mu=1}^4 \gamma_{\mu} \frac{1}{2a} (U_{\mu}(n) \delta_{n+\hat{\mu},m} - U_{-\mu}(n) \delta_{n-\hat{\mu},m}) + m \delta_{n,m}. \quad (1.25)$$

For massless, free lattice fermions ($m = 0$ and $U_{\mu}(n) = 1$) the Fourier transform of this Dirac operator is

$$D(p|q) = \delta(p - q) \frac{i}{a} \sum_{\mu=1}^4 \gamma_{\mu} \sin(p_{\mu} a). \quad (1.26)$$

The quark propagator, which is the inverse of this operator, has an expected pole at $p = (0, 0, 0, 0)$, just like the corresponding momentum space propagator in the continuum. But there are 15 other unphysical poles at $p = (\frac{\pi}{a}, 0, 0, 0)$, $p = (0, \frac{\pi}{a}, 0, 0)$, ..., $p = (\frac{\pi}{a}, \frac{\pi}{a}, \frac{\pi}{a}, \frac{\pi}{a})$. Unfortunately, it turns out to be impossible to remove all of these unwanted fermions easily. In particular, all discretisations of the Dirac operator are subject to the Nielsen-Ninomiya 'no-go' theorem [31–33], which states that no lattice Dirac operator $D_{n,m}$ exists which has all four of these properties:

- $D(n|m)$ is local, which means that it only couples fields $\psi(\bar{n}), \psi(m)$ with $|n - m| = \mathcal{O}(a)$, i.e. that it vanishes sufficiently fast for $|n - m| \rightarrow \infty$
- $D(n|m)$ approaches the correct continuum limit, in momentum space $D(p|q) = i\gamma_{\mu} p_{\mu} + \mathcal{O}(ap^2)$
- $D(n|m)$ respects the chiral symmetry of massless fermions, $\{\gamma_5, D\} = 0$
- $D(p|q)^{-1}$ has only a single pole at $p = 0$

There have been several ideas how to at least reduce the number of species of fermions on the lattice. One of the most straightforward and first ideas how to remove all 15 unwanted species of fermions came from Wilson [34] and is to add the Wilson-term

$$D(p|q)_{\text{Wilson}} = m + \delta(p - q) \frac{i}{a} \sum_{\mu=1}^4 \gamma_{\mu} \sin(p_{\mu} a) + \frac{1}{a} \sum_{\mu=1}^4 (1 - \cos(p_{\mu} a)). \quad (1.27)$$

With this simple addition, the pole at $p = (0, 0, 0, 0)$ is still unaffected while the Wilson term assigns something like a mass to all unphysical fermions with a momentum component of $p_{\mu} = \frac{\pi}{a}$, even at vanishing fermion mass m .

Another way to deal with the unwanted poles are staggered fermions, which reduce the number of fermions to four, while still preserving chiral symmetry [35]. They are quite cheap in terms of computing cost but rely on the *rooting trick*, where the square root of the Dirac operator is taken to reduce the number

of light fermion species from 4 to 2. At finite lattice spacing, this trick leads to a non-local theory which is likely to go away in the continuum limit [36]. There are also *twisted mass* fermions [37–39], which are a variant of the Wilson formulation with an isospin breaking mass term. A very elegant way to deal with the Nielsen-Ninomiya theorem was proposed by Ginsparg and Wilson in 1982, where they suggest to relax the condition that D anticommute with γ_5 , which generalises chiral symmetry to finite lattice spacing a [40]:

$$\{\gamma_5, D\} = aD\gamma_5D. \quad (1.28)$$

As it turns out, this Ginsparg-Wilson relation can be satisfied along with the other three conditions of the Nielsen-Ninomiya theorem - i.e. with this less restrained chiral symmetry condition, a lattice action can be formulated which has only a single species of lattice fermions. One particular realisation of Ginsparg-Wilson fermions are *domain-wall* fermions [41], which are formulated on a $5D$ lattice with a lattice extent N_5 in the fifth direction which works as an exponential suppressor for chirality breaking effects.

In order to expand the Dirac operator for large quark masses m , it is common to redefine it in terms of the *hopping matrix* H ,

$$H_{n,m} = \sum_{\mu=\pm 1}^{\pm 4} (1 - \gamma_\mu) U_\mu \delta_{n+\hat{\mu},m}, \quad (1.29)$$

where $\gamma_{-\mu} \equiv -\gamma_\mu$. This hopping matrix is a collection of all nearest neighbour terms in the operator:

$$D = C(1 - \kappa H), \quad \kappa = \frac{1}{2am + 8}, \quad C = m + \frac{4}{a} \quad (1.30)$$

C is a constant which can be removed by redefining the quark fields $\psi \rightarrow \sqrt{C}\psi$, $\bar{\psi} \rightarrow \sqrt{C}\bar{\psi}$.

The gluonic action can be expressed as a *closed loop* of link variables. The Wilson action uses the simplest such loop, the so-called *plaquette* $P_{\mu\nu}$, which connects four neighbouring lattice sites with each other:

$$P_{\mu\nu}(n) = U_\mu(n)U_\nu(n + \hat{\mu})U_\mu(n + \hat{\nu})^\dagger U_\nu(n)^\dagger. \quad (1.31)$$

The plaquette is schematically shown in Figure 1.3. Using this definition, we can write the gluonic action:

$$S_G[P] = \frac{2}{g_0^2} \sum_{n \in \Lambda} \sum_{\mu < \nu} \text{Tr}[1 - P_{\mu\nu}(n)]. \quad (1.32)$$

Here, g_0 is the (bare) lattice gauge coupling. Often in Lattice QCD, this coupling

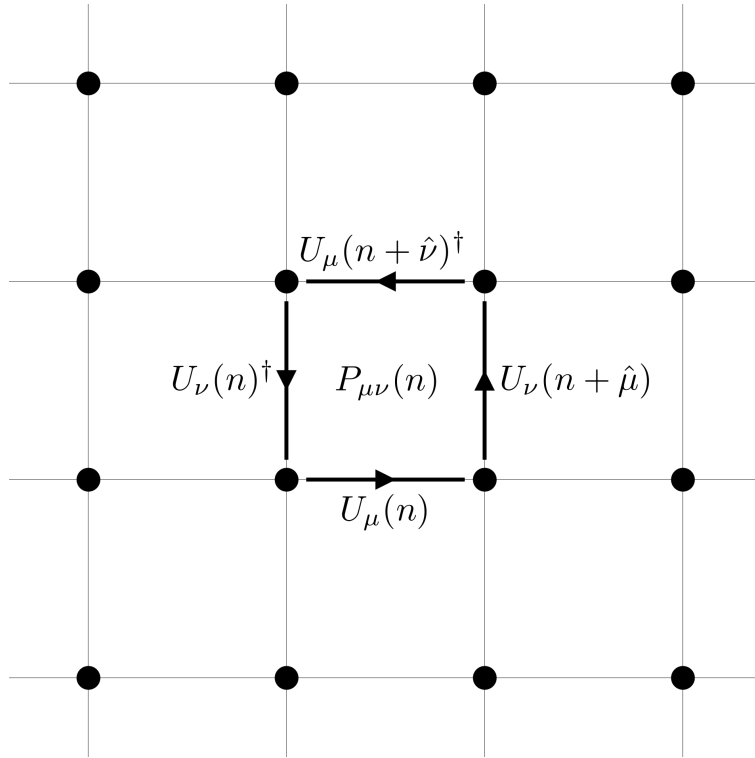


Figure 1.3: A visualisation of the lattice plaquette $P_{\mu\nu}(n)$, which is the smallest closed loop realizable on the lattice.

is expressed via the parameter $\beta = \frac{6}{g_0^2}$. Finally, the full lattice action for Wilson fermions can be written

$$\begin{aligned}
S_W = & a^4 \sum_{n \in \Lambda} [\bar{\psi}(n)\psi(n) - \frac{\kappa}{a} \sum_{\mu} [\bar{\psi}(n)(1 - \gamma_{\mu})U_{\mu}(n)\psi(n + \hat{\mu}) \\
& + \bar{\psi}(n + \hat{\mu})(1 + \gamma_{\mu})U_{\mu}(n)^{\dagger}\psi(n)] \\
& + \frac{\beta}{3} \sum_{n \in \Lambda} \sum_{\mu < \nu} \text{Tr}[1 - P_{\mu\nu}(n)]. \tag{1.33}
\end{aligned}$$

In this action, discretisation errors are $\mathcal{O}(a^2)$ in the gluonic part, but only $\mathcal{O}(a)$ for the fermion part. The idea of *Symanzik improvement* [42,43] is to remove the $\mathcal{O}(a)$ discretisation effects by introducing term of higher mass dimension to the action as counterterms. The Symanzik improvement term for the Wilson action has been written down for the first time by Sheikholeslami and Wohlert [44], such that the whole improved Wilson action reads

$$S_I = S_W + S_{SW} = S_W + c_{SW} a^5 \sum_{n \in \Lambda} \sum_{\mu < \nu} \bar{\psi}(n) \frac{1}{2} \sigma_{\mu\nu} F_{\mu\nu}(n) \psi(n) + \mathcal{O}(a^2), \tag{1.34}$$

with the *Sheikholeslami-Wohlert coefficient* c_{SW} . Newly introduced in here is $F_{\mu\nu}(n)$, which is a lattice version of the field strength tensor. There are a

number of possible choices for this quantity and a usual one is

$$F_{\mu\nu}(n) = \frac{-i}{8a^2}(Q_{\mu\nu}(n) - Q_{\nu\mu}(n)), \quad (1.35)$$

with the *clover term* $Q_{\mu\nu}(n)$, defined as the sum of the four plaquettes P at lattice site n in the $\mu - \nu$ plane:

$$Q_{\mu\nu}(n) = P_{\mu,\nu}(n) + P_{-\nu,\mu}(n) + P_{-\mu,-\nu}(n) + P_{\nu,-\mu}(n). \quad (1.36)$$

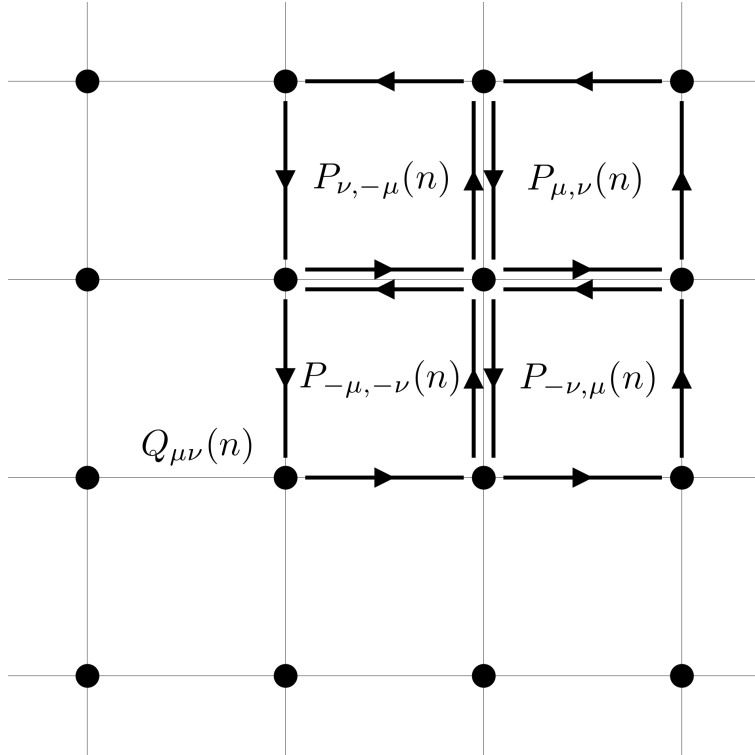


Figure 1.4: A visualisation of the clover term $Q_{\mu\nu}(n)$ on the lattice. It is the sum of the four plaquettes in the $\mu - \nu$ plane at the lattice site n and used in the definition of the clover action.

An illustration of this clover term can be seen in Figure 1.4, which should also explain the name of the term, as it resembles the shape of a clover leaf.

This specific action, i.e. the Wilson Fermion action with clover improvements, is the one used in this thesis. As has been stated already, there are other possible ways to construct a lattice action which converges to the correct continuum QCD action for $a \rightarrow 0$. The same observable, computed on the same lattice but with different actions does not have to be equal though. A comparison of several continuum limits of different lattice calculations is a good tool to check the consistency of these different actions and Lattice QCD in general.

1.1.2 The path integral

Observables can be computed on the lattice via the use of an Euclidean path integral

$$\langle O \rangle = \frac{1}{Z} \int \mathcal{D}[U] \mathcal{D}[\bar{\psi}, \psi] e^{-S_G[U]} e^{-S_F[U, \bar{\psi}, \psi]} O[U, \bar{\psi}, \psi], \quad (1.37)$$

with the partition function

$$Z = \int \mathcal{D}[U] \mathcal{D}[\bar{\psi}, \psi] e^{-S_G[U]} e^{-S_F[U, \bar{\psi}, \psi]}, \quad (1.38)$$

and the $SU(3)$ (gauge field) product measure of the link variables

$$\int \mathcal{D}[U] = \prod_{n \in \Lambda} \prod_{\mu=1}^4 \int dU_{\mu}(n), \quad (1.39)$$

and the Grassmann (fermionic) product measure of the fermion fields

$$\int \mathcal{D}[\bar{\psi}, \psi] = \prod_{n \in \Lambda} \prod_{m \in \Lambda} \int d\psi(n) d\bar{\psi}(m). \quad (1.40)$$

This integral is well-defined, because the lattice and the number of lattice variables is finite. The expectation value of this path integral can thus be split up into two successive expectation values: the gauge field one and the fermionic one:

$$\langle O \rangle = \langle \langle O \rangle_F \rangle_G. \quad (1.41)$$

The Grassmann-valued fermion fields can be integrated out analytically leading to the *fermion determinant*:

$$\langle O \rangle = \frac{1}{Z} \int \mathcal{D}[U] \prod_{f=1}^{N_f} \det D_f[U] (\langle O \rangle_F[U]) e^{-S_G[U]}. \quad (1.42)$$

However, the computation of the determinant of the Dirac operator is very costly, because its dimension is proportional to the number of lattice sites, such that a direct calculation of this determinant is outright impossible for most lattices. Historically, many calculations circumvented this problem by setting $\det D_f = 1$, the so-called *quenched approximation*. Physically, this approximation neglects the effects of the vacuum quark loops - virtual pairs of quarks and antiquarks which are created and annihilated in the fermionic background. These quarks are referred to by the term *sea quarks*. On the other hand, the quarks which directly show up in the propagator are referred to as *valence quarks*.

Almost all modern QCD simulations incorporate the effect of the sea quarks - such a simulation is called a simulation with *dynamical quarks*. In practice, not all quarks are treated dynamically but rather only the lightest ones. This is computationally cheaper and in case of the heavier c, b quarks motivated by decoupling at energy scales lower than their mass. A discussion how to evaluate the decoupling of the charm quark quantitatively is performed in [45, 46]. In the case of $\pi\pi$ scattering, there are no s quarks in any initial or final states. But because the strange quark is lighter than the ρ meson, it is not clear how large the effect of an explicitly included sea-strange quark would be. The pions can still couple to the $K\bar{K}$ channel and it is subject of ongoing research how much this channel actually affects $\pi\pi$ scattering [47]. In this work, we include two dynamical *light* quarks with degenerate masses. The shorthand for this is $N_f = 2$, indicating that there are two degenerate flavours in the simulation. There are also simulations which include a dynamical strange quark, typically with a larger mass. These simulations are more involved and costly and are denoted by $N_f = 2 + 1$. Other simulation types are $N_f = 2 + 1 + 1$ (also including a dynamical charm quark) or $N_f = 1 + 1$ (including u and d quark, but including isospin breaking effects in the sea quarks, i.e. explicitly considering $m_u \neq m_d$). In this shorthand, the quenched simulations can be described as $N_f = 0$.

In any case, the exact computation of an equation like Equation (1.42) is absolutely hopeless even on moderately sized lattices. Typically, a further tool which is used in Lattice QCD calculations is *stochastic Monte-Carlo integration*. Here, the computation is performed on different *gauge configurations*, where a configuration C is defined as a set of gauge links ($SU(3)$ matrices) $U_\mu(n)$ of a lattice Λ :

$$C = \{U_\mu(n) | n \in \Lambda, 0 \leq \mu \leq 3\}. \quad (1.43)$$

In a practical Monte-Carlo analysis, a set of configurations, distributed according to the *statistical weight*

$$W[C] = \frac{1}{Z} \prod_{f=1}^{N_f} \det D_f[C] e^{-S_G[C]} \quad (1.44)$$

is used. This statistical weight is also sometimes called the Boltzmann factor. The idea is now to compute the expectation value of an operator only on a finite number of configurations N_{cfg} and then estimate it by the sample mean of these:

$$\bar{O} = \frac{1}{N_c} \sum_{i=1}^{N_c} O_i, \quad (1.45)$$

where $O_i = O[C_i]$ in a *sample* of gauge configurations $\{C_i | i = 1, \dots, N_{\text{cfg}}\}$ with statistical weights $W[C_i]$. Gauge configurations are drawn according to the distribution using *importance sampling*. From this sample the variance $\sigma^2 = N_{\text{cfg}}^{-1} \sum_i (O_i - \bar{O})^2$ can be calculated to get an estimator with a statistical error, $\langle O \rangle = \bar{O} \pm \sigma$, where the uncertainty is expected to scale like $\frac{1}{\sqrt{N_{\text{cfg}}}}$.

For Grassmann-valued variables (i.e. the fermions in Lattice QCD), standard Monte-Carlo methods cannot be used. Major algorithmic achievements like the Hybrid Monte Carlo (HMC) [48] algorithm make it possible to efficiently use Monte-Carlo methods for Lattice QCD.

1.2 CLS gauge configurations

The gauge configurations used in this work were generated by the Coordinated Lattice Simulations (CLS), an initiative to share the costly generation of configurations amongst several lattice research groups. Configurations are drawn from a sequence $C_1 \rightarrow C_2 \rightarrow \dots$ which is generated using a Markov process. The configurations have an *equilibrium probability distribution* $W[C]$. Such an ordered sequence of configurations is called an *ensemble*. Furthermore, they use a HMC algorithm [48], improved with several other techniques like domain-decomposition (DD-HMC) [49, 50] and mass preconditioning [51], refined to mass-preconditioned HMC (MP-HMC) [52], which are highly efficient tools to speed up the generation process. Parameters of the ensembles used in this work, which all share $\beta = 5.3$ and a lattice spacing of $a = 0.0658(7)(7)\text{fm}$ [53] and have pion masses ranging from 437 MeV to 265 MeV [54] are shown in Table 1.1. One important thing to keep in mind with gauge ensembles is that con-

	T/a	L/a	m_π [MeV]	κ	$m_\pi L$	N_{cfg}	N_{meas}
E5	64	32	437	0.13625	4.7	500	2000
F6	96	48	311	0.13635	5.0	300	900
F7	96	48	265	0.13638	4.2	350	1050

Table 1.1: CLS 2-flavour lattices used in this study. All lattices have $\beta = 5.3$ and a lattice spacing of $a = 0.0658(7)(7)\text{fm}$. N_{meas} are the statistics in the respective ensembles reached by measuring on several source times t_{src} . The value for c_{SW} we use was tuned according to [55].

figurations are correlated (not statistically independent) because configuration C_{n+1} is generated on the basis of configuration C_n . In any analysis, this auto-correlation may lead to the variance σ^2 to be underestimated. This is due to the fact that even the error we asses to any statistically measured quantity is itself subject to a statistical error as well [56]. There are several methods to control this to some degree and we will talk more about the error estimation of our data in Section 1.4.

1.3 Setting the scale

The observables we compute using Lattice QCD are always dimensionless numbers; any dimensionful physical quantity we compute is expressed in units of the lattice spacing a . In the case of an energy or a mass for example, the number we compute on the lattice is aM , where M is the physical mass of the state we measured. In order to obtain a value for the lattice spacing a , which is referred to as *setting the scale*, we have to use a dimensionful physical reference quantity as an input that is accessible experimentally. One way to do this is to choose one hadron H and, for different bare quark mass parameters m_q , compute its mass $aM_H(m_q)$ on the lattice. By extrapolating towards the physical quark mass $m_q \rightarrow m_q^{\text{phys}}$ and comparing the result to the physical hadron mass, one can get an estimate for a via the ratio

$$a \equiv \frac{aM_H(m_q^{\text{phys}})}{M_H^{\text{phys}}}. \quad (1.46)$$

Another reference quantity to set the scale, and the one employed to determine the lattice spacing used in this work, is the Sommer-scale parameter r_0 , which is the distance where the force between static quarks

$$F(r) = \frac{dV(r)}{dr}, \quad (1.47)$$

with the static quark potential $V(r)$ is best understood and whose physical value is about $r_0 \approx 0.5\text{fm}$ [57]. The central equation used to set the scale is

$$r^2 F(r) \Big|_{r=r_0} = 1.65, \quad (1.48)$$

where the value 1.65 is chosen according to models from $\bar{c}c$ and $\bar{b}b$ experiments, precisely to correspond to the Sommer scale. Closed (Wilson) loops, very similar to the plaquette from Equation (1.31), but defined as a rectangle of length $r = na$ in a spatial and $t = n_t a$ in the temporal direction on the lattice decay exponentially with the static potential $V(r) = V(na)$. By defining the force on the lattice via the discretised derivative

$$F(r) = \frac{V(r) - V(r-d)}{d}, \quad (1.49)$$

and assuming $r_0 = 0.5\text{fm}$, $F(r_k)$ can be computed for several values of $r_k = n_k a$. The scale can then be set using Equation (1.48).

For the determination of the lattice spacing used in this work, the Sommer scale was used, but the determination process has been improved upon. One particular downside of the classic approach is that $r_0 = 0.5\text{fm}$ has to be assumed

and a more precise value could be obtained using the kaon-decay constant f_K ¹ as an input to set the scale in our ensembles [58].

1.4 Uncertainty estimate using jackknife

We want to assign a robust error estimate to any observable we compute. If our data would be completely uncorrelated, we could estimate the average and standard deviation of an observable X computed on N different configurations (X_1, X_2, \dots, X_N) simply by computing

$$\hat{X} = \frac{1}{N} \sum_{i=1}^N X_i \quad , \quad \sigma^2 = \frac{1}{N-1} \sum_{i=1}^N (\hat{X} - X_i)^2 ,$$

and quote $\hat{X} \pm \sigma$ as the final estimate for the observable. The problem we face in Lattice QCD though is that our gauge configurations are correlated, because they are computed as a series from one another. Because of those correlations, all observables measured on different configurations of the same ensemble will not be statistically independent; they suffer of so-called *autocorrelations*. To get a handle on these autocorrelations, it would be desirable to compute the exponential autocorrelation time τ_{exp} , which is defined through the correlation Γ of an observable on subsequent configurations

$$\Gamma(t) = \langle X_i X_{i+t} \rangle - \langle X_i \rangle \langle X_{i+t} \rangle \quad , \quad \tau_{exp} = \frac{1}{2} + \sum_{t=1}^N \frac{\Gamma(t)}{\Gamma(0)} , \quad (1.50)$$

and which would indicate how strongly subsequent measurements are correlated. The true variance σ_{true}^2 could then be computed from this autocorrelation time and the naive variance:

$$\sigma_{true}^2 = 2\tau_{exp}\sigma^2 . \quad (1.51)$$

In practice however, it turns out to be very difficult to reach the necessary statistics for a precise determination of autocorrelation times for typical hadronic quantities and instead some simpler and cheaper procedures to assign an error estimate to the observable are used. One of these approaches, and the one used throughout this thesis, is jackknife [59, 60]. It is a so-called data-blocking method, which relies on the assumption that when the data is divided into sub-blocks first, that their mean values are statistically independent for a large enough sample size. The error estimates can then be computed by the variance of the mean values of the data in these sub-blocks. In jackknife, N new sets of

¹Because we are working on $N_f = 2$ ensembles, a quenched strange quark had to be included in this determination.

data are defined, which are the average of all configurations with only a single one left out, i.e.

$$\tilde{X}_i \equiv \frac{1}{N-1} \sum_{\substack{j=0 \\ j \neq i}}^N X_j, \quad (1.52)$$

and the variance can then be computed via

$$\sigma^2 = \frac{N-1}{N} \sum_{i=1}^N (\hat{X} - \tilde{X}_i)^2. \quad (1.53)$$

Chapter 2

Hadron spectroscopy

Before we can actually study a resonance, we have to gain insight into the energy spectrum of the resonance decay channel we are interested in. In this chapter we will explain our strategies to obtain information on the properties, particularly the masses, of hadrons (in our case only mesons) on our lattices. This is referred to as *hadron spectroscopy*. We will also talk about the specific challenges which are to overcome in order to study not only QCD-stable states, but also resonances.

For the moment, we will leave the discussion of resonances at the comment that there is a formalism (explained in Chapter 3.3) which allows us to obtain information on the resonance if we know the energy spectrum of QCD-stable states in the corresponding decay channel in the finite lattice box sufficiently well. Our intermediate objective is therefore to extract this energy spectrum from the lattice. The main observables which are needed for this task are two-point correlation functions

$$C(t, t_0) = \langle O(t)O(t_0)^\dagger \rangle, \quad (2.1)$$

where $O(t_0)^\dagger$ creates a state at time t_0 and $O(t)$ annihilates this state at time t . These *interpolating operators* of a meson with quark flavours f_1 and f_2 can be defined as

$$O_M(n) = \bar{\psi}^{(f_1)}(n)\Gamma\psi^{(f_2)}(n), \quad (2.2)$$

where Γ encodes the spin structure. The fermionic expectation value of such a correlator can be written as a trace of a product of propagators (inverse of the Dirac operator) and the matrices Γ :

$$\langle O_M(n)O_M(m)^\dagger \rangle_F = -\text{tr}[\Gamma D_{(f_1)}^{-1}(n|m)\Gamma D_{(f_2)}^{-1}(m|n)]. \quad (2.3)$$

For two single meson operators (consisting of two quarks each) we can directly calculate this expression on the lattice. Because the expectation value has to be

invariant under all temporal and spatial translations, we only need to consider the operator $O_M(m)^\dagger$ on a single lattice site (i.e. one single point in time and space) to calculate a *point-to-all* propagator.

The $\rho \rightarrow \pi\pi$ channel we are interested in in this work cannot be fully described when just using single-meson operators though. The reason for this is that if we want to extract the resonance state $\rho(t)$, we must first extract all states of the system lying below that state. For ensembles with light enough pion masses, like the ones employed in this work, we also need to include the two-pion operators $(\pi\pi)(t)$. We could potentially calculate an expectation value like the one in Equation (2.3) as well for multi-particle operators, but in this case translation symmetry would only remove one of the spatial sums on the source timeslice. This poses another challenge to overcome: In addition to the quark propagation from the *source* (initial time) to the *sink* (final time), there is also quark propagation from sink to sink. A schematic diagram of a correlation function involving such a sink-to-sink propagation is shown in Figure 2.1. For a naive computation of such a *sink-to-sink* quark line, the Dirac matrix D would have to be inverted for each pair of quark positions on the sink timeslice - a prohibitively expensive task. There are several strategies which

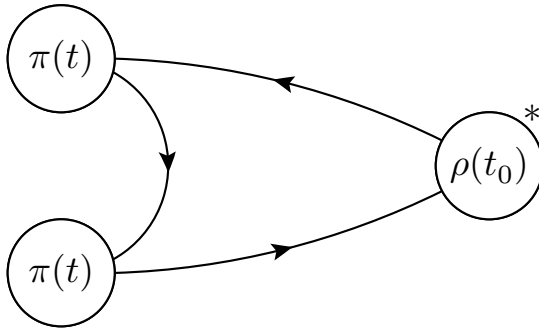


Figure 2.1: Diagrammatic illustration of a $\langle(\pi\pi)(t)\rho^\dagger(0)\rangle$ correlation function. The two-meson operator on the sink timeslice t is difficult to treat numerically because of the sink-to-sink quark propagation.

deal with the computation all-to-all propagators in acceptable time. We are using (stochastic) Distillation in this work, which performs the inversions only in a smaller subspace and which estimates the quark propagation stochastically. We will introduce this method in detail in Sections 2.2 and 2.3.

2.1 The variational method

For the moment, we will assume that we know already how to create two-point functions, like the one in Equation (2.1), for all operator combinations in our decay channel. The next step after the computation of these correlation functions is to extract the energy spectrum from them. In particular we are

not only interested in the energy of the ground state of the system, but also in the low-lying excited states. This proves to be not so trivial, because we cannot simply define some lattice operators which couple exclusively to a single state. The lattice operators we define are rather operators which we hope to have a large overlap with some state, but in practice they have overlap with a superposition of all other states in the spectrum, sharing the same quantum numbers. A method to extract the lowest states of a spectrum is to create a matrix of correlation functions of operators with matching quantum numbers

$$C_{ij}(t) = \langle O_i(t)O_j(0)^\dagger \rangle = \sum_{n=1}^{\infty} e^{-E_n t} \langle 0|\hat{O}_i|n\rangle \langle n|\hat{O}_j^\dagger|0\rangle \quad (2.4)$$

of the correlators in a given frame and then to solve a generalised eigenvalue problem (GEVP) [61–63]

$$C(t)\mathbf{v}(t, t_0) = \lambda(t, t_0)C(t_0)\mathbf{v}(t, t_0) \quad (2.5)$$

for this matrix. This method is known as the *variational method*. It can be shown that the n^{th} eigenvalue λ_n asymptotically decays exponentially with the energy of the n^{th} state, i.e.

$$\lambda_n(t, t_0) \rightarrow A_n e^{-E_n(t-t_0)} \quad (2.6)$$

for large times t . It is worth noting that this insight implies that, in order to study the $(n+1)^{\text{th}}$ energy level of a spectrum, one has to extract the n lower lying states along with it, i.e. solve a GEVP for a matrix with at least $(n+1)$ interpolators coupling to the same tower of energy states. This becomes particularly crucial for lattices with small pion masses, where the spectrum becomes denser with more many multi-hadron states present. We will talk about strategies to define a good operator basis in Sections 2.2 and 2.3.

There are different ways of choosing the parameter t_0 in Equation (2.6). Because $C(t_0)$ becomes noisier for large t_0 and might not even be positive definite any more at large time separations, the GEVP might become an ill-posed problem in this regime. One simple method to avoid this is to keep t_0 fixed at some low timeslice like $t_0 = 3$. The advantage of this approach is that $C(t_0)$ is still well-defined and we can follow $\lambda(t, t_0)$. One can define the effective mass

$$E_{n,\text{eff}}\left(t + \frac{1}{2}\right) = \ln \frac{\lambda_n(t)}{\lambda_n(t+1)}. \quad (2.7)$$

The effective mass approaches its asymptotic value E_n with corrections of the order of the gap between the energy level to be extracted and the one closest

to it [63]

$$E_{n,\text{eff}}(t, t_0) = E_n + \epsilon_n(t, t_0), \quad (2.8)$$

$$\epsilon_n(t, t_0) = \mathcal{O}(e^{-\Delta E_n t}), \quad \Delta E_n = \min_{n \neq m} |E_m - E_n|. \quad (2.9)$$

Because of this, this method is well motivated as long as there are no energy levels close to the ones which are to be extracted, in which case ΔE_n would be small and thus $\epsilon_n(t, t_0)$ could be large. A way to circumvent this problem is to demand that $t_0 > t/2$ for all times t in the GEVP. In this region, the energy gaps to the next contributing level is much larger [64]:

$$\epsilon_n(t, t_0) = \mathcal{O}(e^{-\Delta E_{N+1, n} t}), \quad \Delta E_{m, n} = E_m - E_n, \quad t_0 > t/2, \quad (2.10)$$

where N is the number of interpolating fields in the correlation matrix $C(t)$. One way to achieve this is the so-called *window method* [64], where $t_w \equiv t - t_0$ is kept constant. The window width is also usually kept at some small value like $t_w = 3$, which automatically ensures that $t_0 > t/2$ at physically relevant time separations. The eigenvalues extracted from the GEVP in the window method are approaching a constant

$$\lambda^{(k)}(t, t_w = t - t_0) \rightarrow e^{-E_k t_w}, \quad (2.11)$$

which means that we cannot simply define the effective mass as a ratio of eigenvalues extracted on subsequent timeslices like in Equation (2.7). One way around this is to define the effective mass from the logarithm of a single eigenvalue,

$$E_{n,\text{eff}}(t, t_0) = -\frac{1}{t_w} \ln \lambda_n(t, t_0). \quad (2.12)$$

Another possibility is to solve the GEVP a second time with a different window with like $t'_w = t_w - 1$,

$$C(t)\mathbf{v}(t, t - t_w) = \lambda(t, t - t_w)C(t - t_w)\mathbf{v}(t, t - t_w) \quad (2.13)$$

$$C(t)\mathbf{v}'(t, t - t_w + 1) = \lambda'(t, t - t_w + 1)C(t - t_w + 1)\mathbf{v}'(t, t - t_w + 1), \quad (2.14)$$

and then to define the effective mass as the ratio of the eigenvalues extracted from the two GEVP

$$E_{n,\text{eff}}\left(t - \frac{1}{2}\right) = \ln \frac{\lambda'_n(t, t - t_w + 1)}{\lambda_n(t, t - t_w)}. \quad (2.15)$$

which is expected to approach E_n at large times as well. Of course, $C(t - t_w)$ will be quite noisy and potentially non-positive definite for large t , so the signal

usually is lost in noise at smaller time separations than in the fixed- t_0 method.

2.2 Distillation

We will move the discussion now a bit; from the conceptual idea of how to extract the spectrum to the technicalities of the computation of the correlation functions which we need for this spectrum extraction. The techniques we will present in here have their main strength in the computation of correlation functions involving multi-hadron operators, but several other advantages like the re-usability of certain building blocks come with it as well.

We want the operators we are defining to be suitable to extract the energy spectrum – but even if we only want to extract the ground state of a system, a simple meson operator like the one in Equation (2.3) would not be sufficient. To get a good overlap with the ground state, some *smearing* is usually applied to the operators. This smearing of the fields should be applied in a way such that most symmetries are preserved, while short-range modes, which mostly introduce noise to the low-energy spectrum, are removed. One of those smearing algorithms for the link variables $U_\mu(n)$ is APE smearing [65], where a product of links along all *perpendicular staples* $C_{\mu,\nu}(n)$ to $U_\mu(n)$ is formed, and then projected back into an $SU(3)$ matrix. Each perpendicular staple is one of the shortest detours from lattice site n to $n + \hat{\mu}$:

$$C_{\mu,\nu}(n) = U_\nu(n)U_\mu(n + \hat{\nu})U_\nu^\dagger(n + \hat{\mu}), \quad (2.16)$$

Distillation [16] constructs a quark field smearing which renders the calculation of the sink-to-sink lines possible. The idea is to start from the lattice Laplacian,

$$-\nabla_{nm}^2(t) = 6\delta_{nm} - \sum_{j=1}^3 (\tilde{U}_j(n, t)\delta_{n+\hat{j}, m} + \tilde{U}_j^\dagger(n - \hat{j}, t)\delta_{n-\hat{j}, m}), \quad (2.17)$$

where the gauge fields \tilde{U} are already smeared to suppress UV fluctuations of the gauge field. In our work we used stout smearing [66], which has the advantage that it exactly preserves the $SU(3)$ symmetry (i.e. it does not need a projection back into $SU(3)$ like e.g. HYP [67] smearing) of those fields and that it is differentiable. Stout smearing uses a weighted sum of all perpendicular staples,

$$C_\mu(n) = \sum_{\nu \neq \mu} \rho_{\mu\nu} \left(C_{\mu,\nu}(n) + C_{\mu,-\nu}(n) \right), \quad (2.18)$$

where the staple weights $\rho_{\mu,\nu}$ are real parameters which can be tuned. A schematic of $C_\mu(n)$ can be seen in Figure 2.2. Then, the gauge links are it-

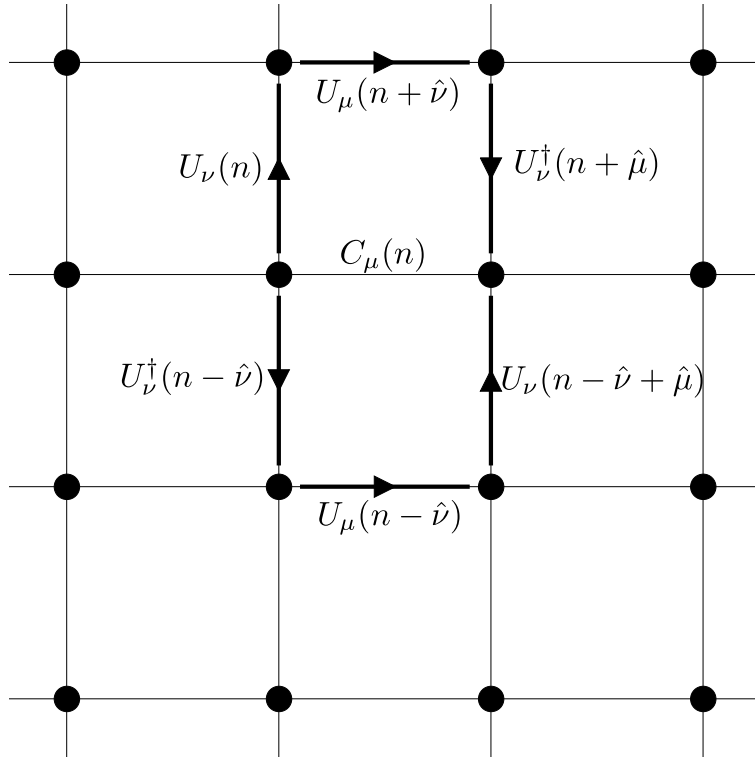


Figure 2.2: Sum of perpendicular staples $C_\mu(n)$ on a $2D$ lattice. On a $4D$ lattice, like the ones used in our calculation, there would be two more directions with two perpendicular staples each. Each of these staple pairs is also weighted by a staple weight $\rho_{\mu\nu}$.

eratively smeared by applying

$$U_\mu^{(k+1)}(n) = \exp\left(iQ_\mu^{(k)}(n)\right)U_\mu^{(k)}(x), \quad (2.19)$$

where the initial gauge link is set to $U_\mu^{(0)}(x) \equiv U_\mu(x)$ and

$$Q_\mu^{(k)}(n) = \frac{i}{2}\left(\Omega_\mu^{(k)\dagger}(n) - \Omega_\mu^{(k)}(n)\right) - \frac{i}{2N}\text{Tr}\left(\Omega_\mu^{(k)\dagger}(n) - \Omega_\mu^{(k)}(n)\right), \quad (2.20)$$

$$\Omega_\mu^{(k)}(n) = C_\mu(n)U_\mu^{(k)\dagger}(n). \quad (2.21)$$

After n_ρ iteration steps

$$U_\mu(n) \equiv U_\mu^{(0)}(n) \rightarrow U_\mu^{(1)}(n) \rightarrow U_\mu^{(2)}(n) \rightarrow \dots \rightarrow U_\mu^{(n_\rho)}(n) \equiv \tilde{U}_\mu(n). \quad (2.22)$$

the smeared *stout link* $\tilde{U}_\mu(n)$ is defined. In our work we use the stout smearing parameters of $n_\rho = 3$ and $\rho_{jk} = 0.2$ and $\rho_{4\mu} = \rho_{\mu 4} = 0$.

The next step is to obtain the low-lying eigenmodes of the spectrum of the Laplacian, i.e. to solve the eigenvalue equation

$$-\nabla^2 v^{(k)} = \lambda^{(k)} v^{(k)}, \quad (2.23)$$

where a cut-off parameter needs to be chosen, typically by setting the number of eigenvalues N_{ev} which are taken into account. The reason to choose the Laplacian is again that it preserves the symmetries we need in our calculation – most importantly gauge symmetry. After sorting these eigenvalues such that $\lambda^{(1)} < \lambda^{(2)} < \dots < \lambda^{(N_{ev})}$, the *distillation operator* is defined by

$$\mathcal{S}(x, y; t) = \sum_{k=1}^{N_{ev}} v_x^{(k)}(t) v_y^{(k)\dagger}(t). \quad (2.24)$$

Alternatively, this equation can be rewritten as a single matrix equation

$$\mathcal{S}(t) = V(t)V^\dagger(t), \quad (2.25)$$

where the k^{th} column of $V(t)$ is the k^{th} eigenvector of the Laplacian. Because the cut-off can mathematically be represented by the Heaviside function,

$$\mathcal{S} = \Theta(\sigma^2 + \nabla^2), \quad (2.26)$$

where sigma is the chosen cut-off parameter ($\lambda^{(N_{ev})} < \sigma < \lambda^{(N_{ev}+1)}$) this smearing is also called *Laplacian Heaviside* (LapH) smearing. The dimension of $V(t)$ is thus $3 \cdot N_L^3 \times N_{ev}$ with $3 = N_c$ the number of colors in our theory and N_L the number of lattice points in each spatial direction. In particular, this dimension can be much smaller than the dimension of the full vector space V_M the LapH smearing is acting on, whose dimension is $3 \cdot N_L^3 \times 3 \cdot N_L^3$. The matrix $V(t)$ can therefore also be viewed as the projection operator into the subspace $V_{N_{ev}}$, spanned by the eigenmodes of the Laplacian. When choosing $N_{ev} = 3 \cdot N_L^3$, the eigenmodes span the full space and the distillation operator is simply the identity. Meson correlation functions (Equation (2.3)) built from smeared quark fields take the form:

$$\langle O_M(x, t) \bar{O}_M(y, t') \rangle_F = \text{tr}[\Phi(t') \tau(t', t) \Phi(t) \tau(t, t')], \quad (2.27)$$

with

$$\Phi_{\alpha\beta}(t) = V^\dagger(t) [\Gamma(t)]_{\alpha\beta} V(t), \quad (2.28)$$

and the so-called *perambulators*

$$\tau_{\alpha\beta}(t', t) = V^\dagger(t') D_{\alpha\beta}^{-1}(t', t) V(t). \quad (2.29)$$

Both Φ and τ are square matrices of dimension $4 \cdot N_{ev} \times 4 \cdot N_{ev}$, with $4 = N_S$ being the number of Dirac spinor components. In order to compute τ , we therefore need only $4 \cdot N_{ev}$ operations of D^{-1} on a vector, which is a much more feasible

task than the direct computation of matrix elements of D^{-1} for each pair of quark positions. Also, all information about source and sink interpolators are in Φ , but not in τ . This means that τ can be calculated and potentially saved to disk in a first step, and the correlation functions are then built in a cheaper step (re-)using the perambulators and contracting them with the quark propagation information stored in τ .

2.3 Stochastic LapH

Distillation is definitely a powerful tool, but the computation of the quark propagators still needs a lot of inversions, in particular on larger lattices. The reason for this is that N_{ev} cannot be chosen arbitrarily low, but rather scales linearly with the physical volume if the smearing radius is to be kept constant. Because the cost per inversion scales with V as well, the total computational cost scales with the square of the volume, which makes pure distillation too expensive on large lattices. One solution to this problem is to obtain a stochastic estimate of the quark lines such that the statistical noise introduced by this stochastic distillation matches the gauge-field noise of the Monte-Carlo evaluation [17]. To treat distillation with LapH smearing stochastically, N_R random noise vectors are introduced. Firstly, we will describe the stochastic estimation of Matrix inverses with random noise vectors η with the expectation values $\langle \eta_i \rangle = 0$ and $\langle \eta_i \eta_j^* \rangle = \delta_{ij}$, before specializing to the case of stochastic LapH. Solving the linear system of equations

$$DX^r = \eta^r \quad (2.30)$$

for X^r allows for the Monte-Carlo estimate of the inverse Dirac matrix

$$D_{ij}^{-1} = \frac{1}{N_R} \sum_{r=1}^{N_R} X_i^r \eta_j^{r*} . \quad (2.31)$$

To further reduce the variance of the stochastic estimator, the noise vectors are *diluted* [68, 69], which is done by applying orthogonal projection operators $P^{[b]}$ to the noise vectors

$$\eta^{r[b]} \equiv P^{[b]} \eta^r , \quad X^{r[b]} = D^{-1} \eta^{r[b]} , \quad (2.32)$$

leading to the Monte-Carlo estimator

$$D_{ij}^{-1} = \frac{1}{N_R} \sum_{r=1}^{N_R} \sum_b X_i^{r[b]} \eta_j^{r[b]*} . \quad (2.33)$$

Its expectation value

$$\langle \sum_b \eta_i^{[b]} \eta_j^{[b]*} \rangle \quad (2.34)$$

is equal to the expectation value of the undiluted estimator

$$\langle \eta_i \eta_j^* \rangle = \langle \sum_{bb'} \eta_i^{[b]} \eta_j^{[b']*} \rangle, \quad (2.35)$$

but many of the terms contributing to the variance are now not only statistically but rather exactly zero (due to the orthogonality of $P^{[b]}$). In this way, Dilution directly reduces the variance of the stochastic estimator of D^{-1} . In the stochastic LapH method, noise is introduced in the LapH subspace. Those LapH-noise vectors ρ are diluted in spin, time and Laplacian eigenmode number (which includes colour and spatial lattice sites). We still have $\langle \rho_i \rangle = 0$ and $\langle \rho_i \rho_j^* \rangle = \delta_{ij}$ and our dilution projectors $P^{[b]}$ are now matrices in the LapH subspace. A quark line can then be computed via

$$\begin{aligned} \mathcal{Q} &= \mathcal{S} D^{-1} \mathcal{S} = \mathcal{S} D^{-1} V_S V_S^\dagger \\ &= \sum_b \mathcal{S} D^{-1} V_S P^{(b)} P^{(b)\dagger} V_S^\dagger \\ &= \sum_b \mathcal{S} D^{-1} V_S P^{(b)} E(\rho \rho^\dagger) P^{(b)\dagger} V_S^\dagger \\ &= \sum_b E((\mathcal{S} D^{-1} V_S P^{(b)} \rho)(V_S P^{(b)} \rho)^\dagger) \\ &\equiv \sum_b E(\varphi^{[b]}(\rho)(\varrho^{[b]}(\rho))^\dagger). \end{aligned} \quad (2.36)$$

where we have defined the LapH sink vectors φ and the LapH source vectors ϱ :

$$\varphi^{[b]}(\rho) = \mathcal{S} D^{-1} V_S P^{(b)} \rho \quad (2.37)$$

$$\varrho^{[b]}(\rho) = V_S P^{(b)} \rho. \quad (2.38)$$

Because of the γ_5 hermiticity of D ($D^\dagger = \gamma_5 D \gamma_5 \Rightarrow (D^{-1})^\dagger = \gamma_5 D^{-1} \gamma_5$) we can also calculate this quark line in a different way:

$$\begin{aligned} \mathcal{Q} &= \sum_b V_S P^{(b)} E(\rho \rho^\dagger) P^{(b)\dagger} V_S^\dagger D^{-1} \mathcal{S} \\ &= \sum_b E((V_S P^{(b)} \rho)(\mathcal{S}^\dagger (D^{-1})^\dagger V_S P^{(b)} \rho)^\dagger) \\ &= \sum_b E((V_S P^{(b)} \rho)(\mathcal{S} \gamma_5 D^{-1} \gamma_5 V_S P^{(b)} \rho)^\dagger) \\ &= \sum_b E((V_S P^{(b)} \rho) \gamma_5^\dagger (\gamma_5 \mathcal{S} D^{-1} V_S P^{(b)} \rho)^\dagger) \end{aligned}$$

$$\begin{aligned}
&= \sum_b E((\gamma_5 V_S P^{(b)} \rho)(\gamma_5 \mathcal{S} D^{-1} V_S P^{(b)} \rho)^\dagger) \\
&= \sum_b E(\bar{\varrho}^{[b]}(\rho)(\bar{\varphi}^{[b]}(\rho))^\dagger).
\end{aligned} \tag{2.39}$$

where the alternative LapH source and sink vectors can be related to the ones from before via:

$$\bar{\varphi}^{[b]}(\rho) = \gamma_5 \varphi^{[b]}(\rho) \tag{2.40}$$

$$\bar{\varrho}^{[b]}(\rho) = \gamma_5 \varrho^{[b]}(\rho). \tag{2.41}$$

With all indices explicitly spelled out the Monte-Carlo estimator for a quark line is

$$\mathcal{Q}_{b\beta; a\alpha}(\mathbf{y}, t; \mathbf{x}, t_0) = \frac{1}{N_R} \sum_{r=1}^{N_R} \sum_b \varphi_{b\beta}^{r[b]}(\mathbf{y}, t) \varrho_{a\alpha}^{r[b]*}(\mathbf{x}, t_0), \tag{2.42}$$

or with the alternative LapH vectors:

$$\mathcal{Q}_{a\alpha; b\beta}(\mathbf{x}, t_0; \mathbf{y}, t) = \frac{1}{N_R} \sum_{r=1}^{N_R} \sum_b \bar{\varrho}_{a\alpha}^{r[b]}(\mathbf{x}, t_0) \bar{\varphi}_{b\beta}^{r[b]*}(\mathbf{y}, t). \tag{2.43}$$

In our calculation, we always use full spin dilution and an interlaced time dilution of 8, in the notation for dilution introduced in [17]. On ensemble E5 (see Table 2.1), all lines connected to the source are computed using full distillation and only the sink-to-sink lines use stochastic distillation. On F6 and F7, stochastic distillation is used on all lines. The full dilution scheme as well as the number of eigenmodes computed on each lattice is given in Table 2.1.

	TI (sts)	TI	LI (sts)	LI	SI	N_T	N_{ev}
E5	8	64	12	56	4	64	56
F6	8	96	12	12	4	96	192
F7	8	96	12	12	4	96	192

Table 2.1: Dilution schemes on the lattices used in this work. All lattices have full spin dilution and an interlaced time (TI) dilution of 8 for the the sink-to-sink (sts) lines and full time dilution (TI = N_T) for lines connected to the source timeslice. This does not mean that we calculated propagators for all N_T source times; we have rather computed point-to-all propagators on several source times on each ensemble, as is shown in Table 1.1. Stochastic interlaced Laplacian dilution (LI) is used for all lines on F6 and F7. On E5, only the sink-to-sink lines use stochastic Laplacian distillation and for the other lines, full distillation (LI = N_{ev}) is used.

Meson-to-meson correlation functions can now be expressed as a product of

two of these quark lines. With the definition of a *meson function*

$$\mathcal{M}^{[b_1, b_2], (\rho_1, \rho_2)}(\mathbf{v}_1, \mathbf{w}_2; \mathbf{p}, t) = \Gamma_{\alpha\beta} \sum_{\mathbf{x}} e^{-i\mathbf{p}\cdot\mathbf{x}} \mathbf{v}_{a\alpha, \mathbf{x}t}^{[b_1]} (\rho_1)^* \mathbf{w}_{a\beta, \mathbf{x}t}^{[b_2]} (\rho_2), \quad (2.44)$$

where \mathbf{v}, \mathbf{w} are LapH source or sink vectors $\varrho/\bar{\varrho}$ or $\varphi/\bar{\varphi}$, a meson-to-meson correlation function can be written

$$C_{\bar{u}}(t_F, t_0) = \langle -\mathcal{M}_I^{[b_1, b_2], (\rho_1, \rho_2)}(\bar{\varphi}_i, \varphi_j; t_F) \mathcal{M}_I^{[b_1, b_2], (\rho_1, \rho_2)}(\bar{\varrho}_i, \varrho_j; t_0)^* \rangle_{U, \rho}. \quad (2.45)$$

This expression uses the Einstein summation convention for the dilution indices b_1, b_2 . The noise average $\langle \dots \rangle_\rho$ has to be taken so that different quark lines use different noise sources. In here, we have chosen to evaluate some quark lines using Equation (2.36) and other using the alternative evaluation from Equation (2.39). We have done this in a way such that the LapH source vectors ϱ , which do not have the inverse of the Dirac matrix D^{-1} in them, are all on the source timeslice t_0 . This way, we only have to compute D^{-1} using sources with support on only a single timeslice, and not on multiple ones like if they were on the sink timeslice. In other words: For the antiquark in a meson, where the LapH-source vector ϱ would usually lie on the sink timeslice, we choose to swap the roles of the LapH-source and LapH-sink vectors $(\varrho, \varphi) \rightarrow (\bar{\varphi}, \bar{\varrho})$. A graphical depiction of Equation (2.45) can be seen in Figure 2.3. One of the

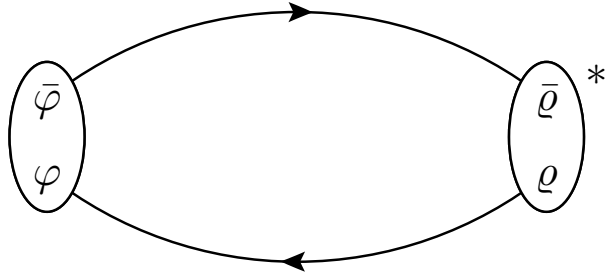


Figure 2.3: Diagrammatic illustration of a $\langle \rho(t)\rho^\dagger(0) \rangle$ correlator in the LapH formulation.

most important strengths of Distillation can be seen directly in this equation: The correlator is a product of two functions, one of which governs the sink time t and the other one the source time t_0 . With all summations at these two times (color, spin, spatial) being factorised, the approach can be modular: Meson functions have to be computed only once, can then be stored on disk and can be used to compute various correlators at a comparably cheap cost, by just contracting the indices in the desired manner. We also show the diagrams contributing to the $\langle \rho(t)(\pi\pi)^\dagger(0) \rangle$ and $\langle (\pi\pi)(t)(\pi\pi)^\dagger(0) \rangle$ in Figures 2.4 and 2.5.

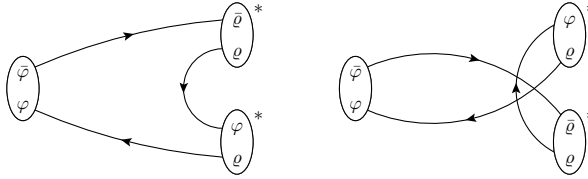


Figure 2.4: Diagrammatic illustration of the two diagrams contributing to the $\langle \rho(t)(\pi\pi)^\dagger(0) \rangle$ correlator in the LapH formulation.

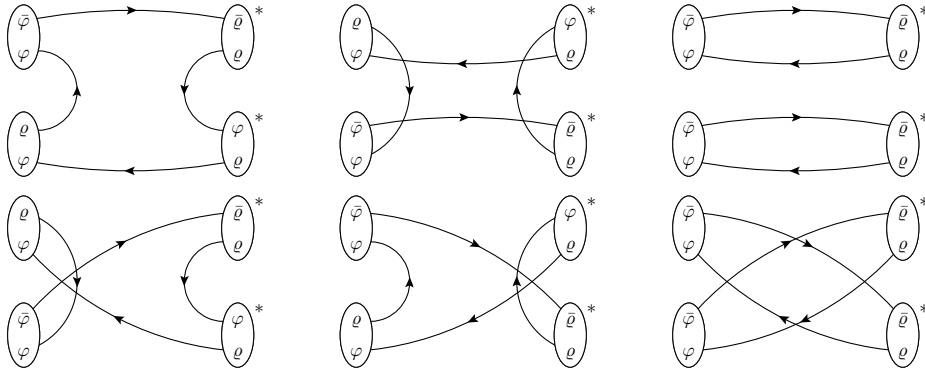


Figure 2.5: Diagrammatic illustration of the six diagrams contributing to the $\langle (\pi\pi)(t)(\pi\pi)^\dagger(0) \rangle$ correlator in the LapH formulation.

Part of this thesis is also the computation of the timelike pion form factor in Section 5.1. We won't go into the full details of this calculation but will note here that one more object directly coming from the distillation / LapH approach is needed in there, to wit the vector current matrix elements [3]

$$A_\Psi = \langle 0 | j_\mu^{em} | \Psi_\sigma^a \rangle, \quad (2.46)$$

with the (in our case 2-flavor) electromagnetic current

$$j_\mu^{em} = \frac{2}{3} \bar{u} \gamma_\mu u - \frac{1}{3} \bar{d} \gamma_\mu d. \quad (2.47)$$

Because we need to properly renormalise these current matrix elements and the LapH smearing interferes with the renormalisation properties, we need unsmearing quark fields for the computation of those. In addition to the LapH sink- and source vectors defined in Equation (2.38), we thus need an additional unsmearing sink vector:

$$\theta^{[b]}(\rho) = D^{-1} V_S P^{(b)} \rho. \quad (2.48)$$

The rest of the machinery remains unchanged, so that we can also compute objects similar to the meson functions, now more appropriately called *current sink*

functions. These objects are computed at the same steps where the stochastic perambulators are constructed and are saved to disk immediately.

Chapter 3

Phenomenology of the ρ resonance

We will move from the general discussion of hadron spectroscopy and the tools needed to perform it towards a more explicit explanation of our specific set-up to study the $\rho \rightarrow \pi\pi$, isospin = 1 decay channel. Resonances are related to the analytical structure of the scattering amplitude $\mathcal{M}_1(E_{cm})$. In experiments, resonances can be identified by a peak in some energy region of the cross section, which we cannot directly access on the lattice. The reason for this is that the lattice, being formulated in Euclidean space, can only give information on stable states. In Chapter 3.3 we will introduce the formalism to identify them by their impact on intermediate states. A plot of the cross section of $e^+e^- \rightarrow \pi^+\pi^-$ as observed in the BESIII experiment [70] is shown in Figure 3.1. The energy

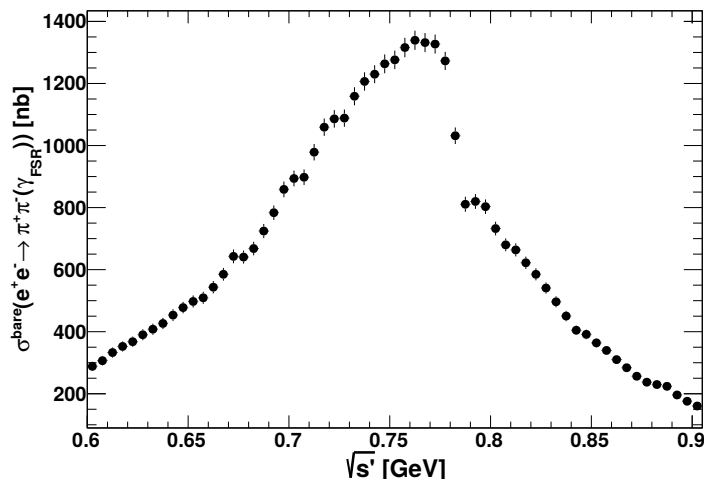


Figure 3.1: Cross section of $e^+e^- \rightarrow \pi^+\pi^-$ scattering in the BESIII experiment as a function of the centre-of-mass energy $E_{cm} = \sqrt{s}$, taken from [70]. Also visible is the $\rho - \omega$ interference.

range the plot shows is the one of the ρ resonance, which we study from a theory

point of view in this work and the peak in the cross section is clearly visible. The peak does not have a Gaussian shape, but rather has a very steep slope on the right-hand side of the peak - this is due to the $\rho - \omega$ interference. We do not expect to see this interference in our work, because we constrain our operators to be purely in P -wave, which is where the $\rho \rightarrow \pi\pi$ scattering occurs, but the ω is absent.

In this chapter we will talk about the explicit interpolators we use in this work and also show the resulting correlation functions needed for the study of $\pi\pi$ scattering. We will talk about the different moving frames we are extracting energy levels from in Section 3.2 and in particular talk about the symmetries on the lattice which give rise to several irreducible representations in each of those frames. In Section 3.3 we will introduce the Lüscher formalism [1, 2], which exploits the finite-volume effects incurred in Lattice QCD as a tool to extract infinite-volume scattering information. This formalism was already briefly mentioned earlier as our motivation to extract the finite-box energy spectrum from the lattice.

3.1 Explicit construction of correlation functions

For the construction of correlators we need to define suitable ρ and $\pi\pi$ interpolators first. This means that we have to define operators which share their respective quantum numbers. A suitable interpolator for the ρ meson on the lattice at time t with momentum \mathbf{P} is [71]

$$\rho(\mathbf{P}, t) = \frac{1}{2L^{3/2}} \sum_{\mathbf{x}} e^{-i\mathbf{P}\cdot\mathbf{x}} \left(\bar{u}\Gamma u - \bar{d}\Gamma d \right) (t), \quad (3.1)$$

where Γ is a projector onto the spin structure or polarisation of the interpolator. In practice, we calculate the three orthogonal components for $\Gamma \in \{\gamma_1, \gamma_2, \gamma_3\}$ and also define another ρ interpolator with $\Gamma \in \{\gamma_0\gamma_1, \gamma_0\gamma_2, \gamma_0\gamma_3\}$.

We are studying the neutral ρ meson, which decays into two charged pions [5], $\rho^0 \rightarrow \pi^+\pi^-$. The two-pion operator we are using is consequently a product of π^+ and π^- interpolators and reads

$$(\pi\pi)(\mathbf{p}_1, \mathbf{p}_2, t) = \pi^+(\mathbf{p}_1, t)\pi^-(\mathbf{p}_2, t) - \pi^-(\mathbf{p}_1, t)\pi^+(\mathbf{p}_2, t), \quad (3.2)$$

where the momenta of the single pions add up to the frame momentum, $\mathbf{p}_1 + \mathbf{p}_2 = \mathbf{P}$. The single-pion interpolators are defined by

$$\pi^+(\mathbf{q}, t) = \frac{1}{2L^{3/2}} \sum_{\mathbf{x}} e^{-i\mathbf{q}\cdot\mathbf{x}} (\bar{u}\gamma_5 d)(\mathbf{x}, t), \quad (3.3)$$

$$\pi^-(\mathbf{q}, t) = \frac{1}{2L^{3/2}} \sum_{\mathbf{x}} e^{-i\mathbf{q}\cdot\mathbf{x}} (\bar{d}\gamma_5 u)(\mathbf{x}, t) \quad , \quad (3.4)$$

such that

$$(\pi\pi)(\mathbf{p}, t) = (\pi\pi)^\dagger(\mathbf{p}, t) \quad . \quad (3.5)$$

The explicit operator basis for the correlator matrix are the two rho-interpolators, Equation (3.1), with gamma insertions γ_i and $\gamma_0\gamma_i^1$, averaged over the three possible polarisations, plus the two-pion operators with different momenta combinations $(\mathbf{p}_1, \mathbf{p}_2)$, Equation (3.2). We can then build the correlator matrix

$$C(t) = \begin{pmatrix} \langle \rho(t)\rho^\dagger(0) \rangle & \langle \rho(t)(\pi\pi)^\dagger(0) \rangle \\ \langle (\pi\pi)(t)\rho^\dagger(0) \rangle & \langle (\pi\pi)(t)(\pi\pi)^\dagger(0) \rangle \end{pmatrix} \quad ,$$

where each element should be thought of as a matrix built by the respective operator basis. As an example, the explicit full operator basis in the CMF consists of

$$\begin{aligned} \rho_{1,i}(\mathbf{P} = 0, t) &= \frac{1}{2L^{3/2}} \sum_{\mathbf{x}} e^{-i\mathbf{P}\cdot\mathbf{x}} \left(\bar{u}(\gamma_i)u - \bar{d}(\gamma_i)d \right) (t) \quad , \\ \rho_{2,i}(\mathbf{P} = 0, t) &= \frac{1}{2L^{3/2}} \sum_{\mathbf{x}} e^{-i\mathbf{P}\cdot\mathbf{x}} \left(\bar{u}(\gamma_0\gamma_i)u - \bar{d}(\gamma_0\gamma_i)d \right) (t) \quad , \\ (\pi\pi)_{1,i}(\mathbf{P} = 0, t) &= \frac{1}{2} \sum_{\mathbf{p} \in P_1} \pi^+(\mathbf{p}, t)\pi^-(-\mathbf{p}, t) - \pi^-(\mathbf{p}, t)\pi^+(-\mathbf{p}, t) \quad , \\ (\pi\pi)_{2,i}(\mathbf{P} = 0, t) &= \frac{1}{8} \sum_{\mathbf{p} \in P_2} \pi^+(\mathbf{p}, t)\pi^-(-\mathbf{p}, t) - \pi^-(\mathbf{p}, t)\pi^+(-\mathbf{p}, t) \quad , \\ (\pi\pi)_{3,i}(\mathbf{P} = 0, t) &= \frac{1}{8} \sum_{\mathbf{p} \in P_3} \pi^+(\mathbf{p}, t)\pi^-(-\mathbf{p}, t) - \pi^-(\mathbf{p}, t)\pi^+(-\mathbf{p}, t) \quad , \end{aligned}$$

with $P_j = \{\mathbf{p} | \mathbf{p}^2 = j, \mathbf{p} \cdot \mathbf{e}_i \neq 0\}$, the single-pion interpolators defined in Equation (3.4) and where the index i is the polarisation of the operator. By averaging over this polarisation index, the full 5×5 correlator matrix is formed:

$$C(\mathbf{P} = 0, t) = \begin{pmatrix} \langle \rho_1(t)\rho_1^\dagger(0) \rangle & \langle \rho_1(t)\rho_2^\dagger(0) \rangle & \langle \rho_1(t)(\pi\pi)_1^\dagger(0) \rangle & \langle \rho_1(t)(\pi\pi)_2^\dagger(0) \rangle & \langle \rho_1(t)(\pi\pi)_3^\dagger(0) \rangle \\ \langle \rho_2(t)\rho_1^\dagger(0) \rangle & \langle \rho_2(t)\rho_2^\dagger(0) \rangle & \langle \rho_2(t)(\pi\pi)_1^\dagger(0) \rangle & \langle \rho_2(t)(\pi\pi)_2^\dagger(0) \rangle & \langle \rho_2(t)(\pi\pi)_3^\dagger(0) \rangle \\ \langle (\pi\pi)_1(t)\rho_1^\dagger(0) \rangle & \langle (\pi\pi)_1(t)\rho_2^\dagger(0) \rangle & \langle (\pi\pi)_1(t)(\pi\pi)_1^\dagger(0) \rangle & \langle (\pi\pi)_1(t)(\pi\pi)_2^\dagger(0) \rangle & \langle (\pi\pi)_1(t)(\pi\pi)_3^\dagger(0) \rangle \\ \langle (\pi\pi)_2(t)\rho_1^\dagger(0) \rangle & \langle (\pi\pi)_2(t)\rho_2^\dagger(0) \rangle & \langle (\pi\pi)_2(t)(\pi\pi)_1^\dagger(0) \rangle & \langle (\pi\pi)_2(t)(\pi\pi)_2^\dagger(0) \rangle & \langle (\pi\pi)_2(t)(\pi\pi)_3^\dagger(0) \rangle \\ \langle (\pi\pi)_3(t)\rho_1^\dagger(0) \rangle & \langle (\pi\pi)_3(t)\rho_2^\dagger(0) \rangle & \langle (\pi\pi)_3(t)(\pi\pi)_1^\dagger(0) \rangle & \langle (\pi\pi)_3(t)(\pi\pi)_2^\dagger(0) \rangle & \langle (\pi\pi)_3(t)(\pi\pi)_3^\dagger(0) \rangle \end{pmatrix} \quad .$$

In other frames and irreducible representations, the correlator matrix is built according to the prescription described in Section 3.2. We are computing the correlation functions for all possible moving frames which share a value of \mathbf{P}^2 but are oriented in different directions and then average over them.

We also need lattice currents for our work, in particular for the extraction of the timelike pion form factor and for the calculation of the long-time contri-

¹On E5, we are only using a single ρ interpolator with a γ_i insertion.

bution to the hadronic vacuum polarisation. The local vector current is given by

$$J_\mu^l(n) = \bar{\psi}(n)\gamma_\mu\psi(n), \quad (3.6)$$

where $\psi(n)$ is a (mass-degenerate) doublet of u and d quarks. This current is not conserved for Wilson fermions. Furthermore, this bare current has to be renormalised with a renormalisation constant Z_V . For the construction of a conserved vector current, we have to consider an infinitesimal symmetry transformation of the fermion fields [28]

$$\psi(n) \rightarrow \psi(n) + \delta\psi(n), \quad (3.7)$$

$$\bar{\psi}(n) \rightarrow \bar{\psi}(n) + \delta\bar{\psi}(n), \quad (3.8)$$

and demand that this transformation leaves the result of a path integral invariant. The explicit transformation we consider is the vector transformation

$$\psi(n) \rightarrow \psi'(n) = e^{i\epsilon}\psi(n), \quad (3.9)$$

$$\bar{\psi}(n) \rightarrow \bar{\psi}'(n) = \bar{\psi}(n)e^{-i\epsilon}, \quad (3.10)$$

which is a symmetry of the QCD lattice action for arbitrary quark masses. The corresponding infinitesimal transformations we are considering here are

$$\psi(n) \rightarrow \psi'(n) = (1 + i\epsilon(n)\tau^a)\psi(n), \quad (3.11)$$

$$\bar{\psi}(n) \rightarrow \bar{\psi}'(n) = \bar{\psi}(n)(1 - i\epsilon(n)\tau^a), \quad (3.12)$$

where τ^a are the Pauli $SU(2)$ matrices. Applying this transformation to the fermion action (1.24) and only considering terms up to $\mathcal{O}(\epsilon)$, we obtain

$$\delta S = i \sum_{n,m} \bar{\psi}(n) \left(D_{n,m}\epsilon(m)\tau^a - \epsilon(n)\tau^a D_{n,m} \right) \psi(m). \quad (3.13)$$

Considering the Dirac operator for Wilson fermions (Equation (1.30)) we obtain

$$\begin{aligned} \delta S = & i \sum_n \bar{\psi}(n) \left(\left[\left(\mathcal{M} + \frac{4}{a} \right), \epsilon(n)\tau^a \right] \right) \psi(n) \\ & - \frac{i}{2a} \sum_n \bar{\psi}(n) \sum_{\mu=\pm 1}^{\pm 4} (1 - \gamma_\mu) U_\mu(n) \epsilon(n) \tau^a \psi(n + \hat{\mu}) \\ & + \frac{i}{2a} \sum_n \bar{\psi}(n) \sum_{\mu=\pm 1}^{\pm 4} \epsilon(n + \hat{\mu}) \tau^a (1 - \gamma_\mu) U_\mu(n) \psi(n + \hat{\mu}). \end{aligned} \quad (3.14)$$

Because we are working only with two light flavours in the isospin limit, the mass matrix \mathcal{M} commutes with τ^a , such that the first term vanishes. By explicitly

writing the sums only over positive directions of μ , remembering that $\gamma_{-\mu} = -\gamma_\mu$ and then shifting the lattice site summation index $n \rightarrow n + \pm\hat{\mu}$, so that in each term the lattice site of ϵ is the same, we arrive at

$$\begin{aligned}
\delta S = & -\frac{i}{2a} \sum_n \sum_{\mu=1}^4 \bar{\psi}(n) (1 - \gamma_\mu) U_\mu(n) \epsilon(n) \tau^a \psi(n + \hat{\mu}) \\
& -\frac{i}{2a} \sum_n \sum_{\mu=1}^4 \bar{\psi}(n) (1 + \gamma_\mu) U_\mu(n - \hat{\mu})^\dagger \epsilon(n) \tau^a \psi(n - \hat{\mu}) \\
& +\frac{i}{2a} \sum_n \sum_{\mu=1}^4 \bar{\psi}(n - \hat{\mu}) \epsilon(n) \tau^a (1 - \gamma_\mu) U_\mu(n) \psi(n) \\
& +\frac{i}{2a} \sum_n \sum_{\mu=1}^4 \bar{\psi}(n + \hat{\mu}) \epsilon(n) \tau^a (1 + \gamma_\mu) U_\mu(n)^\dagger \psi(n). \tag{3.15}
\end{aligned}$$

We can now demand that this variation has to vanish for arbitrary $\epsilon(n)$. With the definition of the conserved current

$$J_{\mu,a}^c(n) = \frac{1}{2} (\bar{\psi}(n + \hat{\mu}) (1 + \gamma_\mu) U_\mu(n)^\dagger \tau^a \psi(n) - \bar{\psi}(n) (1 - \gamma_\mu) U_\mu(n) \tau^a \psi(n + \hat{\mu})), \tag{3.16}$$

we can rewrite the equation for δS as

$$\sum_{\mu=1}^4 (J_{\mu,a}^c(n) - J_{\mu,a}^c(n - \hat{\mu})) = 0, \tag{3.17}$$

which shows that $J_{\mu,a}^c(n)$ is indeed a Noether current of the system.

Both the pointlike current, Equation (3.6), as well as the the point-split current, Equation (3.16), have $\mathcal{O}(a)$ discretisation effects. The renormalised $\mathcal{O}(a)$ improved version of the currents reads [72, 73]

$$J_{\mu,a,R}^{l/c}(n) = Z_V (1 + b_V am_q) \left(J_{\mu,a}^{l/c}(n) + ac_V \partial_V T_{\mu\nu}(n) \right), \tag{3.18}$$

with the improvement coefficients b_V, c_V ($b_V = 1$ for the point-split current), the bare subtracted quark mass am_q and the tensor current

$$T_{\mu\nu}(n) = \frac{1}{2} \bar{\psi}(n) [\gamma_\mu, \gamma_\nu] \psi(n). \tag{3.19}$$

3.2 Moving frames and irreducible representations

In continuum QCD and also in infinite volume, the three-dimensional rotational symmetry in space classifies energy eigenstates. Any multiplet of degenerate

states due to this rotational symmetry can be described by the infinite number of *irreducible representations* (irreps) labelled by different spins J [74]. In Lattice QCD, due to the Euclidean grid there are less symmetries than in the continuum or infinite volume: In the CMF, the allowed spatial momenta \mathbf{p} in the box are restricted due to the periodic boundary conditions which we use in our ensembles to

$$\mathbf{p} = \frac{2\pi}{L}(k, l, m), \quad k, l, m \in \{0, 1, \dots, L/a - 1\}. \quad (3.20)$$

The symmetry group of the lattice is that one of a cube, called the cubic symmetry group or the octahedral group. Any continuum operator O^J with spin J must be *subduced* [74] into the respective irreps Λ via

$$O_{\Lambda, \mu}^{[J]} = \sum_M \mathcal{S}_{\Lambda, \mu}^{J, M} O^{J, M}, \quad (3.21)$$

where M are the magnetic quantum numbers of J , $\mathcal{S}_{\Lambda, \mu}^{J, M}$ is the subduction coefficient and μ is the row of the finite volume irrep Λ . The J in $O_{\Lambda, \lambda}^{[J]}$ is in brackets because, although it was produced only from operators with spin J , the operator can now have an overlap with all other spins which are contained in Λ [75]. In the moving frames, there is a further reduction of symmetry, namely into the subgroup of the octahedral group which keeps \mathbf{P} invariant [75], which is referred to as the little group [76]. In order to subduce continuum operators into the lattice irreps of the moving frame, we first need to create helicity operators

$$O^{J, \lambda}(\mathbf{p}) = \sum_M \mathcal{D}_{M\lambda}^{(J)*}(R) O^{J, M}(\mathbf{p}), \quad (3.22)$$

where λ is the helicity index, $\mathcal{D}_{M\lambda}^{(J)*}(R)$ is a *Wigner-D matrix* [77] for the transformation R which rotates $|\mathbf{p}\hat{\mathbf{e}}_z$ into \mathbf{p} [78]. This helicity λ can now be subduced into little group irreps Λ , forming a so-called *subduced helicity operator*

$$O_{\Lambda, \mu}^{J, P, |\lambda|}(\mathbf{p}) = \sum_{\hat{\lambda}=\pm\lambda} \mathcal{S}_{\Lambda, \mu}^{\tilde{\eta}\hat{\lambda}} O^{J, P, \hat{\lambda}}(\mathbf{p}), \quad (3.23)$$

where P is the parity of $O^{J, P, \hat{\lambda}}(\mathbf{p} = 0)$ and $\tilde{\eta} = P(-1)^J$. Subducing the meson-meson operators used in this study into irreps needs one further symmetry to be taken into account: Because we work in the isospin limit, the π^+ and π^- in the $\pi\pi$ state are of equal mass and differ only in their conjugated charge. The system thus has a symmetry under the interchange of the two pions, allowing only odd partial waves [79]. Taking all these reductions of symmetry into account, the relevant irreps of the $\rho \rightarrow \pi\pi$ channel, where $J^P = 1^-$ and where $l = 1$ is the dominant contributing partial wave are listed in Table 3.1. A general $\pi\pi$

\mathbf{P}	$\Lambda(\dim(\Lambda))$
[000]	$T_1(3)$
[00n]	$A_1(1), E(2)$
[0nn]	$A_1(1), B_1(1), B_2(1)$
[nnn]	$A_1(1), E(2)$

Table 3.1: Irreps in the various moving frames used in this study.

creation operator in an irrep Λ can be written [75]

$$(\pi\pi)_{\mathbf{P},\Lambda,\mu}^{[\mathbf{p}_1,\mathbf{p}_2]^\dagger} = \sum_{\substack{\mathbf{p}_1 \in \{\mathbf{p}_1\}^* \\ \mathbf{p}_2 \in \{\mathbf{p}_2\}^* \\ \mathbf{p}_1 + \mathbf{p}_2 = \mathbf{P}}} = \mathcal{C}(\mathbf{P}, \Lambda, \mu, \mathbf{p}_1, \mathbf{p}_2) \pi^\dagger(\mathbf{p}_1) \pi^\dagger(\mathbf{p}_2), \quad (3.24)$$

where the set $\{\mathbf{p}_{1,2}\}^*$ incorporates all the momenta that $\mathbf{p}_{1,2}$ can be rotated into using an allowed lattice rotation. \mathcal{C} is a Clebsch-Gordan coefficient which couples the irreps Λ_1 and Λ_2 of the single-pion creation operators $\pi^\dagger(\mathbf{p})$ with the irrep Λ of the $(\pi\pi)^\dagger$ operator. These single-pion irreps are either the cubic group for $\mathbf{p} = 0$ or the A_2 irrep of the little group of \mathbf{p} for $\mathbf{p} \neq 0$. The coefficients relevant for this work are listed in [75, 80].

3.3 Lüscher's finite volume method

We have noted at some stages already that the reason for extracting the energy spectrum of the ρ and $\pi\pi$ isospin = 1 states is that we want to use them to obtain infinite-volume scattering information of the ρ resonance. In this chapter we will finally explain in more detail how this connection works.

Resonances are composite states which are unstable and thus decay into other states of QCD and as such are more difficult to study than QCD-stable states. In fact, we can only directly access stable states in Lattice QCD: A fundamental part of the lattice approach is to Wick-rotate Minkowski time into imaginary time to assure an Euclidean geometry. In continuum QCD, the Osterwalder-Schrader-theorem [81] allows Euclidean correlation functions to be continued back into Minkowski space, given that they obey several conditions, one of them being the so-called *reflection positivity*. Because observables like the Euclidean correlation functions computed in Lattice QCD have to be discrete and are only approximate, we cannot simply map them back to Minkowski space via an analytic continuation. One of the consequences of this is that we cannot extract physical matrix elements from any simulation in Lattice QCD which deals with multiple particles in the initial or final state. This is formulated in the *Maiani-Testa theorem* [82]. Accordingly, we cannot directly access scattering information for any dynamical process, like a resonance, using Lattice QCD. In other words, the only energy states which we can reliably extract using Lattice

QCD are asymptotic states. A circumvention of this problem comes directly from the finite volume [1, 2], which is necessarily used in Lattice QCD. In a typical lattice finite volume of a few fermis, the energy states in the discrete two-pion energy spectrum are quite far apart from each other. The Maiani-Testa theorem however applies principally only to infinite or very large lattices, where the final states have a continuous spectrum – and precisely this non-continuity of the spectrum actually allows to map the finite-volume spectrum to the infinite-volume resonance [83].

The insight that two-pion scattering, or any process involving multi-hadron states has calculable power-law corrections can now be used as a tool to obtain infinite-volume resonance information. Lüscher’s work was initially done only for the centre-of-mass frame [1, 2], but has been extended to moving frames [84]. In [85], the result was re-derived using a quantum-field-theory language involving a diagrammatic expansion which illustrates the key points of the Lüscher approach. For the introduction of the approach in this thesis, we will follow the arguments outlined in [86], which deals with two-particle scattering in a very general way. We also use the notation employed in this reference. The main idea is to decompose the two-to-two finite-volume correlator

$$C_L(P) \equiv \int_L d^4x e^{-iPx} \left[\langle 0 | T \mathcal{A}(x) \mathcal{B}^\dagger(0) | 0 \rangle \right]_L, \quad (3.25)$$

where T is a time-ordering operator and $\mathcal{A}(x), \mathcal{B}(x)$ are operators coupling to $\pi\pi$ states, into products of finite- and infinite-volume quantities. To this end, this correlator is expanded into a skeleton expansion, where only two-particle states can go on-shell. This expansion includes Bethe-Salpeter kernels, which do include any diagrams without on-shell states, alternating with two-particle loops,

$$C_L(P) = \begin{array}{c} \textcircled{\mathcal{A}} \textcircled{V} \textcircled{\mathcal{B}^\dagger} + \textcircled{\mathcal{A}} \textcircled{V} \textcircled{\bullet} \textcircled{V} \textcircled{\mathcal{B}^\dagger} \\ + \textcircled{\mathcal{A}} \textcircled{V} \textcircled{\bullet} \textcircled{V} \textcircled{\bullet} \textcircled{V} \textcircled{\mathcal{B}^\dagger} + \dots \end{array} \quad (3.26)$$

The V in this equation in between the two-particle loops indicates a sum over admissible finite-volume momenta in the loop. As opposed to the Bethe-Salpeter kernels, the two-particle loops can go on-shell. This skeleton-expansion is advantageous, because for the pole-free parts of the skeleton-expansion, the difference between infinite and finite volume is exponentially suppressed, as has been shown in [85]. Consequently, all relevant finite-volume corrections must be in the explicit two-particle loops of the diagram (as long as $\mathcal{A}(x), \mathcal{B}^\dagger(x)$ are chosen in a way that they do not introduce any additional finite-volume effects). The difference between the infinite-volume and finite-volume two-particle loop can

then be identified as some finite-volume residue

$$\mathcal{F}_L = \left[\frac{1}{L^3} \sum_{\mathbf{k}} - \int \frac{d\mathbf{k}}{(2\pi)^3} \right] \int \frac{dk_4}{2\pi} \mathcal{L}(P, k) \mathcal{S}(k) \mathcal{R}^\dagger(P, k), \quad (3.27)$$

where L is the box size of the lattice, and \mathcal{L} and \mathcal{R}^\dagger can be arbitrary, smooth end-cap functions and in this case are either a Bethe-Salpeter kernel or $\mathcal{A}(x)$ or $\mathcal{B}^\dagger(x)$. $\mathcal{S}(k)$ is the product of the two propagators, i.e. the two-particle loop. The finite-volume dependence of the residue factorises as

$$\mathcal{F}_L = -\mathcal{L}(P) F(P, L) \mathcal{R}^\dagger(P), \quad (3.28)$$

where $F(P, L)$ is the finite-volume residue factor which is simply a finite-volume matrix and $\mathcal{L}, \mathcal{R}^\dagger$ are now row- and column vectors, respectively. In this step, exponentially suppressed terms arising from the evaluation of the k_4 integral have been discarded. Finally, the finite-volume sums in the skeleton expansion are replaced by an infinite volume integrals plus the residues containing F , which can be written in the diagrammatic way via

$$\begin{array}{c} \circlearrowleft \mathcal{L} \quad V \quad \mathcal{R}^\dagger \circlearrowright \\ \circlearrowleft \mathcal{L} \quad \infty \quad \mathcal{R}^\dagger \circlearrowright \\ \circlearrowleft \mathcal{L} \quad F \quad \mathcal{R}^\dagger \circlearrowright \end{array} = \begin{array}{c} \circlearrowleft \mathcal{L} \quad \infty \quad \mathcal{R}^\dagger \circlearrowright \\ \circlearrowleft \mathcal{L} \quad F \quad \mathcal{R}^\dagger \circlearrowright \end{array} . \quad (3.29)$$

This expression can be reorganised into terms grouped according to their number of finite-volume residues F . The terms without finite-volume insertions, i.e. the Bethe-Salpeter kernels and *infinite volume* two-particle states, are resummed and yield the scattering amplitude \mathcal{M} :

$$\begin{array}{c} \circlearrowleft \mathcal{M} \circlearrowright \\ \circlearrowleft \bullet \circlearrowright \\ \circlearrowleft \bullet \quad \infty \quad \bullet \circlearrowright \\ \circlearrowleft \bullet \quad \infty \quad \bullet \quad \infty \quad \bullet \circlearrowright \\ \dots \end{array} = \begin{array}{c} \circlearrowleft \bullet \circlearrowright \\ \circlearrowleft \bullet \quad \infty \quad \bullet \circlearrowright \\ \circlearrowleft \bullet \quad \infty \quad \bullet \quad \infty \quad \bullet \circlearrowright \\ \dots \end{array} + \dots . \quad (3.30)$$

The dressed end-cap functions A, B , which are equal in infinite and finite volume up to exponential suppressions are given by

$$\begin{array}{c} \circlearrowleft A \circlearrowright \\ \circlearrowleft A \circlearrowright \\ \circlearrowleft A \quad \infty \quad \mathcal{M} \circlearrowright \end{array} = \begin{array}{c} \circlearrowleft A \circlearrowright \\ \circlearrowleft A \circlearrowright \\ \circlearrowleft A \quad \infty \quad \mathcal{M} \circlearrowright \end{array} , \quad (3.31)$$

$$\begin{array}{c} \circlearrowright B^\dagger \circlearrowleft \\ \circlearrowright B^\dagger \circlearrowleft \\ \mathcal{M} \circlearrowleft \quad \infty \quad B^\dagger \circlearrowleft \end{array} = \begin{array}{c} \circlearrowright B^\dagger \circlearrowleft \\ \circlearrowright B^\dagger \circlearrowleft \\ \mathcal{M} \circlearrowleft \quad \infty \quad B^\dagger \circlearrowleft \end{array} . \quad (3.32)$$

With these definitions, A, B and \mathcal{M} are infinite-volume objects and all finite-volume corrections are explicit in the F insertions. The resulting diagrams can

be summed into a geometric series in $\mathcal{M}F$,

$$\begin{aligned}
C_L(P) - C_\infty(P) = & \text{Diagram 1} + \text{Diagram 2} \\
& + \text{Diagram 3} + \dots \quad (3.33)
\end{aligned}$$

The diagrams represent terms in a geometric series. Diagram 1 is a circle with nodes A and B†, with an arc labeled F between them. Diagram 2 is a circle with nodes A and B†, with two arcs labeled F and M between them. Diagram 3 is a circle with nodes A and B†, with three arcs labeled F, M, and F between them. Ellipses indicate further terms in the series.

which leads to the final expression for the finite-volume correlator

$$C_L(P) = C_\infty(P) - A(P) \frac{1}{F^{-1}(P, L) + \mathcal{M}(P)} B^\dagger(P). \quad (3.34)$$

The finite-volume correlation function, $C_L(P)$ has poles at the energies of the respective finite-volume theory. On the right-hand side of this equation, neither $C_\infty(P)$ nor $A(P)$ or $B^\dagger(P)$ have any such poles and consequently all poles in $C_L(P)$ must correspond to divergent eigenvalues in the matrix $\frac{1}{F^{-1}(P, L) + \mathcal{M}(P)}$. This requirement is equivalent to the two-particle quantisation condition

$$\det[F^{-1}(P, L) + \mathcal{M}(P)] = 0. \quad (3.35)$$

This is the equation which we have been looking for: It relates the energy spectrum (for any fixed box size L and momentum \mathbf{P}) to the scattering amplitude \mathcal{M} through the kinematical function F . The explicit relation of the finite- and infinite-volume correlation functions is achieved by evaluating the Fourier transformed correlator

$$C_L(x_4 - y_4, \mathbf{P}) = \int_L d\mathbf{x} \int_L d\mathbf{y} e^{-i\mathbf{P}(\mathbf{x}-\mathbf{y})} \left[\langle 0 | T \mathcal{A}(x) \mathcal{B}^\dagger(0) | 0 \rangle \right]_L, \quad (3.36)$$

in two different ways. Because the translation operators cancel the Fourier-phase factors, it turns out that the integrand does not depend on \mathbf{x} or \mathbf{y} and that the whole expression can simply be written in terms of the spectral decomposition of the correlator like in Equation (2.4):

$$C_L(x_4 - y_4, \mathbf{P}) = L^6 \sum_n e^{-E_n(x_4 - y_4)} \left[\langle 0 | \mathcal{A}(0) | E_n, \mathbf{P}, L \rangle \right]_L \left[\langle E_n, \mathbf{P}, L | \mathcal{B}^\dagger(0) | 0 \rangle \right]_L. \quad (3.37)$$

The Fourier-transformed correlator can also be evaluated directly using Equation (3.34):

$$\begin{aligned}
C_L(x_4 - y_4, \mathbf{P}) & \equiv L^3 \int \frac{dP_4}{2\pi} e^{iP_4(x_4 - y_4)} C_L(P) \\
& = L^3 \int \frac{dP_4}{2\pi} e^{iP_4(x_4 - y_4)}
\end{aligned}$$

$$\begin{aligned}
& \times \left[C_\infty(P) - A(P) \frac{1}{F^{-1}(P, L) + \mathcal{M}(P)} B^\dagger(P) \right] \\
& = L^3 \sum_n e^{-E_n(x_4 - y_4)} \\
& \times \langle 0 | \mathcal{A}(0) | E_n, \mathbf{P}, \text{in} \rangle \mathcal{R}(E_n, \mathbf{P}) \langle E_n, \mathbf{P}, \text{out} | \mathcal{B}^\dagger(0) | 0 \rangle,
\end{aligned} \tag{3.38}$$

with

$$\mathcal{R}(E_n, \mathbf{P}) = \lim_{P_4 \rightarrow E_n} \left[- (iP_4 + E_n) \frac{1}{F^{-1}(P, L) + \mathcal{M}(P)} \right], \tag{3.39}$$

the residue of the matrix between $A(P)$ and $B^\dagger(P)$, evaluated at the n^{th} two-particle energy E_n . Both evaluations of Equations (3.38) and (3.39) assume that $x_4 > y_4$. In the former, it is needed when applying the time-ordering operator, and in the latter it allows for the contour to be closed in the upper P_4 plane. The sum results from the poles encircled by the contour corresponding to the finite-volume energies on the imaginary axis. A comparison of these two equations finally leads to

$$\begin{aligned}
& \left[\langle 0 | \mathcal{A}(0) | E_n, \mathbf{P}, L \rangle \right]_L \left[\langle E_n, \mathbf{P}, L | \mathcal{B}^\dagger(0) | 0 \rangle \right]_L = \\
& \frac{1}{L^3} \langle 0 | \mathcal{A}(0) | E_n, \mathbf{P}, \text{in} \rangle \mathcal{R}(E_n, \mathbf{P}) \langle E_n, \mathbf{P}, \text{out} | \mathcal{B}^\dagger(0) | 0 \rangle,
\end{aligned} \tag{3.40}$$

which is the desired relation between finite-volume and infinite-volume matrix elements, up to exponentially suppressed corrections in e^{-mL} . It is important to stress that Equation (3.35) and consequently also (3.40) are valid only below the lowest three or four-particle threshold. For the purpose of this work, where we study the $\rho \rightarrow \pi\pi$ channel, this threshold is the four-pion threshold. A three-pion state is excluded in this channel due to G-parity, which decouples states with even and odd numbers of pions.

3.4 Explicit formulae for $\pi\pi$ scattering

We stress again that Equations (3.35) and (3.40) are valid only for systems with only two particles which can go on-shell. For the further discussion, we will specifically cover the case of $\rho \rightarrow \pi\pi$ scattering. The whole discussion can be generalised to two particles of different masses [87] but for the purpose of this project we only need to consider equal masses. In a moving frame with total momentum $\mathbf{P} = \frac{2\pi}{L} \mathbf{d}$, the relative velocity

$$\mathbf{v} = \frac{\mathbf{P}}{E}, \tag{3.41}$$

relates the energy E in the moving frame to the centre-of-mass energy E_{cm} via

$$E = \gamma E_{\text{cm}}, \quad \gamma = \frac{1}{\sqrt{1 - |\mathbf{v}|^2}}, \quad (3.42)$$

or equivalently

$$E_{\text{cm}} = \sqrt{E^2 - \mathbf{P}^2}. \quad (3.43)$$

The relative momentum in the centre-of-mass frame is given by

$$q = \sqrt{\frac{E^2}{4} - m_\pi^2}. \quad (3.44)$$

In the CMF, the elastic scattering amplitude \mathcal{M} is fully diagonal and can be described by a single phase:

$$\mathcal{M}_{l_1, m_1; l_2, m_2} = \delta_{l_1, l_2} \delta_{m_1, m_2} \frac{16\pi E_{\text{cm}}}{q} \frac{e^{2i\delta_l(q)} - 1}{2i}, \quad (3.45)$$

with the phase shift $\delta_l(q)$ in the l^{th} partial wave. The matrix F in this basis reads

$$F_{l_1, m_1; l_2, m_2} = \frac{q}{8\pi E_{\text{cm}}} (\delta_{l_1, l_2} \delta_{m_1, m_2} + i F_{l_1, m_1; l_2, m_2}^{FV}), \quad (3.46)$$

$$F_{l_1, m_1; l_2, m_2}^{FV} = -\frac{4\pi}{q} \sum_{l=0}^{\infty} \sum_{m=-l}^l \frac{4\pi}{q^l} c_{lm}^P(q^2) \int d\Omega^* Y_{l_1, m_1}^* Y_{l, m}^* Y_{l_2, m_2}, \quad (3.47)$$

where $Y_{l, m}(\theta, \psi)$ are the spherical harmonics and $c_{lm}^P(q^2)$ is a known kinematical function which is related to the Lüscher modified zeta function $Z_{lm}^d[s, q^2]$ [1, 2]

$$c_{lm}^P(q^2) = -\frac{\sqrt{4\pi}}{\gamma L^3} \left(\frac{2\pi}{L}\right)^{l-2} Z_{lm}^d\left[1, \left(\frac{qL}{2\pi}\right)^2\right], \quad (3.48)$$

$$Z_{lm}^d[s, q^2] = \sum_{\mathbf{r} \in P_d} \frac{\mathcal{Y}_{lm}}{(r^2 - q^2)^s}, \quad (3.49)$$

$$\mathcal{Y}_{lm} = r^l Y_{lm}(\theta, \psi). \quad (3.50)$$

P_d is a set of vectors given by

$$P_d = \{\mathbf{r} | \mathbf{r} = \hat{\gamma}^{-1} \mathbf{n}, \mathbf{n} \in \mathbb{Z}^3\}, \quad (3.51)$$

where $\hat{\gamma}$ is the operator which Lorentz transforms a vector \mathbf{u} from a system with velocity \mathbf{v} (see Equation (3.41)) to the centre-of-mass frame via

$$\hat{\gamma} \mathbf{u} = \gamma \mathbf{u}_{\parallel} + \mathbf{u}_{\perp}, \quad \hat{\gamma}^{-1} \mathbf{u} = \gamma^{-1} \mathbf{u}_{\parallel} + \mathbf{u}_{\perp}, \quad (3.52)$$

with the parallel and perpendicular components of \mathbf{u}

$$\mathbf{u}_{\parallel} = \frac{\mathbf{u} \cdot \mathbf{v}}{|\mathbf{v}|^2} \mathbf{v}, \quad \mathbf{u}_{\perp} = \mathbf{u} - \mathbf{u}_{\parallel}. \quad (3.53)$$

One possible way to compute this numerically at least for sufficiently small values of l, m, \mathbf{d} is to use the formula [87, 88]

$$\begin{aligned} Z_{lm}^{\mathbf{d}}(1, q^2) = & \gamma \int_0^1 dt e^{tq^2} \sum_{\mathbf{n} \in \mathbb{Z}, \mathbf{n} \neq 0} (-i)^l \mathcal{Y}_{lm} \left(-\frac{\pi \hat{\gamma} \mathbf{n}}{t} \right) \left(-\frac{\pi}{t} \right)^{3/2} e^{-(\pi \gamma \mathbf{n})^2/t} \\ & + \gamma \left(\left(\int_0^1 dt (e^{tq^2} - 1) \left(-\frac{\pi}{t} \right)^{3/2} \frac{1}{\sqrt{4\pi}} \right) - \pi \right) \delta_{l0} \delta_{m0} \\ & + \sum_{\mathbf{r} \in P_{\mathbf{d}}} \mathcal{Y}_{lm}(\mathbf{r}) \frac{e^{-(r^2 - q^2)}}{(r^2 - q^2)^s}. \end{aligned} \quad (3.54)$$

Of course, the infinite sums need some finite cut-off and one has to verify that the asymptotic value is already approximated well enough for the precision aimed for in the study. We are studying the ρ and thus are interested in the p-wave $l = 1$ partial wave but in principle, we also have to deal with the contributions of higher-order partial waves. The effect of the $l = 3$ [11] and $l = 3, l = 5$ [89] partial waves has been studied by looking at irreps whose lowest angular momentum was $l = 3$ or $l = 5$. Both studies showed that we can neglect the effect of any partial waves above $l = 1$. With this restriction, the quantisation condition of Equation (3.34) can be rewritten

$$\delta(k) = \phi_{\Lambda}^{\mathbf{d}}(q) + n\pi, \quad (3.55)$$

where $k = \frac{2\pi}{L}q$. This is exactly the Lüscher condition, which includes as a special case also the CMF result, where the kinematical function $\phi(q)$ is defined as

$$\phi(q)_{\text{CMF}} = \phi_{T_1}^{[000]}(q) = -\frac{Z_{00}^{[000]}(1, q^2)}{\gamma \pi^{3/2} q}. \quad (3.56)$$

With the definition

$$w_{lm} = \frac{1}{\gamma \pi^{3/2} \sqrt{2l+1}} q^{-l-1} Z_{lm}^{\mathbf{d}}(1, q^2), \quad (3.57)$$

the functions $\phi_{\Lambda}^{\mathbf{d}}(q)$ can be succinctly written and are summarised in Table 3.2. We finally have all the ingredients for the whole Lüscher analysis: Given the energy spectrum from the GEVP in the different frames with momentum \mathbf{d} and irreps Λ , phase shift points $\delta(k)$ at the corresponding centre-of-mass energy can be computed. This phase shift encodes all the important scattering information of the $\rho \rightarrow \pi\pi$ process.

\mathbf{d}	Λ	$\phi_{\Lambda}^{\mathbf{d}}(q)$
[000]	T_1	w_{00}
[00n]	A_1	$w_{00} + 2w_{20}$
[00n]	E_2	$w_{00} - w_{20}$
[0nn]	A_1	$w_{00} + \frac{1}{2}w_{20} + i\sqrt{6}w_{21} - \sqrt{\frac{3}{2}}w_{22}$
[0nn]	B_1	$w_{00} + \frac{1}{2}w_{20} - i\sqrt{6}w_{21} - \sqrt{\frac{3}{2}}w_{22}$
[0nn]	B_2	$w_{00} - w_{20} + \sqrt{6}w_{22}$
[nnn]	A_1	$w_{00} - i\sqrt{\frac{8}{3}}w_{22} - \sqrt{\frac{8}{3}}\text{Re}(w_{21}) - \sqrt{\frac{8}{3}}\text{Im}(w_{21})$
[nnn]	E_2	$w_{00} + i\sqrt{6}w_{22}$

Table 3.2: Functions $\phi_{\Lambda}^{\mathbf{d}}(q)$ for different irreps Λ in several moving frames with lattice momentum \mathbf{d} . All of these functions are derived in [11].

Chapter 4

Numerical analysis of the spectrum

In this chapter, we will explain in detail how we are extracting the primary and secondary quantities from our lattice study. Towards extracting physical quantities, which can be compared to experimental results, a lot of systematic choices like fit ranges of different extraction methods have to be made and we will talk about the justification and the systematic effects of those choices in this chapter.

4.1 The pion mass

One of the fundamental quantities which we are extracting from our study and which is used in the entire calculation is the pion mass m_π . It is worth putting some effort into the determination of m_π for several reasons: First of all, the pion correlator has the most precise signal, with the exciting states falling off early due to the low mass of the pion. It has also been computed numerous times on the lattices used in this work, and as such provides a simple and basic cross-check of our methodology. Most importantly though, the pion mass is needed to compute most of the secondary quantities we are extracting from the lattice. Having a precise estimate of m_π on each jackknife sample helps dramatically to account for and alleviating some of the correlations between gauge configurations. The overall signal of m_π is comparably precise on each timeslice, but the variation of the signal between timeslices is quite pronounced, as can be seen in Figures 4.1, 4.2 and 4.3, where the pion correlator $\langle \pi(t)\pi^\dagger(0) \rangle$ and its effective mass are shown for lattices we use in this study. Particularly for F7, Figure 4.3, the fluctuations are visible in the effective mass.

To extract the pion mass from these correlators, we perform a correlated fit to a single-cosh ansatz

$$\langle \pi(t)\pi^\dagger(0) \rangle = C \cosh(m_\pi(t - T/2)). \quad (4.1)$$

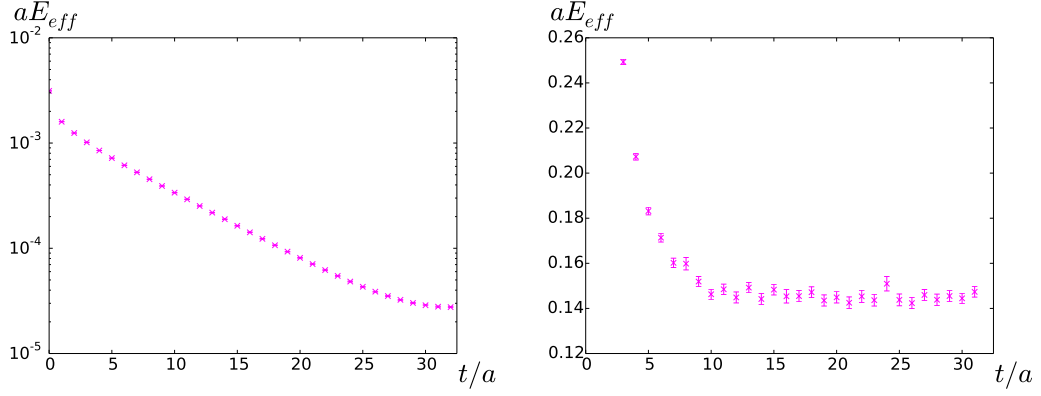


Figure 4.1: **Left panel:** The pion correlator $\langle \pi(t)\pi^\dagger(0) \rangle$ in the CMF on the E5 lattice. Forward- and backward-propagating waves are averaged and the error bars associated with the data come from a jackknife procedure. **Right panel:** Effective mass of the pion correlator shown on the left panel.

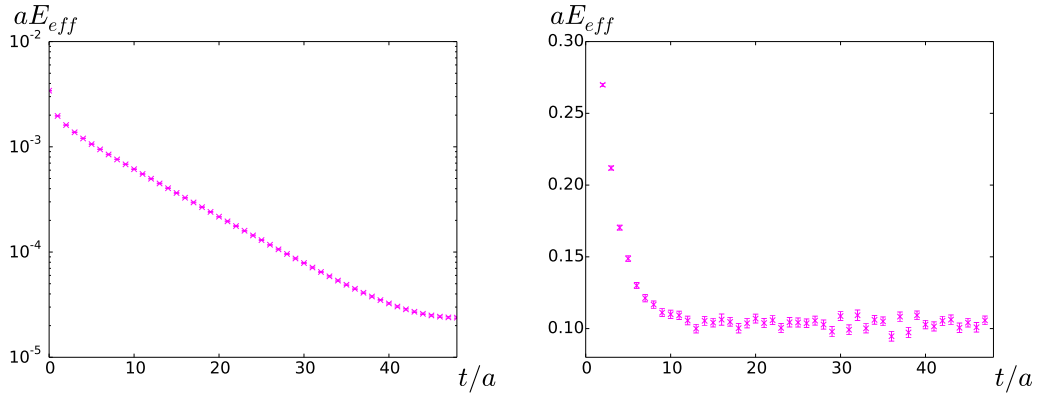


Figure 4.2: Same as Figure 4.1 but on the F6 lattice.

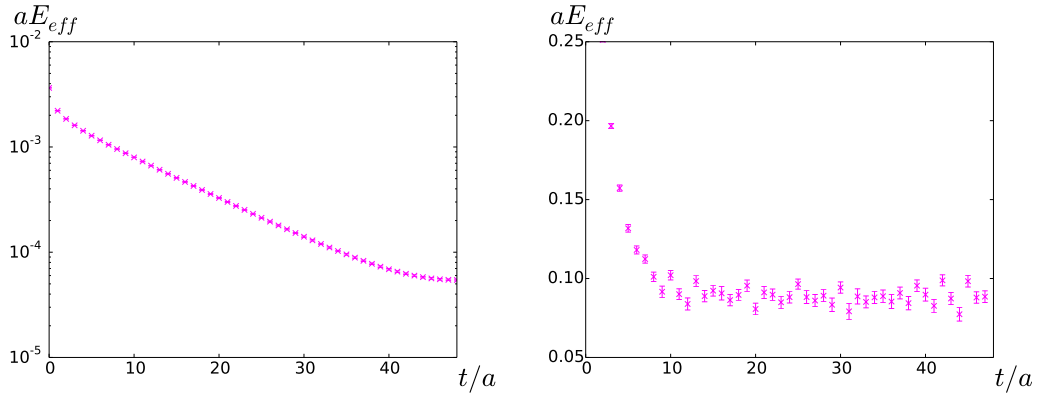


Figure 4.3: Same as Figure 4.1 but on the F7 lattice.

This fit function is motivated because the exponential decay of the correlation function from the source time happens in both directions from the source timeslice. Due to the periodic boundary conditions in our lattices, there is a forward-propagating part and a backward-propagating part. The superposition of those two forms a hyperbolic cosine centred about the temporal point furthest away from the source time, which is at $T/2$ with the source shifted to 0 (and periodically to T). The fit window $[t_{\min}, t_{\max}]$ for this fit must be chosen such that t_{\min} is large enough that excited states do not contribute to the fit any more and t_{\max} should be as large as possible, without getting into the regime where noise fluctuations affect the fit result. Figures 4.4, 4.5 and 4.6 show the fit results from a cosh fit to the pion correlator on the three ensembles. One can see how the fit stabilises with larger values of t_{\min} , and that for our chosen t_{\min} , the fit does not depend much on the choice of t_{\max} . On F7, the plateau does not look as nice as on E5 or F6 and becomes lower for larger choices of t_{\min} . When choosing $t_{\min} = 19$, which looks like a region where a plateau settles, the fit result varies much more than on E5 or F6 for a variation of t_{\max} and shows a clear trend towards higher values for larger t_{\max} . This is a result of the large correlations between timeslices and which is visible in Figure 4.3.

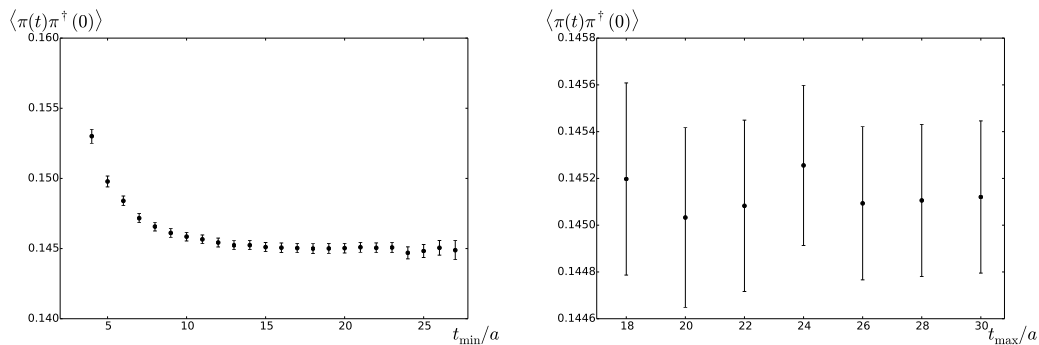


Figure 4.4: Pion mass obtained from several single-cosh fits to the pion correlator $\langle \pi(t)\pi^\dagger(0) \rangle$ on the E5 ensemble. The error bars associated with each fit result stem from a jackknife estimate. **Left panel:** Fit from various values of t_{\min} to $t_{\max} = 28$. **Right panel:** Fit from $t_{\min} = 15$ to various values of t_{\max} .

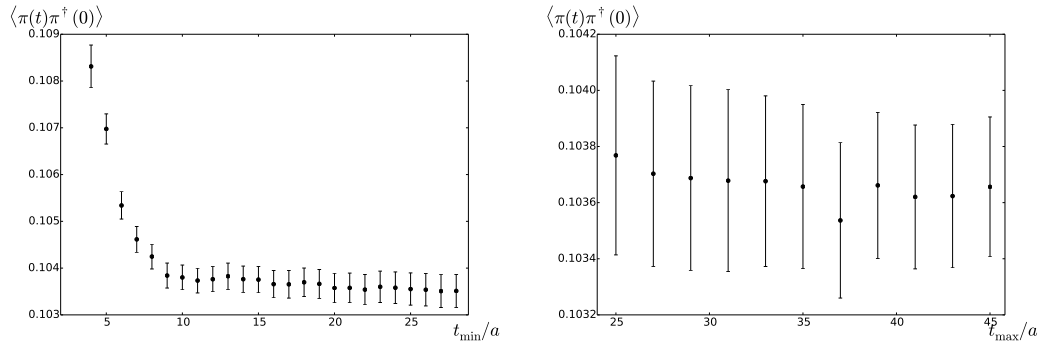


Figure 4.5: Same as Figure 4.4 but for the F6 lattice. **Left panel:** Fit from various values of t_{\min} to $t_{\max} = 35$. **Right panel:** Fit from $t_{\min} = 16$ to various values of t_{\max} .

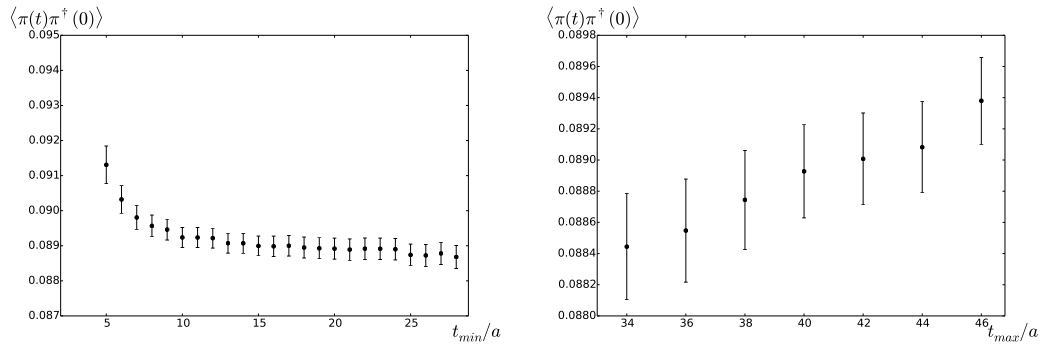


Figure 4.6: Same as Figure 4.4 but for the F7 lattice. **Left panel:** Fit from various values of t_{\min} to $t_{\max} = 40$. **Right panel:** Fit from $t_{\min} = 19$ to various values of t_{\max} .

In order to stabilise this fit, we would like the fit range to be as large as possible: With high values of t_{\max} , we can ensure that the correlations by timeslice level each other out as good as possible, and a low value for t_{\min} brings in valuable information on the signal from the early timeslices, where the signal is best. When going to earlier timeslices, we need to account for an excited state contamination in the fit range. On F7, we therefore also performed a fit to a two-cosh ansatz,

$$\langle \pi(t)\pi^\dagger(0) \rangle = C_1 \cosh(m_\pi(t - T/2)) + C_2 \cosh(\Delta E(t - T/2)), \quad (4.2)$$

where ΔE is the gap to the next excited state in the spectrum. With a plateau for a similar value of m_π , this fit reinforces the choice of $t_{\min} = 19$, as can be seen in Figure 4.7. All fit ranges and fit results are summarised in Table 4.1.

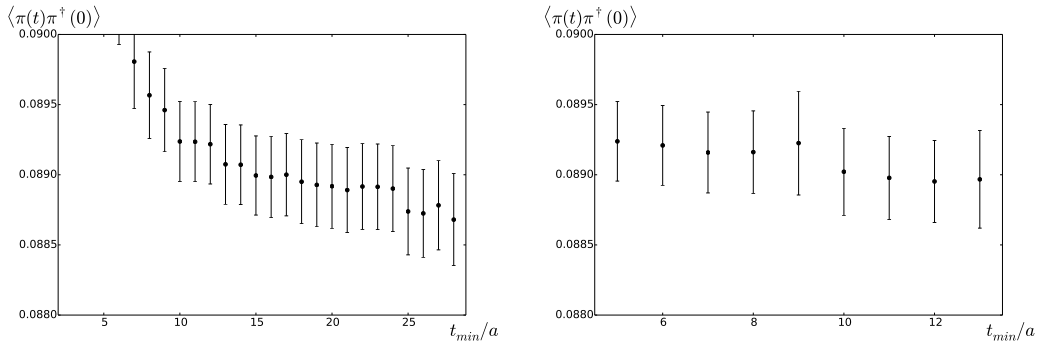


Figure 4.7: **Left panel:** Zoom of the left panel in Figure 4.6. **Right panel:** Two-cosh fit from various values of t_{\min} to $t_{\max} = 40$.

	fit	t_{\min}	t_{\max}	am_π	χ^2/dof
E5	1 – cosh	15	28	0.14511(33)	0.80
F6	1 – cosh	16	35	0.10366(29)	0.61
F7	1 – cosh	19	40	0.08893(30)	1.68
F7	2 – cosh	12	40	0.08895(29)	1.87

Table 4.1: Fit ranges to the single-cosh (and also two-cosh on F7) fit and corresponding pion masses including jackknife error on the three ensembles. On F7, the fit range of the 1-cosh fit was chosen so that the resulting pion mass is consistent with the less fluctuating pion mass of the two-cosh fit. The χ^2/dof value on F7 indicates as well that the data for the pion correlator is not perfect.

We also compared the pion mass fits in the different momentum frames we are using, which is shown in Figure 4.8. Boosted to their centre-of-mass energy via

$$E_{\text{cm}} = \sqrt{E^2 - \mathbf{P}^2}, \quad (4.3)$$

all pion masses agree within errors but the determination in the CMF is the

most precise one. For this reason we are using only the pion mass from the CMF for all further calculations in all momentum frames.

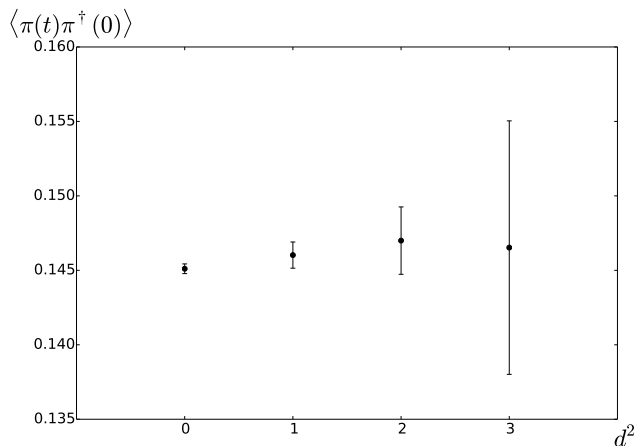


Figure 4.8: Pion mass obtained from the pion correlators in the different frames on the E5 lattice. All energies are boosted to the CMF energy, using the dispersion relation.

4.2 Energy spectrum from the GEVP

We will now move to the determination of the energy spectrum from the GEVP, defined in Equation (2.5). The first step is to build the correlation matrix $C(t)$ from the correlation functions defined in Section 3.1. The next steps depend on the choice of method for the GEVP. We will talk about the differences in the extraction of the energy spectrum using the fixed- t_0 method or the window method in this chapter.

4.2.1 Fixed- t_0 method

One way in which we solved the GEVP in our analysis is with a fixed t_0 , with a value of $t_0 = 3$. In each irrep, we obtain N eigenvalues from the GEVP of the $N \times N$ correlator matrix. The k^{th} eigenvalue $\lambda^{(k)}(t)$ decays exponentially with the k^{th} energy level E_k but also has some excited-state contribution. The effective mass, defined by Equation (2.7) illustrates this behaviour well: At early Euclidean times, the spectrum is dominated by excited states and at larger Euclidean times, where the lowest energy state dominates, the effective mass reaches a plateau. One possible way to extract the energy E_k is a constant fit to the effective mass or a single-exponential fit to the corresponding eigenvalue in a fit window which lies exclusively in the plateau region. With the statistical fluctuations between the data points, it is sometimes difficult to say where exactly the plateau region starts and whether some early timeslices might not still have some excited-state contribution in them. For this reason, we are

performing a two-exponential fit, accounting for a single excited state, in a fit window which starts already earlier than the plateau region. A fit window $[t_{\min}, t_{\max}]$ has to be chosen for every single level of the GEVP in every frame and irrep. The variation of t_{\min} is shown for some exemplifying energy levels in Figure 4.9. The same plot for all energy levels we used in the different frames and irreps is shown in the appendix in Figures A.1, A.3 and A.5. There are several considerations to be taken into account when choosing the appropriate fit range for each level. We decided on using a global lower fit parameter t_{\min} for each level in this method to assure that excited state effects are treated in the same way for each energy level obtained. The value we choose is $t_{\min} = 6$ on E5 and $t_{\min} = 7$ on F6 and F7, because a plateau seems to be reached in all levels at that point. The extracted energy levels using the fixed- t_0 method

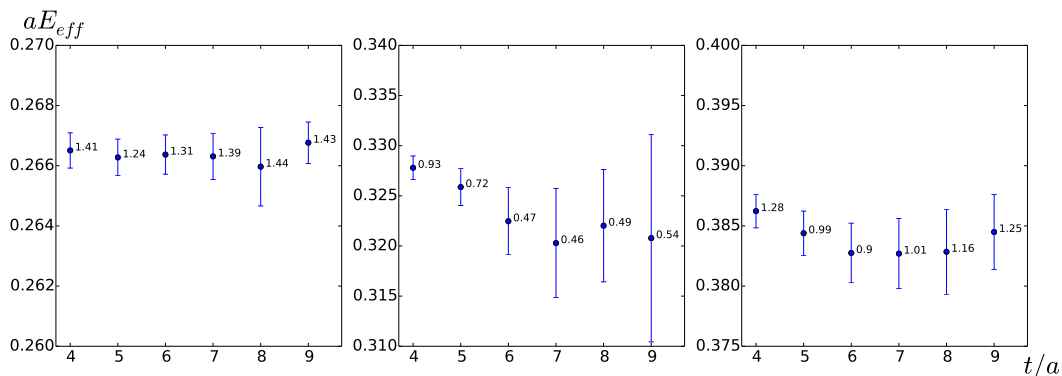


Figure 4.9: t_{\min} dependence of the fit to the three levels in the $d^2 = 1, A_1$ irrep on the F6 lattice extracted from the GEVP in the fixed- t_0 method using $t_0 = 3$. The left plot shows the ground state and the second and third plot are the first and second excited states, respectively. The horizontal axis denotes t_{\min}/a in the fit window and the vertical axis is the energy (in lattice units) of the state. The error associated with the data points comes from a jackknife procedure and the black number next to each data point is the associated χ^2/dof of the correlated fit.

are listed in Table 4.2. The extracted energy levels are shown together with the effective masses in Figure 4.10 for some irreps and in Appendix A.2 for all irreps and lattices.

4.2.2 Window method

The other method we use to solve the GEVP is the window-method, with a fixed window width of $t_w = t - t_0 = 3$. While the window-method ensures that $t < 2t_0$ for all values of t in the region where we would like to extract the energy levels, one particular downside of the window method is that $C(t_0) = C(t - t_w)$ on the right-hand side of the GEVP equation will suffer from noise already for relatively early timeslices, unlike in the fixed- t_0 method. On the other hand, the plateau in the effective masses is realised comparably quickly. Both t_{\min}

d^2	irrep	E5	χ^2/dof	F6	χ^2/dof	F7	χ^2/dof
0	T_1	0.3226(12)	0.68	0.2878(12)	0.80	0.2722(16)	0.93
		0.4906(26)	0.86	0.3447(15)	0.90	0.3315(20)	1.31
				0.4333(39)	0.73	0.4277(42)	0.75
1	A_1	0.3016(10)	2.17	0.2319(7)	1.24	0.2048(9)	1.49
		0.3579(13)	0.90	0.2947(37)	0.47	0.2852(34)	0.59
				0.3597(26)	0.90	0.3498(22)	0.94
1	E_2	0.3210(20)	1.50	0.2899(12)	0.93	0.2743(21)	1.19
		0.5246(43)	0.45	0.3641(30)	0.89	0.3565(24)	0.52
				0.4435(56)	0.54	0.4361(66)	0.69
2	A_1	0.3069(16)	1.00	0.2467(9)	0.87	0.2209(11)	1.48
		0.3786(23)	1.39	0.3029(35)	0.83	0.2895(56)	0.96
				0.3755(23)	0.82	0.3664(29)	0.68
2	B_1	0.3156(35)	0.86	0.2658(10)	0.96	0.2469(15)	2.52
		0.4131(21)	1.05	0.3101(20)	1.07	0.2916(50)	1.71
				0.3814(39)	1.60	0.3694(42)	0.85
2	B_2	0.3258(29)	1.21	0.2902(20)	0.86	0.2762(31)	1.86
		0.5374(93)	0.87	0.3775(23)	1.51	0.3673(27)	1.19
				0.3924(57)	1.24	0.3762(61)	0.66
3	A_1	0.3104(28)	0.56	0.2594(12)	0.49	0.2312(30)	2.10
		0.3952(46)	0.78	0.3016(17)	0.94	0.2819(40)	1.15
				0.3142(29)	1.07	0.3044(36)	0.95
3	E_1	0.3243(39)	1.85	0.2786(26)	1.17	0.2636(21)	0.96
		0.4531(40)	0.89	0.3277(28)	1.24	0.3075(56)	1.30

Table 4.2: Extracted energy levels aE_k (states are ordered from ground state to the higher excited states from top to bottom) in the fixed- t_0 method in each irrep for the three lattices used in this work. One level less per irrep is extracted on E5, due to the levels being above the $4m_\pi$ threshold and the interpolator basis being smaller by 1. All levels are extracted using the fixed- t_0 method with $t_0=3$, as described in Section 4.2.1

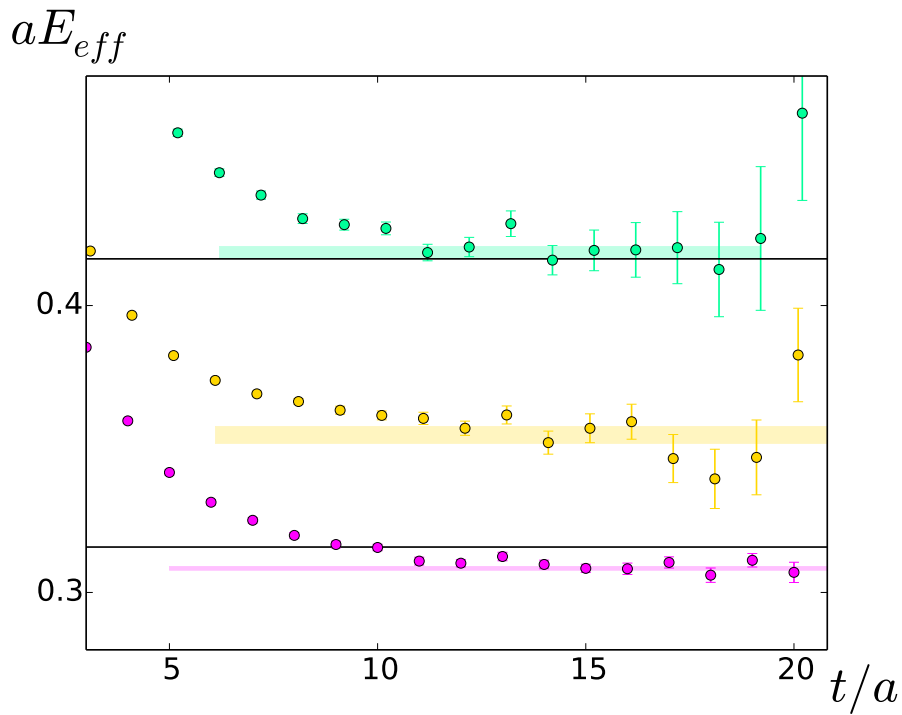
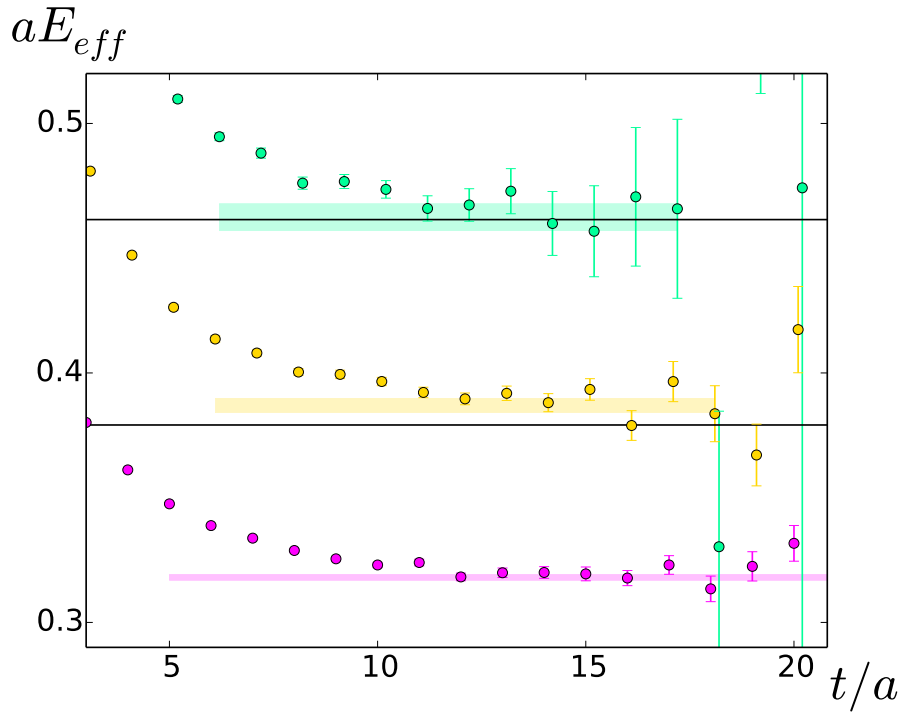


Figure 4.10: Spectrum from the GEVP on the F6 lattice, using the fixed- t_0 method, for two irreps: $\mathbf{d}^2 = 1, E_2$ on the top and $\mathbf{d}^2 = 2, A_1$ on the bottom. The different levels in the respective irrep are plotted using different colours and the accordingly coloured bands are the fit results of the corresponding eigenvalues to a two-exponential fit function. The width of those bands indicates the statistical error of the fit and the length shows the chosen fit range. The blue data points are from a higher energy level which we are not using in our analysis. The corresponding plots of energy levels in all other irreps can be seen in Appendix A.2.

and in particular t_{\max} are therefore taken at a lower value than in the other method. As in the fixed- t_0 method, we obtain N eigenvalues from the GEVP of the $N \times N$ correlator matrix in each irrep and we want to extract the energy E_k from the k^{th} eigenvector $\lambda^{(k)}(t)$. We also do this by fitting these eigenvalues to a two-exponential fit. It is worth noting again that the leading exponential in the window-method (i.e. the one decaying with the energy E_k according to $e^{-E_k t_w}$) is actually a constant. This is why we have two different definitions for the effective mass in the window method, Equations (2.12) and (2.15). The excited-state contributions seem to be of a similar size in both definitions – this can be seen in Figure 4.11, where the comparison of both definitions is made in the CMF on the F6 lattice. The variation of t_{\min} is shown for some exemplary energy levels in Figure 4.12. The same plot for all energy levels we used in the different frames and irreps is shown in the appendix in Figures A.2, A.4 and A.6. It is obvious from these plots that the fits in the window method are not as stable as the ones in the fixed- t_0 method. For higher values of t_{\min} , the fit result becomes lower and lower in particular in the excited states. Because t_{\max} is quite low also, for the reasons outlined at the beginning of this chapter, we cannot simply continue to higher values of t_{\min} because we would not fit to enough data points at that point. Finding a proper procedure how to choose all fit windows in a comparable way therefore turns out to be more complicated in the window method. The energy gap in the window method, described in Equation (2.10), is expected to be largest for the ground state and smaller for the excited states, which are closer to the energy E_{N+1} in the spectrum. We are therefore using $t_{\min} = 6$ for the ground states and $t_{\min} = 7$ for the excited states on all lattices.

Again, we are showing extracted energy levels together with the effective masses in Figure 4.13 for some irreps and in Appendix A.2 for all irreps and lattices.

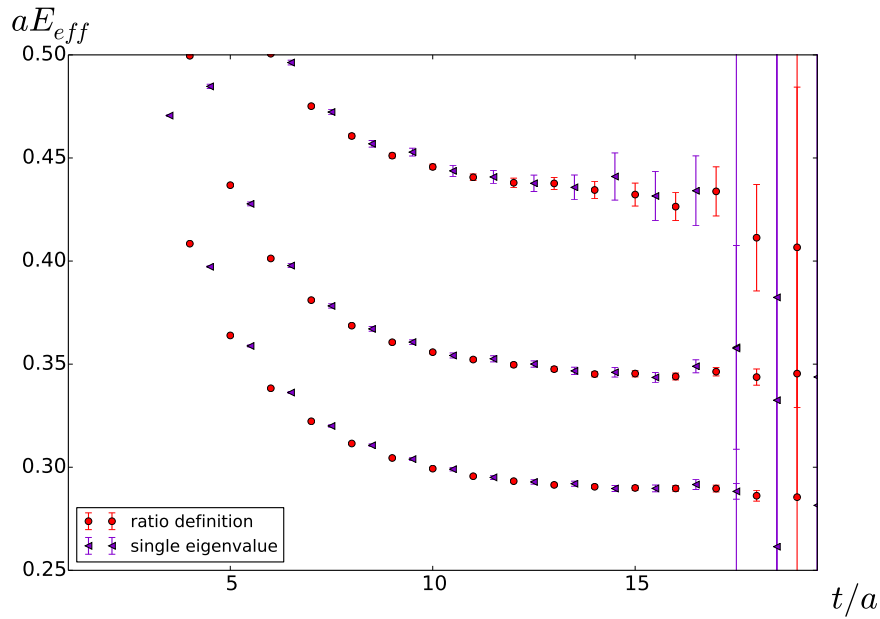


Figure 4.11: Comparison of the effective masses defined by Equation (2.12) (shown in purple and at full integer timeslices t) and (2.15) (shown in red and in between two timeslices $t + \frac{1}{2}$) in the CMF on the F6 lattice. Shown are the three lowest states in the system.

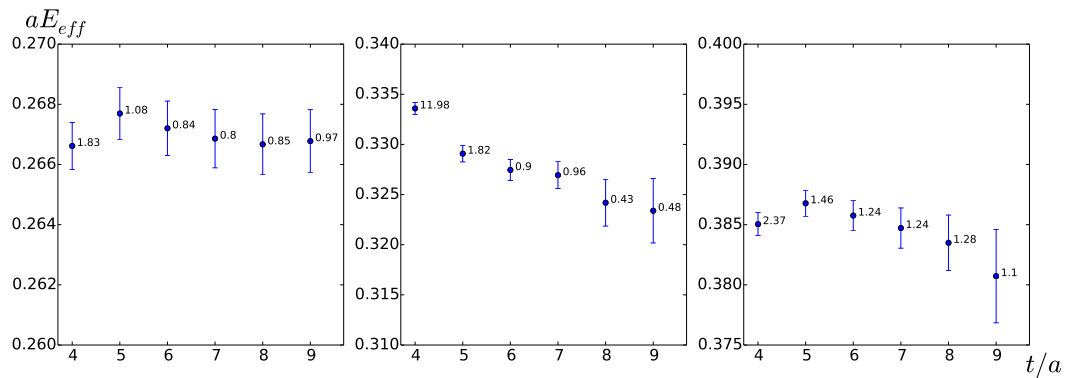


Figure 4.12: Same as Figure 4.9 but for the window method.

d^2	irrep	E5	χ^2/dof	F6	χ^2/dof	F7	χ^2/dof
0	T_1	0.3213(11)	0.77	0.2883(9)	0.63	0.2727(11)	0.45
		0.4905(21)	0.73	0.3443(15)	0.82	0.3306(17)	1.67
				0.4333(32)	0.42	0.4228(34)	0.75
1	A_1	0.3022(8)	1.05	0.2329(10)	0.84	0.2049(8)	1.40
		0.3573(12)	1.12	0.2996(15)	0.96	0.2875(18)	0.66
				0.3618(18)	1.24	0.3491(21)	1.04
1	E_2	0.3215(14)	1.67	0.2900(10)	0.83	0.2755(11)	1.14
		0.5238(41)	0.77	0.3671(18)	1.02	0.3559(18)	0.49
				0.4460(28)	0.35	0.4356(40)	0.56
2	A_1	0.3068(11)	0.85	0.2472(10)	1.18	0.2224(11)	0.95
		0.3783(20)	1.37	0.3054(17)	1.23	0.2945(21)	1.04
				0.3753(18)	0.61	0.3646(21)	1.77
2	B_1	0.3155(25)	0.60	0.2658(10)	0.86	0.2467(11)	1.82
		0.4128(20)	1.11	0.3106(18)	1.25	0.2948(29)	1.67
				0.3841(20)	1.48	0.3700(27)	0.43
2	B_2	0.3240(23)	1.10	0.2913(13)	0.84	0.2783(17)	2.22
		0.5454(51)	1.32	0.3755(18)	1.29	0.3653(20)	0.71
				0.3943(24)	1.06	0.3797(40)	0.78
3	A_1	0.3096(18)	0.59	0.2584(13)	0.37	0.2364(17)	1.35
		0.3937(47)	0.62	0.2989(14)	0.44	0.2831(20)	0.82
				0.3161(21)	0.97	0.3079(26)	0.82
3	E_1	0.3199(37)	1.83	0.2786(12)	1.41	0.2617(15)	0.73
		0.4538(37)	0.77	0.3295(18)	1.12	0.3132(34)	1.74

Table 4.3: Same as Table 4.2 but for the window method.

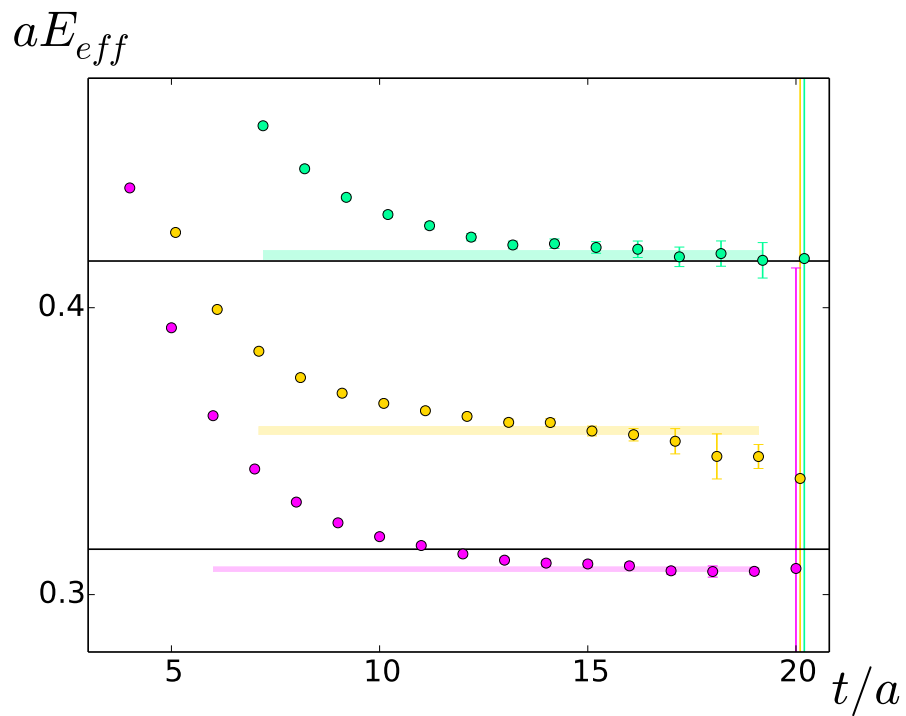
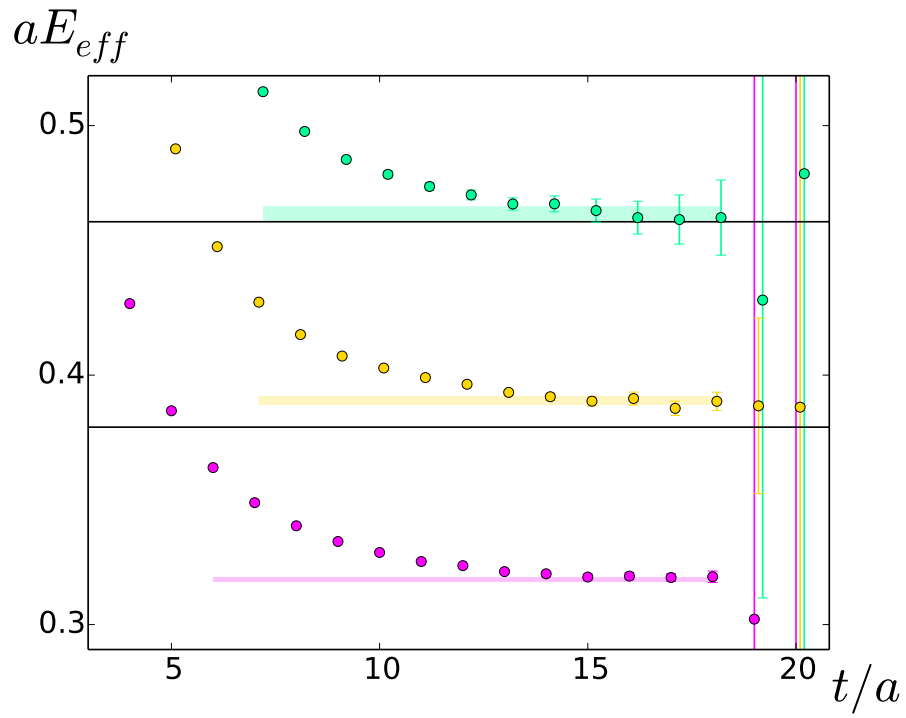


Figure 4.13: Same as Figure 4.10 but for the window method.

4.3 Phase-shift analysis

Having extracted the energy levels in all frames and irreps we consider, we can feed them into the Lüscher condition (Equation (3.55)) to obtain information about the phase shift $\delta(k)$. The only other ingredient needed are the modified zeta functions, which we numerically compute using the form explained in [87, 90].

The concept is shown in Figure 4.14, where the vertical axis in the left panel is the same one as the horizontal axis in the right panel, i.e. the extracted energy levels from the GEVP appear as an input value in the phase shift curve. One can see how the ground state of the CMF lies close to (but not exactly in) the resonance, because its phase shift value is close to $\pi/2$. Figure 4.15 shows the

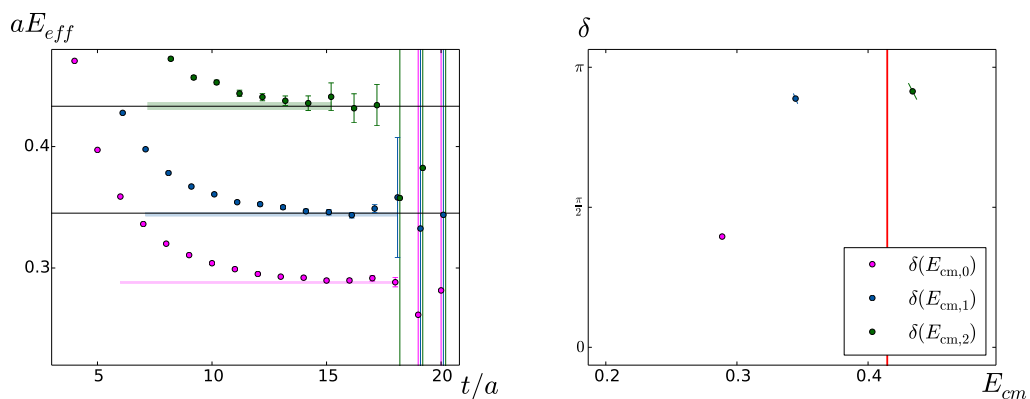


Figure 4.14: **Left panel:** Same as Figure 4.13 but shown are the energy levels in the CMF. **Right panel:** Phase shift δ as a function of the centre-of-mass energy E_{cm} . The three data points are calculated from the Lüscher condition from the fits to the eigenvalues, shown along with the effective masses in the left panel. The colour of each data points is the same as the one of the corresponding level on the left-hand side. The red vertical line indicates the $4\text{-}m_\pi$ threshold, above which the Lüscher condition does not apply any more. The error bars follow the values allowed by the Lüscher condition, because δ and E_{cm} are fully correlated at fixed pion mass m_π .

phase shift with the extracted energy levels from all irreps. One can clearly see that a phase shift from 0 to π occurs. Still, we have only discrete data points and would like a parametrisation of this phase shift δ which lets us extract the resonance information, i.e. the rho mass m_ρ and the coupling $g_{\rho\pi\pi}$ or equivalently the width $\Gamma_{\rho\pi\pi}$. The simplest such parametrisation is a Breit-Wigner curve,

$$\cot \delta_1(k, g_{\rho\pi\pi}, m_\rho) = \frac{6\pi}{g_{\rho\pi\pi}^2} \frac{(m_\rho^2 - E_{cm}^2)E_{cm}}{k^3}, \quad (4.4)$$

which is motivated in the resonance region through the effective-range formula. Given that the data points and their error estimates are confined to the lines dictated by the Lüscher zeta function, as is visible in Figure 4.15, we should not naively fit to the data points, taking only their uncertainty of the vertical

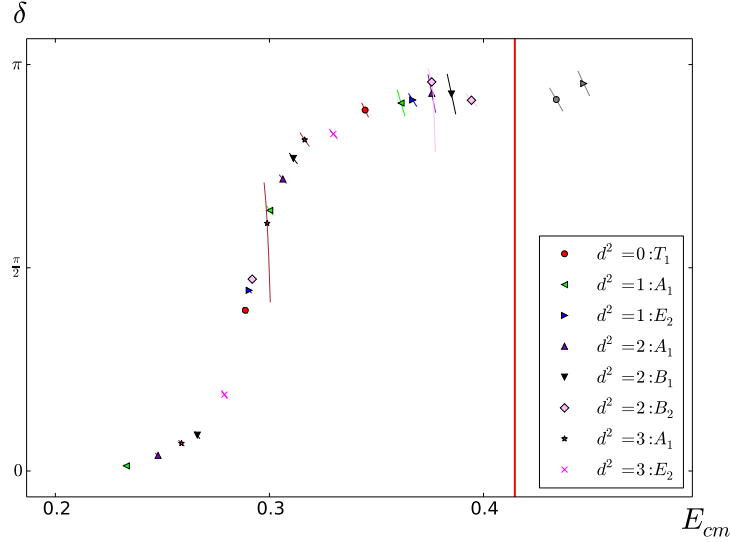


Figure 4.15: Same as the right panel of Figure 4.14 but with all irreps included on the F6 lattice. Differently coloured data points correspond to different irreps - the data points shown in Figure 4.14 now appear all in red. All points together clearly show the phase-shift behaviour which is indicative of a resonance.

or horizontal axis into account. In our approach, which fits the data according to their error behaviour along the curves dictated by the zeta-functions, we reformulate the Lüscher condition to

$$\cot \delta_1(k) \Big|_{\text{Lüscher}} = \cot(n\pi - \phi(q)) \quad (4.5)$$

and define the difference to Equation (4.4)

$$f(k; g_{\rho\pi\pi}, m_\rho) = \cot \delta_1(k) \Big|_{\text{Lüscher}} - \cot \delta_1(k; g_{\rho\pi\pi}, m_\rho). \quad (4.6)$$

Given any pair of resonance parameters $(g_{\rho\pi\pi}, m_\rho)$ we can solve $f(k; g_{\rho\pi\pi}, m_\rho) = 0$ and this way obtain $k_i^{\text{fit}}(g_{\rho\pi\pi}, m_\rho)$ and the energy levels $E_{\text{cm},i}^{\text{fit}}(g_{\rho\pi\pi}, m_\rho)$. We can then define the χ^2 -function

$$\chi^2(g_{\rho\pi\pi}, m_\rho) = \quad (4.7)$$

$$\sum_{i,j} (E_{\text{cm},i}^{\text{fit}}(g_{\rho\pi\pi}, m_\rho) - E_{\text{lat},i}) C_{i,j}^{-1} (E_{\text{cm},j}^{\text{fit}}(g_{\rho\pi\pi}, m_\rho) - E_{\text{lat},j}), \quad (4.8)$$

with the covariance matrix

$$C_{i,j} = \sum_{i,j} \sum_{k=0}^{n_{jk}} (E_{\text{lat},i,k} - \bar{E}_{\text{lat},i}) (E_{\text{lat},j,k} - \bar{E}_{\text{lat},j}), \quad (4.9)$$

calculated from the n_{jk} jackknife samples of the lattice energies and the lattice energy of the central value $\bar{E}_{\text{lat},i}$. By minimising this χ^2 -function on each

jackknife sample, we can obtain fit values for the resonance parameters.

One advantage of this way to fit the data points is that the fit routine uses the fit function as an input and consequently, it can be replaced by any fit function which is expected to describe the data. We have done this with a Gounaris-Sakurai [91] representation of $\delta(k)$,

$$\frac{k^3}{\omega} \cot[\delta_{11}(k)] = k^2 h(\omega) - k_\rho^2 h(m_\rho) + b(k^2 - k_\rho^2), \quad (4.10)$$

$$b = -\frac{2}{m_\rho} \left[\frac{2k_\rho^3}{m_\rho \Gamma_\rho} + \frac{1}{2} m_\rho h(m_\rho) + k_\rho^2 h'(m_\rho) \right], \quad (4.11)$$

$$h(\omega) = \frac{2k}{\pi\omega} \ln \frac{\omega + 2k}{2m_\pi}, \quad (4.12)$$

$$k_\rho = \sqrt{\frac{m_\rho^2}{4} - m_\pi^2}. \quad (4.13)$$

The results of these two different fits are compared in Table 4.4 and Table 4.5 and the corresponding phase-shift plots for all lattices are shown in Figure 4.16 and Figure 4.17. We also show the chiral behaviour of the resonance parameters in Figure 4.18. Both results agree perfectly within errors and also give a very similar uncertainty estimate. It is also obvious that the resonance mass m_ρ differs substantially from the naively extracted rho mass, using only the ground state of the GEVP. For the further discussion we will stick to the Breit-Wigner parametrisation.

	E5		F6		F7	
	BW	GS	BW	GS	BW	GS
m_ρ	0.3156(8)	0.3157(10)	0.2933(8)	0.2934(9)	0.2800(11)	0.2800(10)
$g_{\rho\pi\pi}$	5.70(9)	5.66(9)	6.08(13)	6.03(13)	5.90(21)	5.87(17)
χ^2/dof	1.47	1.64	0.75	0.84	1.57	1.63

Table 4.4: Resonance parameters extracted from the fit to the energy levels using the Lüscher formalism. All levels are extracted using the window method with $t_w=3$, as described in Section 4.2.2. Compared are the fit results to the Breit-Wigner parametrisation and the Gounaris-Sakurai parametrisation.

	E5		F6		F7	
	BW	GS	BW	GS	BW	GS
m_ρ	0.3168(9)	0.3171(9)	0.2923(12)	0.2923(11)	0.2784(17)	0.2785(19)
$g_{\rho\pi\pi}$	5.86(11)	5.83(9)	5.95(16)	5.92(15)	5.71(20)	5.69(35)
χ^2/dof	1.28	1.45	1.27	1.37	1.64	1.68

Table 4.5: Same as Table 4.4 but for the fixed- t_0 method.

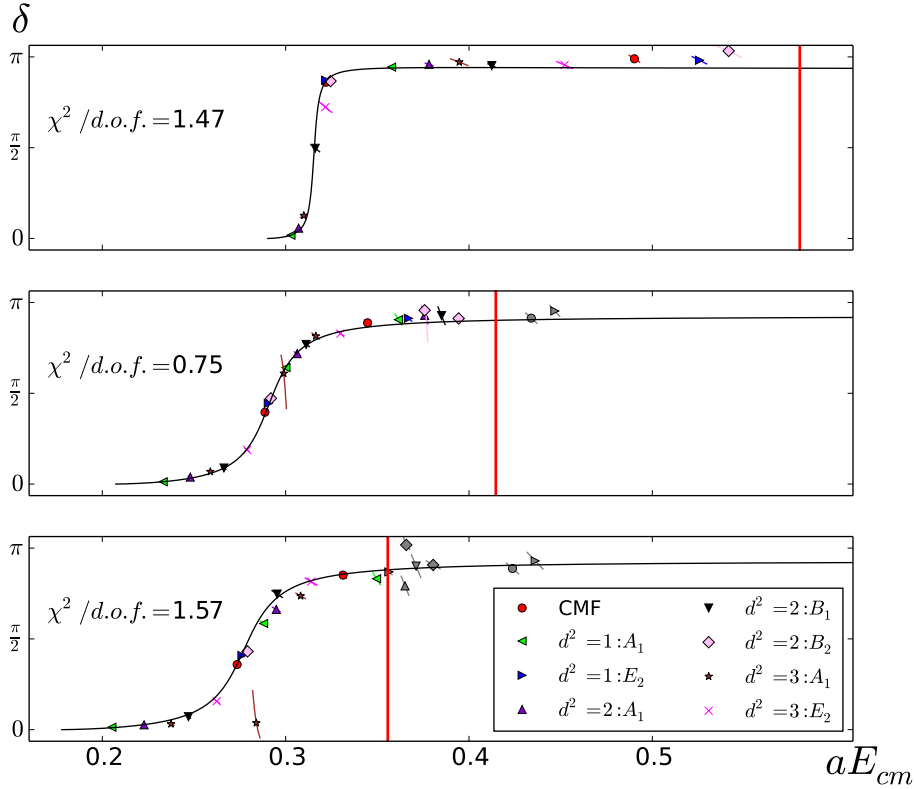


Figure 4.16: Comparison of the phase shifts on all three lattices in the window method. The horizontal axis shows the CMF energy of each level and data points of the same colour and symbol belong to the same frame and irrep. Error bars follow the lines allowed by the Lüscher zeta functions. The red vertical line indicates the $4m_\pi$ threshold in each system and data points above are excluded from the fit and thus shown in grey. The black line is the result of the Breit-Wigner fit to our data by minimising the χ^2 function defined in (4.8). The χ^2/dof for each lattice is also shown in the plots.

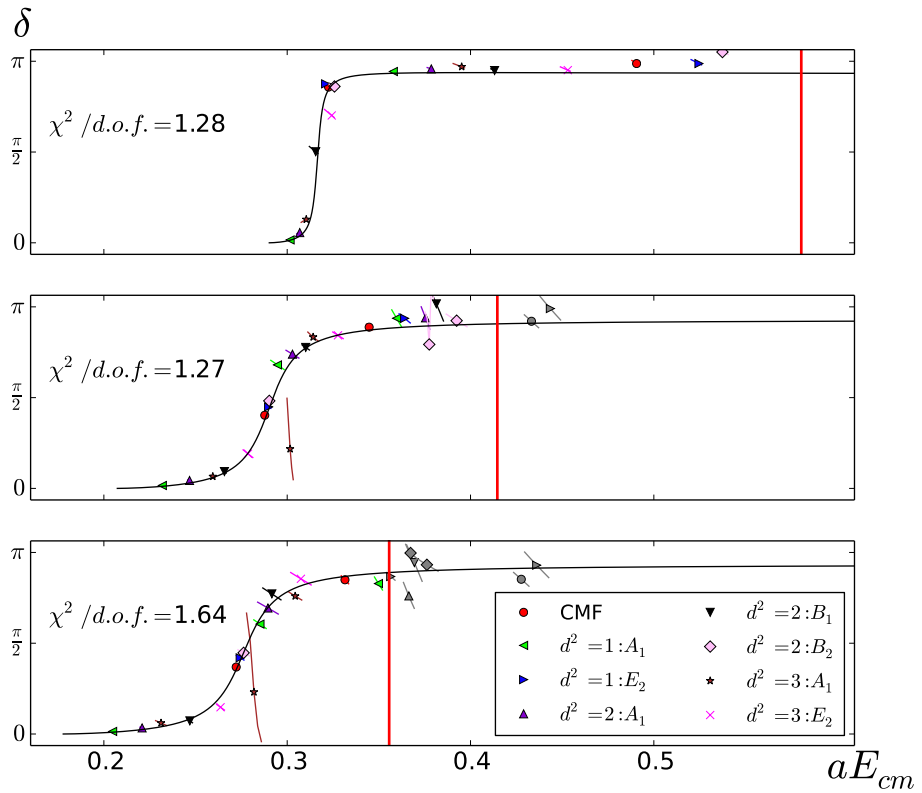


Figure 4.17: Same plot as Figure 4.16 but for the fixed- t_0 method.

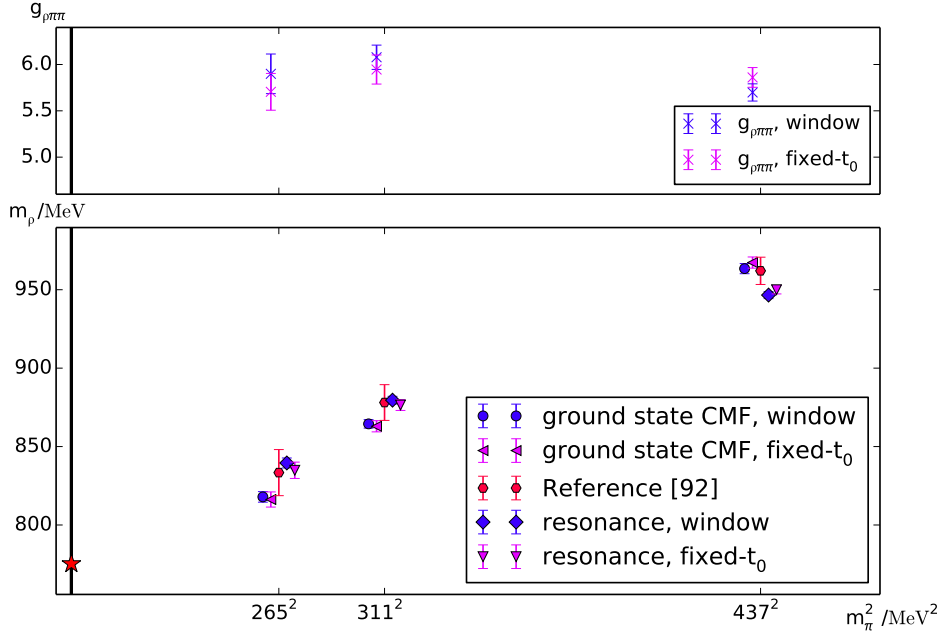


Figure 4.18: Comparison of the resonance parameters on all three lattices. The upper plot shows the coupling $g_{\rho\pi\pi}$, which shows a flat chiral behaviour and is consistent with $g_{\rho\pi\pi} \approx 6$ on all our lattices. The lower plot shows the rho mass as a function of m_π^2 . The red values are the naive rho mass, extracted from a $\langle \rho(t)\rho^\dagger(0) \rangle$ correlator in [92]. To the left of these points, we show our naive rho mass, which was extracted using the ground state of the GEVP. To the right are our resonance masses m_ρ extracted from the fit to the phase-shift points. All results from the window method are plotted in blue and the ones from the fixed- t_0 method are plotted in purple. The black vertical line indicates the physical pion mass and the red star shows the physical rho mass.

4.4 Matrix elements $|A_\Psi|$

In addition to the correlator matrix $C(t)$ we have calculated the matrix elements $\langle J_\mu(t)O_i^\dagger(0) \rangle$, both for the local (pointlike) current J_l and the conserved (point-split) current J_c and for the full operator basis O_i , consisting of ρ and $(\pi\pi)$ interpolators used in the system. Just like in the spectrum analysis, we are interested not only in the ground state of these correlation functions but also the excited-state spectrum. This is achieved using the eigenvectors $v_n(t)$ (normalised to $v_n(t)v_n^\dagger(t) = 1$) from the GEVP, which we obtained along with the corresponding eigenvalues $\lambda_n(t)$, but which were not needed for our spectrum analysis. These eigenvectors can be used to form optimised operators $X_n(t)$ which couple very well to the energy state E_n :

$$X_n(t) = v_n^\dagger O(t) = \sum_i v_{ni}^* O_i. \quad (4.14)$$

This operator can be used to form a two-point function,

$$D_{nn}(t) = \langle X_n(t)X_n^\dagger(0) \rangle = v_n^\dagger C(t)v_n, \quad (4.15)$$

which is the (approximate) projection of the correlation matrix $C_{ij}(t)$ onto the correlator corresponding to the n^{th} state. At large times, other states in $D_{nn}(t)$ are expected to be exponentially suppressed such that only the n^{th} state survives:

$$D_{nn}(t) \rightarrow |Z_n|^2 \exp(-E_n t). \quad (4.16)$$

$Z_n = \langle \Omega | X_n | n \rangle$ is an overlap factor with state n of the optimised interpolating operator X_n . From an exponential fit to $D_{nn}(t)$ we can extract $|Z_n|$ for our further analysis. We can also use the operators X_n to form a two-point function with the current insertions at the sink:

$$\langle J(t)X_n^\dagger(0) \rangle = \sum_i v_{ni} \langle J(t)O_i^\dagger(0) \rangle, \quad (4.17)$$

which again has a large-time behaviour dominated just by one state:

$$\langle J(t)X_n^\dagger(0) \rangle \rightarrow \langle \Omega | J(t) | n \rangle Z_n^* e^{-E_n t}. \quad (4.18)$$

We are interested in the matrix element $\langle \Omega | J(t) | n \rangle$, which can either be extracted by fitting an exponential function to $D_{nn}(t)$ and $\langle J(t)X_n^\dagger(0) \rangle$ or by forming various ratios [93]:

$$R_1(t) = \frac{\langle J(t)X_n^\dagger(0) \rangle}{\sqrt{D_{nn}(t)}e^{-\frac{1}{2}E_n t}} \rightarrow \frac{Z_n^*}{|Z_n|} \langle \Omega | J(t) | n \rangle, \quad (4.19)$$

$$R_2(t) = \frac{\langle J(t)X_n^\dagger(0) \rangle Z_n}{D_{nn}(t)} \rightarrow \langle \Omega | J(t) | n \rangle, \quad (4.20)$$

$$R_3(t) = \frac{\langle J(t)X_n^\dagger(0) \rangle}{Z_n e^{-E_n t}} \rightarrow \frac{Z_n^*}{Z_n} \langle \Omega | J(t) | n \rangle. \quad (4.21)$$

In our calculation, all those ratios agree within errors, but also show different excited-state effects. These ratios are plotted for all levels in Appendix B. $R_1(t)$ produces the most precise plateaus of the three and is not reliant on the fit to Equation (4.16) for the extraction of Z_n , such that we use $|R_1(E_n)| = |\langle \Omega | J(t) | n \rangle| \equiv |A_{\Psi,n}|^2$.

Our results for the matrix elements $|A_{\Psi}|$ are listed in Table 4.6 for the window method and in Table 4.7 for the fixed- t_0 method. There are quite large differences between $Z_V |A_{\Psi}|_l$ (using the local, pointlike current from Equation (3.6)) and $|A_{\Psi}|_c$ (using the conserved, point-split current from Equation (3.16)) due to cut-off effects. This is a clear indication that an improved version of the currents, introduced in Equation (3.18), would be preferable. In principle, these differences are supposed to vanish in the continuum limit, but we cannot check this as part of this work since we are only considering a single lattice spacing.

d^2	irrep	E5		F6		F7	
Z_V		0.74418(33)		0.74143(14)		0.74011(23)	
		$Z_V A_\Psi _l$	$ A_\Psi _c$	$Z_V A_\Psi _l$	$ A_\Psi _c$	$Z_V A_\Psi _l$	$ A_\Psi _c$
0	T_1	2.41(34)	2.12(31)	1.94(22)	1.74(19)	1.79(24)	1.63(22)
		0.75(20)	0.57(16)	1.06(18)	0.90(16)	1.05(17)	0.90(15)
				0.71(22)	0.53(18)	0.80(20)	0.65(18)
1	A_1	2.02(25)	1.81(22)	0.55(7)	0.51(6)	0.48(6)	0.46(5)
		1.85(25)	1.59(22)	2.18(30)	1.95(26)	2.08(30)	1.87(26)
				0.79(14)	0.66(12)	0.87(15)	0.74(13)
1	E_2	2.24(33)	1.98(30)	1.94(21)	1.74(19)	1.79(23)	1.63(21)
		1.18(35)	0.97(30)	0.89(16)	0.74(14)	0.98(16)	0.82(14)
				0.57(17)	0.42(14)	0.52(14)	0.40(11)
2	A_1	2.44(32)	2.17(28)	0.83(10)	0.77(9)	0.72(10)	0.68(9)
		1.57(26)	1.33(23)	2.25(32)	2.00(28)	2.22(33)	1.98(29)
				0.65(12)	0.54(10)	0.63(11)	0.53(10)
2	B_1	2.05(39)	1.81(35)	1.02(12)	0.93(11)	0.82(11)	0.76(11)
		0.98(17)	0.81(15)	1.77(25)	1.56(22)	1.76(30)	1.57(26)
				0.43(10)	0.33(9)	0.50(10)	0.41(9)
2	B_2	2.18(41)	1.92(37)	1.91(24)	1.71(21)	1.77(27)	1.60(24)
		0.61(19)	0.50(16)	0.38(8)	0.31(7)	0.16(4)	0.14(4)
				0.92(18)	0.74(15)	0.87(20)	0.69(16)
3	A_1	2.75(44)	2.44(40)	1.17(15)	1.08(13)	1.01(17)	0.94(16)
		1.41(31)	1.17(26)	1.27(18)	1.12(15)	0.98(14)	0.87(13)
				1.87(29)	1.63(26)	2.05(33)	1.81(29)
3	E_1	1.42(33)	1.25(30)	1.40(18)	1.26(15)	1.25(18)	1.14(17)
		0.78(17)	0.64(14)	1.40(22)	1.20(19)	1.40(25)	1.21(22)

Table 4.6: Matrix elements $|A_\Psi|$ extracted from the window method in units of 10^{-2} . The values for Z_V are taken from [92]. The difference in $Z_V|A_\Psi|_l$ and $|A_\Psi|_c$ is due to cut-off effects.

d^2	irrep	E5		F6		F7	
Z_V		0.74418(33)		0.74143(14)		0.74011(23)	
		$Z_V A_\Psi _l$	$ A_\Psi _c$	$Z_V A_\Psi _l$	$ A_\Psi _c$	$Z_V A_\Psi _l$	$ A_\Psi _c$
0	T_1	2.43(36)	2.14(32)	1.98(25)	1.78(22)	1.79(28)	1.62(26)
		0.79(22)	0.61(18)	0.97(15)	0.82(13)	1.03(17)	0.88(15)
				0.61(15)	0.46(12)	0.64(18)	0.48(15)
1	A_1	2.04(26)	1.83(24)	0.57(6)	0.53(5)	0.49(6)	0.47(6)
		1.78(25)	1.53(22)	2.14(45)	1.91(40)	2.08(40)	1.86(36)
				0.68(13)	0.56(11)	0.75(14)	0.63(12)
1	E_2	2.24(39)	1.98(34)	1.98(24)	1.77(22)	1.80(31)	1.63(28)
		0.92(27)	0.72(23)	0.78(15)	0.64(13)	0.84(15)	0.69(13)
				0.44(13)	0.30(9)	0.41(13)	0.29(10)
2	A_1	2.48(37)	2.20(33)	0.93(10)	0.85(9)	0.75(10)	0.70(10)
		1.42(25)	1.19(22)	2.18(43)	1.93(38)	2.14(51)	1.91(46)
				0.51(9)	0.41(8)	0.53(11)	0.44(9)
2	B_1	2.05(45)	1.82(40)	1.12(13)	1.02(12)	0.89(13)	0.82(12)
		0.98(17)	0.81(15)	1.69(25)	1.49(22)	1.66(37)	1.47(33)
				0.38(9)	0.30(8)	0.39(9)	0.31(8)
2	B_2	2.21(46)	1.95(41)	1.94(29)	1.73(25)	1.76(36)	1.59(32)
		0.35(13)	0.28(11)	0.29(6)	0.23(5)	0.24(5)	0.19(5)
				0.74(19)	0.57(15)	0.71(19)	0.56(15)
3	A_1	2.80(54)	2.49(48)	1.36(16)	1.23(14)	1.04(21)	0.97(19)
		1.18(26)	0.97(22)	1.53(20)	1.33(18)	1.23(25)	1.10(22)
				1.41(24)	1.21(21)	1.76(34)	1.54(30)
3	E_1	1.47(35)	1.30(32)	1.54(26)	1.38(22)	1.37(20)	1.24(18)
		0.69(15)	0.56(13)	1.26(22)	1.08(18)	1.23(29)	1.07(25)

Table 4.7: Same as Table 4.6 but for the fixed- t_0 method

Chapter 5

Applications

In general, the results of the spectrum analysis in the window and fixed- t_0 method have some systematic differences already on the level of the energy levels. These differences have an effect on all subsequent steps of our analysis, but as we have shown with the phase-shift analysis, the methods do not contradict each other and the results are not substantially different. For the next analysis steps, which are the extraction of the timelike pion form factor and the hadronic vacuum polarisation to the muon ($g - 2$), we will therefore only discuss a single method. We chose the window method due to its theoretically motivated advantages. We have performed the full analysis of the pion form factor and the hadronic vacuum polarisation as well in the fixed- t_0 method, analogously to how it is explained in the forthcoming chapters, and present those results in Appendix D.

5.1 Timelike pion form factor

Following an idea proposed by Meyer [3], the pion form factor F_π can be extracted using $\pi\pi$ -scattering information from Lattice QCD, in the timelike region. This is remarkable, because Lattice QCD only allows access to form factors in the spacelike region, $q^2 < 0$, due to the fact that it is formulated in Euclidean space. The formalism does not include an explicit analytic continuation, which one would expect for a quantity which could naively only be determined using correlation functions in Minkowski space. Previously [94–100], the pion form factor was calculated on the lattice in the spacelike region and then used to extract the pion charge radius $\langle r^2 \rangle$ at low momenta $q^2 \rightarrow 0$.

The idea is to closely follow the Lüscher approach [1, 2] and consider QCD coupled to $SU(2)$ gauge bosons whose mass is assumed to be in the regime $2m_\pi \leq E \leq 4m_\pi$, where $\pi\pi$ scattering takes place. These gauge bosons are taken as a perturbation due to their coupling to the quarks, which on the

lattice can be put directly into the Lüscher condition:

$$\left(\delta_1(k) + \frac{\partial\delta(k)}{\partial k}\Delta k + \Delta\delta_1(k)\right) + \left(\phi(q) + \phi'(q)\Delta q\right) = 0, \quad (5.1)$$

and consequently

$$\Delta\delta_1(k) = -\left(q\phi'(q) + k\frac{\partial\delta(k)}{\partial k}\right)\frac{\Delta k}{k}. \quad (5.2)$$

In here, the shift Δk is related to the mass M and coupling e of the gauge bosons as well as to the current matrix element $A_{\Psi,n} = L^{3/2}\langle n|j(x)|0\rangle$ via

$$\Delta k = \mp\frac{e}{\sqrt{2M}}A_{\Psi}\frac{E_{\pi\pi}}{k_{\pi}}. \quad (5.3)$$

In infinite volume however, this change in the phase shift can be derived from the change in the scattering amplitude, which is affected by the coupling of the gauge bosons to the quarks. This change is related to the square of the pion form factor in the timelike region, $|F_{\pi}|^2$ via

$$\Delta\delta_1(k) = \mp\frac{e^2}{24\pi\sqrt{M}\frac{e}{\sqrt{2}}|A_{\Psi}|}|F_{\pi}|^2\frac{k_{\pi}^3}{E_{\pi\pi}}. \quad (5.4)$$

By comparing these two expressions in the finite- and infinite volume case, the final formula for the pion form factor

$$|F_{\pi}(E)|^2 = \left(q\phi'(q) + k\frac{\partial\delta(k)}{\partial k}\right)\frac{3\pi E^2}{k^5}|A_{\Psi}|^2, \quad (5.5)$$

is derived. This formula is only valid in the CMF, but has been extended to moving frames [101], where the only differences are the different functions $\phi_{\Lambda}^{\mathbf{d}}(q)$ and a pre-factor

$$|(F_{\pi})_{\Lambda}^{\mathbf{d}}(E)|^2 = G_{\Lambda}^{\mathbf{d}}(\gamma)\left(q(\phi_{\Lambda}^{\mathbf{d}})'(q) + k\frac{\partial\delta(k)}{\partial k}\right)\frac{3\pi E^2}{k^5}|A_{\Psi}|^2, \quad (5.6)$$

where

$$G_{\Lambda}^{\mathbf{d}}(\gamma) = \begin{cases} \frac{1}{\gamma} & \text{if } \Lambda = A_1 \\ \gamma & \text{else} \end{cases}, \quad (5.7)$$

with γ as defined in Equation (3.42). The derivatives $(\phi_{\Lambda}^{\mathbf{d}})'(q)$ and $\frac{\partial\delta(k)}{\partial k}$ can be obtained numerically, but both functions are quite steep or have poles in some sections so that it is more reliable to evaluate the derivatives directly. The formulae needed for this are given in Appendix C.

As has been noted before, the matrix elements $|A_{\Psi}|$ from Chapter 4.4 suffer from discretisation effects which is manifested in the substantial difference be-

tween $Z_V|A_\Psi|_l$ (extracted from a local current J_l) and $|A_\Psi|_c$ (extracted from a conserved current J_c). For the pion form factor and the further discussion, we will use a local-conserved version, i.e. in Equation (5.6) use

$$|A_\Psi|_{lc}^2 \equiv Z_V|A_\Psi|_l|A_\Psi|_c. \quad (5.8)$$

The main reason for this is that we will compare our results in the next chapter to lattice data from a different project, which was obtained using a local-conserved current as well.

Using those matrix elements $|A_\Psi|_{lc}^2$ along with the energy levels of the GEVP and the phase shift data from our Lüscher analysis we can map out $F_\pi(s)$ using Equation (5.6). We are also comparing our form-factor results to the Gounaris-Sakurai parametrisation [91] of F_π , which we want to stress is not a fit to the data and which can be parametrised only by the resonance parameters m_ρ, Γ_ρ via [102]

$$F_\pi(\omega) = \frac{f_0}{\frac{k^3}{\omega}(\cot[\delta_{11}(k)] - i)}, \quad (5.9)$$

$$f_0 = -\frac{m_\pi^2}{\pi} - k_\rho^2 h(m_\rho) - b \frac{m_\rho^2}{4}, \quad (5.10)$$

where the definitions of Equation (4.10) are used. The results of our lattice-calculated values for F_π and the Gounaris-Sakurai curves are shown in Figure 5.1. The explicit values for the F_π data points along with the extracted matrix elements $|A_\Psi|$ are also listed in Table 5.1. The error of the data points is not fully Gaussian, because the term with the derivative $(\phi_\Lambda^{\mathbf{d}})'(q)$ follows strict lines similar to the ones shown in the phase shift plot in Figure 4.16. But because other terms contribute as well to the error of F_π , there is no clear correlation like in the case of the phase shift, which renders it difficult to plot the error estimate precisely.

The Gounaris-Sakurai curve seems to represent our data reasonably well, but it would be desirable to have a fit to our form factor data extracted from Lattice QCD. One way to fit is using an n -subtracted Omnès representation [103, 104]

¹

$$F(t) = \exp \left(P_{n-1}(t)t + \frac{t^n}{\pi} \int_{4m_\pi^2}^{\infty} ds \frac{\delta_{11}(s)}{s^n(s-t-i\epsilon)} \right), \quad (5.11)$$

where $P_{n-1}(t)$ is a polynomial function of grade $n-1$. For the 2-subtracted

¹I would like to thank Harvey Meyer for pointing out the possibility to fit F_π in this way and Ben Hörz for discussions and ideas about the actual implementation of the fit routine.

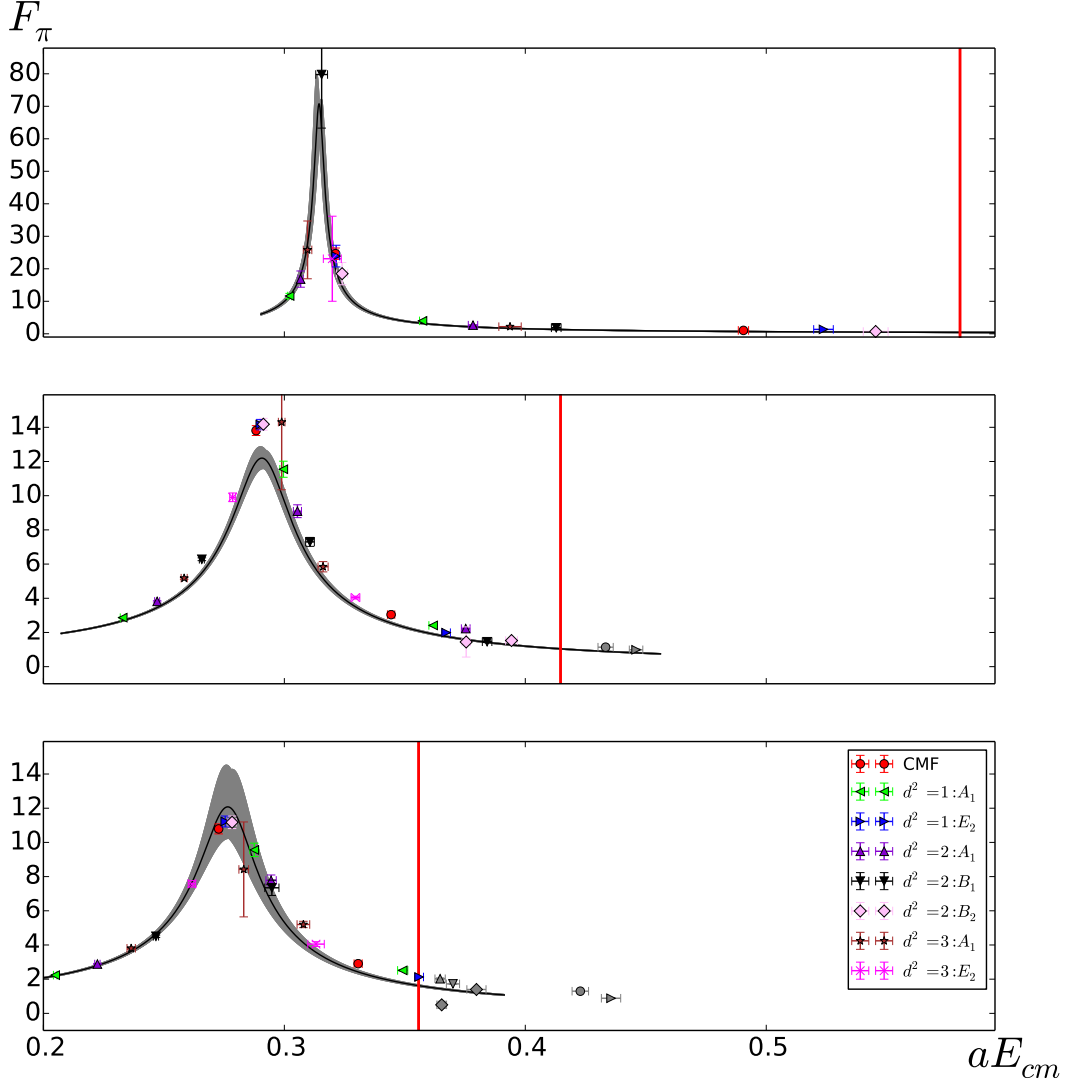


Figure 5.1: The timelike pion form factor on the E5, F6, F7 lattice (top to bottom). Data points with the same symbol and colour belong to the same frame and irreps. The error bars associated with each data point come from a jackknife estimate. The grey curve is the GS representation of F_π , which only takes the fit parameters of the phase-shift fit $m_\rho, g_{\rho\pi\pi}$ into account – it is not a fit to the data pictured in these plots. The vertical red bars indicate the $4m_\pi$ threshold in each lattice.

d^2	irrep	E5			F6			F7		
		$ A_\Psi $	F_π	$ A_\Psi $	F_π	$ A_\Psi $	F_π	$ A_\Psi $	F_π	
0	T_1	0.0212(31) 0.0057(16)	23.15(1.63) 0.91(4)	0.0174(19) 0.0090(16) 0.0053(18)	13.09(27) 2.81(4) 0.99(6)	0.0163(22) 0.0090(15) 0.0065(18)	10.28(28) 2.70(3) 1.17(4)			
1	A_1	0.0181(22) 0.0159(22)	11.01(76) 3.68(3)	0.0051(6) 0.0195(26) 0.0066(12)	2.77(3) 10.90(45) 2.21(4)	0.0046(5) 0.0187(26) 0.0074(13)	2.18(3) 9.05(37) 2.31(4)			
1	E_2	0.0198(30) 0.0097(30)	22.46(3.14) 1.23(6)	0.0174(19) 0.0074(14) 0.0042(14)	13.41(29) 1.81(3) 0.85(5)	0.0163(21) 0.0082(14) 0.0040(11)	10.70(30) 1.95(3) 0.78(3)			
2	A_1	0.0217(28) 0.0133(23)	15.87(2.36) 2.44(3)	0.0077(9) 0.0200(28) 0.0054(10)	3.67(4) 8.56(35) 2.03(4)	0.0068(9) 0.0198(29) 0.0053(10)	2.80(3) 7.35(30) 1.85(5)			
2	B_1	0.0181(35) 0.0081(15)	75.08(15.54) 1.67(3)	0.0093(11) 0.0156(22) 0.0033(9)	5.99(8) 6.84(25) 1.28(5)	0.0076(11) 0.0157(26) 0.0041(9)	4.34(7) 6.93(43) 1.57(3)			
2	B_2	0.0192(37) 0.0050(16)	17.38(3.22) 0.63(13)	0.0171(21) 0.0031(7) 0.0074(15)	13.43(33) 1.31(80) 1.38(3)	0.0160(24) 0.0014(4) 0.0069(16)	10.64(35) 0.48(20) 1.25(3)			
3	A_1	0.0244(40) 0.0117(26)	24.33(8.38) 2.00(3)	0.0108(13) 0.0112(15) 0.0163(26)	4.96(6) 13.47(3.73) 5.46(28)	0.0094(16) 0.0087(13) 0.0181(29)	3.68(6) 7.96(2.63) 4.88(18)			
3	E_1	0.0125(30) 0.0064(14)	21.70(12.31) 1.06(2)	0.0126(15) 0.0120(19)	9.41(24) 3.75(8)	0.0114(17) 0.0121(22)	7.24(18) 3.78(13)			

Table 5.1: Numerical values and jackknife error estimate for each data point of F_π . In each frame and irrep, we also show the value for $|A_\Psi|_{lc}$, computed using Equation (5.8), which was used to compute F_π . Plots of this data with different parametrisations are shown in Figures 5.1, 5.2 and 5.3.

version, the polynomial is a constant,

$$P(t) = \frac{\langle r^2 \rangle}{6}, \quad (5.12)$$

with the square radius $\langle r^2 \rangle$ of the pion. The polynomial for the 3-subtracted version reads

$$P(t) = \frac{\langle r^2 \rangle}{6} + \frac{1}{2} \left(2c_V^\pi - \left(\frac{\langle r^2 \rangle}{6} \right)^2 \right) t, \quad (5.13)$$

with the curvature c_V^π of the pion form factor. The integrand has a pole at $s = t$ and in order to solve the integral numerically we need to do a subtraction,

$$\int_{4m_\pi^2}^{\infty} ds \frac{\delta_{11}(s)}{s^n(s-t-i\epsilon)} = \int_{4m_\pi^2}^{\infty} ds \frac{\delta_{11}(s) - \delta_{11}(t)}{s^n(s-t)} + \delta_{11}(t) \int_{4m_\pi^2}^{\infty} ds \frac{1}{s^n(s-t-i\epsilon)}. \quad (5.14)$$

The second integral can now be computed analytically for the 2-subtracted version,

$$\int_{4m_\pi^2}^{\infty} ds \frac{1}{s^2(s-t-i\epsilon)} = -\frac{1}{4m_\pi^2 t^2} \left(t - 8m_\pi^2 \ln(2) + 4m_\pi^2 \ln \left(\frac{t}{m_\pi^2} - 4 \right) \right) + \frac{i\pi}{t^2}, \quad (5.15)$$

or for the 3-subtracted version,

$$\begin{aligned} \int_{4m_\pi^2}^{\infty} ds \frac{1}{s^3(s-t-i\epsilon)} = \\ -\frac{1}{32m_\pi^4 t^3} \left(t^2 + 8m_\pi^2 t - 64m_\pi^4 \ln(2) + 32m_\pi^4 \ln \left(\frac{t}{m_\pi^2} - 4 \right) \right) + \frac{i\pi}{t^3}. \end{aligned} \quad (5.16)$$

The form factor in the 2-subtracted version can then be expressed via

$$\begin{aligned} F(t) = \exp \left(Pt + \frac{t^2}{\pi} \int_{4m_\pi^2}^{\infty} ds \frac{\delta_{11}(s) - \delta_{11}(t)}{s^2(s-t)} \right. \\ \left. - \frac{\delta_{11}(t)}{4m_\pi^2 \pi} \left(t - 8m_\pi^2 \ln(2) + 4m_\pi^2 \ln \left(\frac{t}{m_\pi^2} - 4 \right) \right) + i\delta_{11}(t) \right). \end{aligned} \quad (5.17)$$

We are then computing the Omnès function

$$O(t) = \exp \left(\frac{t^2}{\pi} \int_{4m_\pi^2}^{\infty} ds \frac{\delta_{11}(s) - \delta_{11}(t)}{s^2(s-t)} \right)$$

$$- \frac{\delta_{11}(t)}{4m_\pi^2\pi} \left(t - 8m_\pi^2 \ln(2) + 4m_\pi^2 \ln \left(\frac{t}{m_\pi^2} - 4 \right) \right) + i\delta_{11}(t), \quad (5.18)$$

for each energy levels extracted and fit the ratio $\frac{F(t)}{O(t)}$ to the function $\exp(Pt)$, where we allow the polynomial to have a constant and a linear term. Both the pion form factor in Equation (5.17) as well as the Omnès function in Equation (5.18) have a similar expression in the 3-subtracted version, which straightforwardly follows from Equation (5.16). The results of the fit to the 2-subtracted version are shown in Figure 5.2 and the same plot for the 3-subtracted version can be seen in Figure 5.3. Both fits seem to describe the F_π data much better than the GS representation of the form factor. All fits have quite large values for χ^2/dof , but the ones in the 3-subtracted version are significantly smaller. We have also computed the square radius $\langle r^2 \rangle$ from this fit and show our results in Table 5.2. The results for the 2- and 3-subtracted version differ on the level of 2σ , which might be an indication that the 2-subtracted version is not enough to describe the data accurately. The square radius was also computed in [100] via a chiral extrapolation of the spacelike pion form factor, computed on the same ensembles we are using in our study. Because they were using a local current (as opposed to the local-conserved current we were using up to this point), we did the whole analysis as well with $|A_\Psi| = |A_\psi|_l$ in Equation (5.6). The results for the square radius from this analysis are shown and compared to the result from [100] in Table 5.3. The comparison of this table with Table 5.2 shows again that discretisation effects in our currents are large. This effect is already visible in the matrix elements $|A_\Psi|$, shown in Table 4.6.

	n	E5	F6	F7
$\langle r^2 \rangle / r_0^2$	2	1.15(2)	1.31(1)	1.42(2)
$\langle r^2 \rangle / r_0^2$	3	1.08(3)	1.28(3)	1.34(4)
c_V / r_0^4	3	3.43(7)	4.75(7)	5.78(15)

Table 5.2: Square radius and curvature (in units of 10^{-2}) of the pion obtained from the fit to the n -subtracted Omnès representation of the form factor, using a local-conserved vector current. The Sommer scale r_0 is taken from [53].

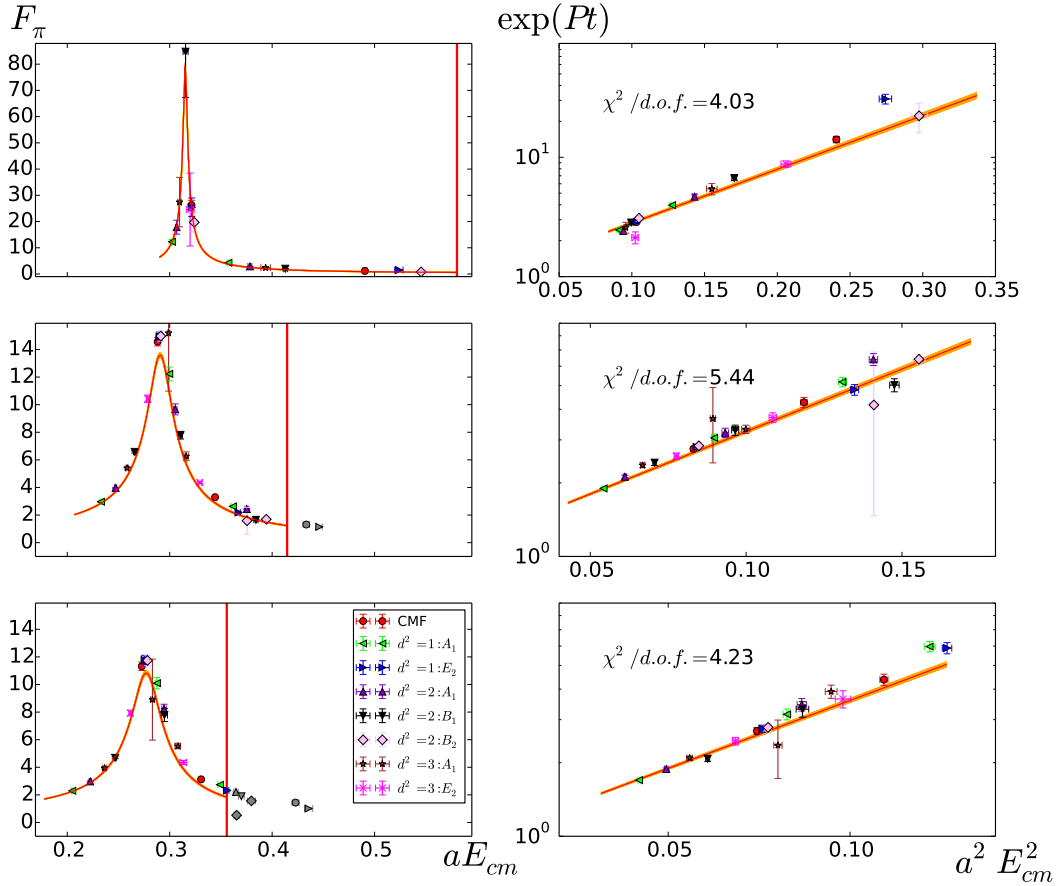


Figure 5.2: **Left panel:** The timelike pion form factor on the E5, F6, F7 lattice (top to bottom), window method. Data points with the same symbol and colour belong to the same frame and irreps. The orange curve is the fit to F_π , parametrised via the 2-subtracted version of Equation (5.17). The vertical red bars indicate the $4m_\pi$ threshold in each lattice and data points above this threshold have not been included in the fit and are shown in grey for this reason. **Right panel:** The data which we are actually fitting to. The y-axis shows F_π divided by the Omnès integral, Equation (5.18), and the fit function is $f(t) = \exp(Pt)$, where P is a constant. The horizontal axis is displayed on a log scale and the orange curve is the fit function with the jackknife error. Shown are also the $\chi^2/\text{d.o.f.}$ values of the respective fits, which are quite high.

	n	E5	F6	F7
$\langle r^2 \rangle / r_0^2$	2	1.22(2)	1.38(1)	1.49(2)
$\langle r^2 \rangle / r_0^2$	3	1.16(3)	1.34(3)	1.38(3)
c_V / r_0^4	3	3.64(8)	5.02(7)	3.26(7)
$\langle r^2 \rangle / r_0^2$		1.18(5)	1.37(6)	1.61(10)

Table 5.3: Same as Table 5.2 but using a local-local vector current. The last line shows the values from [100], where $\langle r^2 \rangle$ has been computed using a chiral extrapolation of the spacelike form factor. The difference of our results to the corresponding values in Table 5.2 comes from discretisation effects, which are also visible in the matrix elements themselves, shown in Table 4.6.

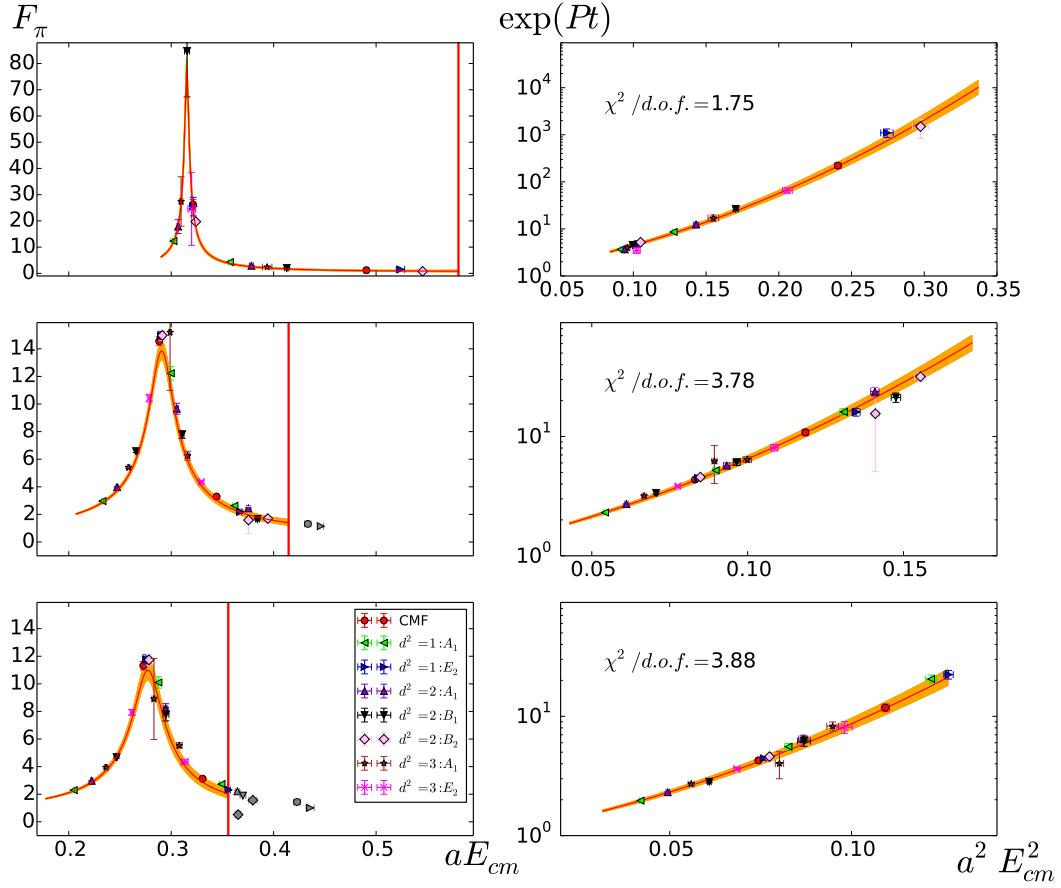


Figure 5.3: Same as Figure 5.2, but using the 3-subtracted version of Equation (5.17). The fit function is now $f(t) = \exp(Pt)$, where P is a first grade polynomial.

5.2 Hadronic vacuum polarisation

The magnetic moment of the muon [4],

$$\mathbf{M}_\mu = g_\mu \frac{e}{2m_\mu} \mathbf{S}, \quad (5.19)$$

is defined by the spin-angular momentum \mathbf{S} of the muon, and the gyromagnetic ratio g_μ , famously predicted by the Dirac-equation at tree-level to be $g_\mu^{(0)} = 2$ [105, 106]. Because of quantum loop effects the value of g_μ is actually a bit larger than 2, leading to the definition of the anomalous magnetic moment of the muon,

$$a_\mu = \frac{g_\mu - 2}{2}. \quad (5.20)$$

In the Standard model, this quantity has three contributions

$$a_\mu = a_\mu^{\text{W}} + a_\mu^{\text{QED}} + a_\mu^{\text{QCD}}$$

where the weak contribution [107]

$$a_\mu^{\text{W}} = 153.6(1.0) \times 10^{-11}$$

is known up to 2-loop corrections and the QED contribution [108]

$$a_\mu^{\text{QED}} = 116584718.951(0.80) \times 10^{-11}$$

is known up to 5-loop corrections. In comparison to the errors on those two contributions, the one in the a_μ^{QCD} part is much larger. The leading-order QCD contribution is given by the hadronic vacuum polarisation (Figure 5.4), whose value has been determined in Reference [109] as

$$a_\mu^{\text{QCD},[\text{LO}]} = 6931(34) \times 10^{-11}.$$

Incidentally, the leading-order HVP contribution dominates the total uncertainty in the Standard-Model estimate of the muon $g - 2$. The HVP is the lowest order in which hadronic effects have a contribution to $(g - 2)_\mu$, because they couple only indirectly to the muons via photons. The next-to-leading order contribution can be split up into a contribution from higher hadronic loops [110],

$$a_\mu^{\text{QCD},[\text{NLO}],[\text{loops}]} = -97.9(0.9) \times 10^{-11},$$

and the hadronic light-by-light scattering contribution [111]

$$a_\mu^{\text{QCD},[\text{NLO}],[\text{Hlbl}]} = 105(26) \times 10^{-11},$$

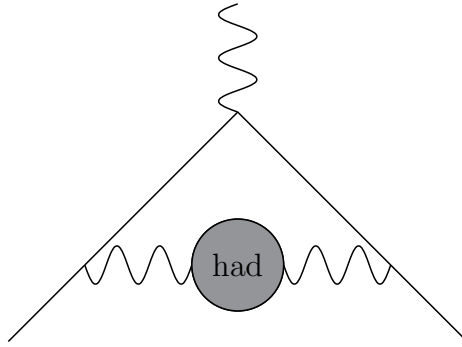


Figure 5.4: The hadronic vacuum polarisation contribution a_μ^{hvp} to the anomalous magnetic moment of the muon, $(g-2)_\mu$. The grey blob indicates hadronic loops. Because quarks do not directly couple to leptons, this hadronic contribution only occurs at $\mathcal{O}(\alpha^2)$

which gives another sizeable contribution to the overall uncertainty.

Experimentally, a_μ has been determined to a similar precision [5, 112]

$$a_\mu^{\text{exp}} = 116592089(63) \times 10^{-11},$$

but with a clear discrepancy of about 3.5σ to the theoretical prediction [109]

$$a_\mu^{\text{theo}} = 116591823(43) \times 10^{-11}.$$

This difference might be a hint towards physics beyond the standard model and for this reason a lot of current research is going into more precise measurements or theoretical predictions of $(g-2)_\mu$. Notably, there are planned experiments at Fermilab and J-PARC [113, 114], which are aiming to reduce the experimental uncertainty by a factor of 4. It would be desirable to reduce the theoretical uncertainty by a similar factor. As has been shown in this section, the theoretical error is mainly driven by the HVP and Hlbl contributions.

Our study can help to reduce the uncertainty in the estimate of the HVP contribution a_μ^{hvp} . In the so-called *time-momentum representation* [115–117], this quantity can be calculated by evaluating the integral [92, 115]

$$a_\mu^{\text{hvp}} = \left(\frac{\alpha}{\pi}\right)^2 \int_0^\infty dx_0 G(x_0) \tilde{K}(x_0; m_\mu), \quad (5.21)$$

where $\tilde{K}(x_0; m_\mu)$ is a known kernel function with m_μ being the mass of the muon and $G(x_0)$ is the vector-vector correlator. The Kernel is defined via

$$\tilde{K}(x_0; m_\mu) = 8\pi^2 \int_0^\infty \frac{d\omega}{\omega} K(\omega^2; m_\mu) [\omega^2 t^2 - 4 \sin^2(\frac{\omega t}{2})], \quad (5.22)$$

$$K(s, m_\mu) = \frac{1}{m_\mu^2} \hat{s} Z(\hat{s})^3 \frac{1 - \hat{s} Z(\hat{s})}{1 + \hat{s} Z(\hat{s})^2}, \quad (5.23)$$

$$Z(\hat{s}) = -\frac{\hat{s} - \sqrt{\hat{s}^2 + 4\hat{s}}}{2\hat{s}}, \quad \hat{s} = \frac{s}{m_\mu^2}, \quad (5.24)$$

or alternatively by the approximations (58) and (60) in [92]. For small x_0 , this correlator can be precisely computed on the lattice, but the signal cannot be traced to arbitrarily large values of x_0 , partly due to noise pollution but also simply because the time extent of the lattice is finite and the integral must be evaluated up to infinite Euclidean time. Getting a good estimate for the long-distance behaviour of $G(x_0)$, which is needed to perform the integral to infinity, is one of the main challenges which comes with this approach. The general idea is therefore to use the direct lattice data up to some cut-off value x_0^{cut} and to determine the part above this value separately. Because $G(x_0)$ should be dominated by the iso-vector correlator at large distances, which in finite volume should be an infinite tower of exponentials of the energy levels in the spectrum,

$$G(x_0) = \sum_{n=0}^{\infty} A_n e^{-E_n x_0}, \quad (5.25)$$

a very simple way to estimate the large- x_0 part of $G(x_0)$ is to describe it by a single-exponential term,

$$G(x_0)_{\text{ext}} = A_0 e^{m_\rho x_0}. \quad (5.26)$$

where we identified E_0 with m_ρ , the naive rho mass, i.e. the plateau value of a correlator whose (smeared) quark interpolators have the quantum numbers of the rho meson and the amplitude A serves as a fit parameter to match the lattice data at the transition value x_0^{cut} . Of course, x_0^{cut} needs to be chosen carefully: If it is too high, the result will likely suffer from noise of the lattice data, but if it is chosen too low, systematic errors are introduced because the assumption that only one state dominates the spectrum will no longer be fulfilled. Of course, it is not clear whether x_0^{cut} can be chosen on every lattice such that both of these problems are taken care of, or in other words that a single exponential suffices in approximating the correlator data in the region where the signal is lost. In [92], the infinite-volume iso-vector correlator

$$G^{\rho\rho}(x_0)_{\text{ext}} = \int_0^\infty d\omega \omega^2 \rho(\omega^2) e^{-\omega x_0}, \quad (5.27)$$

where

$$\rho(\omega^2) = \frac{1}{48\pi^2} \left(1 - \frac{4m_\pi^2}{\omega^2}\right)^{\frac{3}{2}} |F_\pi(\omega)|^2, \quad (5.28)$$

has been used. This formula connects the iso-vector correlator to the pion form

factor and is only valid in a regime where the two-pion channel saturates the iso-vector correlator, which again means that x_0^{cut} has to be chosen at a large enough value. In order to integrate over $F_\pi(\omega)$, one needs a parametrisation of it. In [92], a Gounaris-Sakurai [91] parametrisation has been used, where the input parameters (the naive rho mass m_ρ and the resonance width Γ_ρ) have been determined from the $\langle \rho(t)\rho^\dagger(0) \rangle$ correlator and via a fit to the iso-vector correlator $G^{\rho\rho}(x_0)$. In this work, we have extracted the resonance parameters directly from the scattering phase shift (and have indeed demonstrated that there is a difference between the naive rho mass and the resonance parameter m_ρ), so that we could use these parameters in a Gounaris-Sakurai parametrisation as well. But we also have information about the lowest states in the energy spectrum from the GEVP and we can therefore reconstruct the pre-factors A_n in Equation (5.25) with the current matrix elements we already used to compute F_π :

$$G^{ud}(x_0)_{n_{\text{max}}} = \sum_{n=0}^{n_{\text{max}}} Z_V |A_l|_n |A_c|_n e^{-E_n x_0}, \quad (5.29)$$

with

$$|A_{l/c}|_n = |\langle 0 | J_{l/c} | n \rangle|. \quad (5.30)$$

The subscripts l/c refer to the local (point-like) and the conserved (point-split) currents, respectively and Z_V is the renormalisation constant needed for the local current. This approach has several advantages: We do not only get a more precise estimate for the large- x_0 behaviour of $G(x_0)$, but we also have a way to estimate the remaining excited state contamination. By computing $G(x_0)_{n_{\text{max}}}$ for different values of n_{max} , we can see the estimates converging towards each other. In a region, where $G(x_0)_n$ agrees within errors with $G(x_0)_{n+1}$, we can safely assume that all energy levels $n+2$ and above will not contribute significantly to $G(x_0)$ any more. The integrand of Equation (5.21) for different values of n_{max} can be seen in Figure 5.5. We compare it to the data obtained by a direct calculation of the vector-vector correlator on the same ensembles, performed in [92].

Another way to obtain an estimate for the long-time part of the correlator is to evaluate the integral (5.27) directly using one of the parametrisations for F_π which we presented in the last chapter. The result of this is shown in Figure 5.6, where we compare the vector-vector correlator $G^{\rho\rho}$ obtained from the Gounaris-Sakurai and from the Omnès representation and for comparison show the highest state from Figure 5.5 as well as the lattice data again. One can see readily from Figure 5.5 that on F7, our reconstruction of the vector-vector correlator using Equation (5.29) does not saturate the data from the

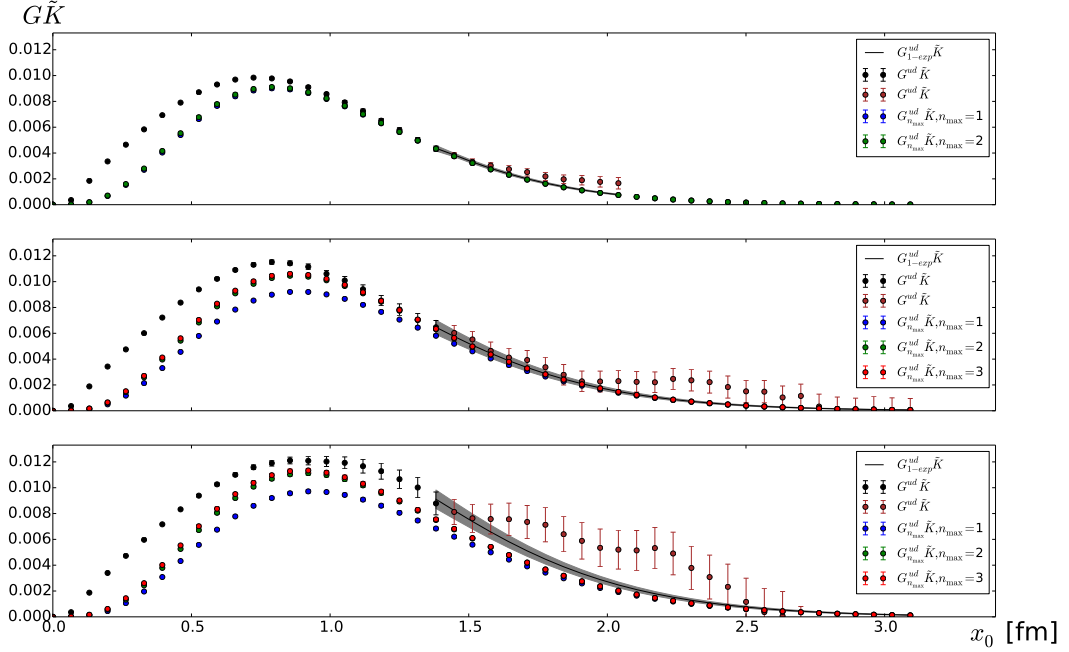


Figure 5.5: a_μ^{hvp} on E5, F6, F7 (top to bottom). Shown are the lattice data points calculated in [92] in black up to x_0^{cut} and in brown above the cut. The coloured dots represent the data from this work using the reconstructed light-quark correlator $G_{n_{\text{max}}}^{\text{ud}}$ from Equation (5.29) for different values of n_{max} . Even for values lower than x_0^{cut} , the contribution obtained only from the first level on E5 saturates the contribution from the lowest two levels. On F6 and F7, the contribution from two levels saturates the contribution obtained from 3 levels also at comparably low x_0 . This means that the computation of further levels would not contribute significantly to a_μ^{hvp} any more and it also shows that a 1-exponential tail is not well motivated on F6 and F7. Also, on E5 and F6, our reconstructed data saturates the lattice data around x_0^{cut} and is much more precise afterwards. On F7, our data lies significantly below the lattice data, which might be caused by correlation by timeslice which overestimates the vector-vector correlator on F7. Already starting at about 1 fm, the data from the direct lattice calculation on F7 seems to deviate from the expected behaviour, leading to this possible overestimation.

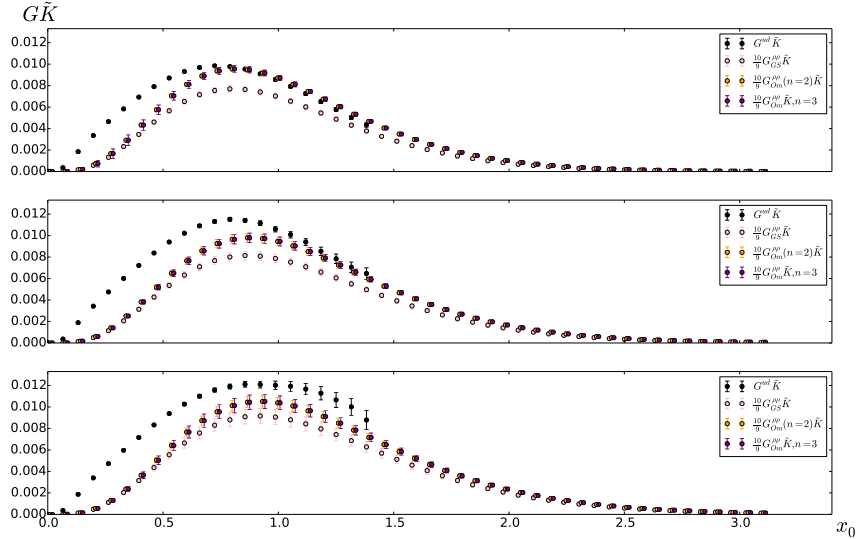


Figure 5.6: a_μ on E5, F6, F7 (top to bottom), showing the data used to compute our final results for a_μ^{hvp} presented in Table 5.4. The black data are the direct computation of the vector-vector computation from Lattice QCD, which is not part of this work and was first presented in [92]. The blue data points are our reconstruction of the light-quark correlator G^{ud} as explained in Equation (5.29) and using all available states, i.e. using two states on E5 and three states on F6 and F7. The other data points are reconstructions of the vector-vector correlator $G^{\rho\rho}$ using Equation (5.27), the pink points using the GS parametrisation and the purple points using the 3-subtracted Omnès representation of F_π . The difference to the 2-subtracted version of the Omnès representation integral is too small to be seen on this plot.

	E5	F6	F7
0 to x_0^{cut}	2.662(26)	3.131(52)	3.462(86)
x_0^{cut} to ∞ (1-exp/GS)	0.484(15)	0.818(52)	1.238(96)
x_0^{cut} to ∞ (G^{ud})	0.473(9)	0.808(13)	1.050(20)
x_0^{cut} to ∞ ($G^{\rho\rho}, n=2$)	0.516(13)	0.776(29)	1.049(48)
x_0^{cut} to ∞ ($G^{\rho\rho}, n=3$)	0.502(13)	0.805(30)	1.078(52)
0 to ∞ (1-exp/GS)	3.146(39)	3.949(99)	4.700(173)
0 to ∞ (G^{ud})	3.135(28)	3.940(59)	4.524(95)
0 to ∞ ($G^{\rho\rho}, n=2$)	3.179(30)	3.907(63)	4.511(102)
0 to ∞ ($G^{\rho\rho}, n=3$)	3.165(31)	3.936(65)	4.540(106)

Table 5.4: Values for a_μ^{hvp} obtained using various methods, in units of 10^{-8} . The first line shows the accumulated integral over the lattice data up to x_0^{cut} . The next four lines show the integral over the long-time tail using the following four methods: (1-exp/GS) is the single-exponential (on E5) or the GS fit (on F6 and F7) to the lattice data, as has been used in [92]. G^{ud} is our extension using the reconstruction of the light-quark correlator using Equation (5.29). $G^{\rho\rho}$ reconstructs the vector-vector correlator using Equation (5.27), where the pion form factor F_π is parametrised by the n -subtracted Omnès representation for $n=2$ and $n=3$. We do not show the results of $G^{\rho\rho}$ reconstructed using the GS parametrisation of F_π as it does not describe our data really well, as can be seen in Figure 5.6.

direct lattice computation of the isovector $G(x_0)$. Unlike in the cases of E5 and F6, it is not really clear where to transition from one method to estimate the correlator to the other. Because the second state the reconstruction of the light-quark correlator G^{ud} on F7 already saturates the third state quite well, we can be reasonably sure that adding more states will not change this picture. Also, the pronounced bump in the lattice data points on higher timeslices on F7 indicates that the data might over-estimate the true correlator a bit. In Figure 5.7, we show the values of a_μ^{hvp} as a function of x_0^{cut} . As expected one can see that on F7, the central value grows significantly for larger transition values. We have also compared our new values for a_μ^{hvp} with the ones from [92] and the chiral extrapolation done in that work in Figure 5.8. One can see there that the value for F7 shifts significantly, but that it comes to an overall better agreement with the chiral extrapolation curve.

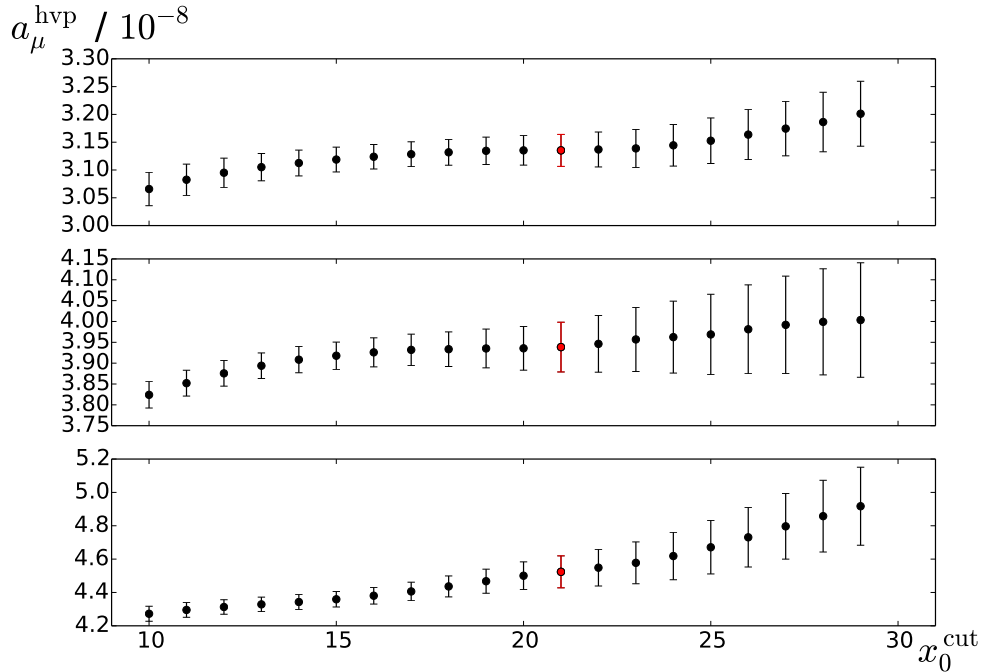


Figure 5.7: Shown is a_μ^{hvp} , obtained via the TMR method as a function of the transition parameter x_0^{cut} in lattice units. From top to bottom, the graphics belong to E5, F6 and F7. The data point highlighted in red belongs to $x_0^{\text{cut}} = 1.38\text{fm}$, which is also the value used in [92]. Because the large- x_0 tail from our analysis lies consistently below the lattice data on F7, the central value of a_μ^{hvp} grows significantly for larger values of x_0^{cut} , unlike on E5 and F6.

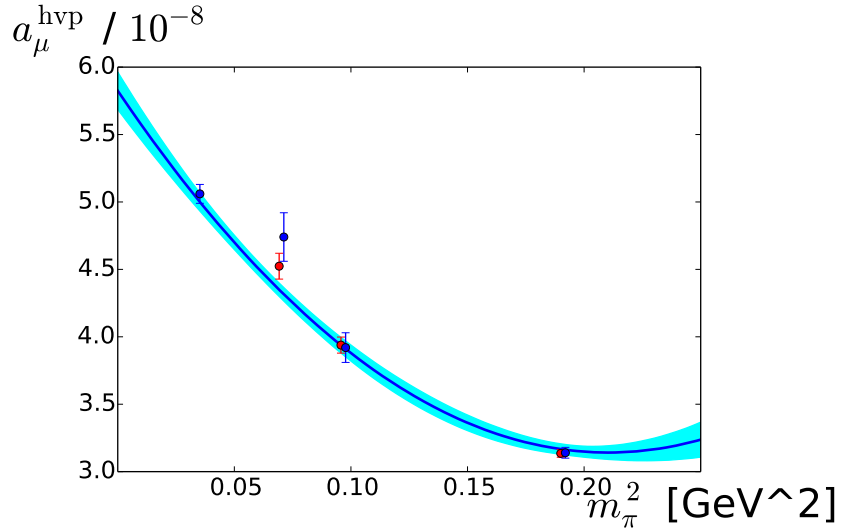


Figure 5.8: Pion mass dependence of a_μ^{hvp} at $\beta = 5.3$. The blue data points and the blue chiral extrapolation of all $\beta = 5.3$ lattices is the data from [92]. The red data points are using the large- x_0 tail from our most precise reconstruction of the correlator, which is the G^{ud} correlator using the matrix elements $|A_\Psi|$ as an input. The displacements of points on the same lattices in x_0 direction are artificial to make the points distinguishable. The leftmost blue point is G8 ($m_\pi = 185$ MeV), which was not computed in this work. Both E5 and F6 are determined more precisely when using our long-time correlator reconstruction and the value of F7, which is comparably imprecise and large in [92], moves significantly towards the chiral extrapolation curve with our data.

Chapter 6

Conclusions

In this thesis we have performed a spectrum-analysis of the $\rho \rightarrow \pi\pi$ channel on three different CLS $N_f = 2$ ensembles at the same lattice spacing. We have used the variational method in a total of 8 different irreps in a centre-of-mass frame and three different moving frames with lattice momenta up to $\mathbf{d}^2 = 3$ and investigated systematic differences in the GEVP by comparing the fixed- t_0 method and the window method. This spectrum information was used in a Lüscher-type analysis to gain access to phase-shift information and extract the resonance parameters of the rho resonance; the mass m_ρ and the coupling $g_{\rho\pi\pi}$. Systematic effects were studied by fitting both to a Breit-Wigner curve as well as to a Gounaris-Sakurai representation of the phase shift.

Using unsmearred operators both for the pointlike local as well as for the point-split conserved current, we could then use this phase-shift information to compute the pion form factor in the timelike region. Because we were using a non-improved version of the lattice currents, we found rather large discretisation effects between the local and conserved currents. We compared our results to the Gounaris-Sakurai representation of the pion form factor, which is parametrised only by the resonance parameters, and found an agreement of only some of our data with this representation. A better description of the pion form factor data was found when we used an Omnès representation of the form factor, which was obtained using a fit to the F_π data, taking the resonance parameters m_ρ and $g_{\rho\pi\pi}$ as fixed parameters. We compared the results from a 2-subtracted and a 3-subtracted version of the Omnès representation. The χ^2 values of those correlated fits are smaller in the 3-subtracted version but still alarmingly large – nevertheless, the fit seems to represent the pion form factor data very well and certainly much better than the Gounaris-Sakurai representation. One of the fit parameters is related to the square radius $\langle r^2 \rangle$ of the pion, which we were then able to compare to the results of an independent lattice calculation on the same ensembles, in which $\langle r^2 \rangle$ was obtained using a chiral extrapolation of the spacelike pion form factor.

Extending a recent determination of the HVP contribution to the anomalous

magnetic moment of the muon, $(g-2)_\mu$, we calculated an independent estimator for the long-time behaviour of the vector-vector correlator $G(x_0)$ in two different ways: Once by approximating the light-quark correlator $G^{ud}(x_0)$ by a tower of exponentials of the centre-of-mass frame energy spectrum, where the amplitudes are related to the current elements used to compute the pion form factor, and secondly by directly computing the vector-vector correlator $G^{\rho\rho}(x_0)$ via an integral over the pion form factor, as parametrised by the Omnès representation. The resulting long-time contributions to a_μ^{hvp} agree with each other and are a huge improvement over the determination with a fit to a single exponent or a Gounaris-Sakurai tail, which was used in the $(g-2)$ study we were comparing our results to, because resonance information was not available at that time. On two of the lattices, a very good agreement of our large-time correlator with the vector-vector correlator directly computed from the lattice was found, and the overall uncertainty could be reduced to a level that it is largely dominated by the lattice data up to the transition value x_0^{cut} . On the most chiral lattice we used, F7, our data under-represented the lattice data significantly, so that we lowered the final value for a_μ^{hvp} by about 1σ . Because the lattice data on F7 seems to show some hump already at about 1 fm, and because we are using a transition value of $x_0^{\text{cut}} \approx 1.38$ fm, the true value for a_μ^{hvp} might be even lower. In any case, the published value for F7 lay prominently above the fit curve of the data points sharing the same lattice spacing and our analysis brought this data point closer to the curve. It is worth noting that F7 is also the only lattice where our determination of the square radius $\langle r^2 \rangle$ lies significantly below the result we were comparing it to.

There are a couple of improvements we could make on this study: First of all, we have shown that discretisation effects in the currents are large and it would be desirable to implement an $\mathcal{O}(a)$ -improved version of the lattice currents. Secondly, there is another and more chiral CLS $\beta = 5.3$ ensemble available, which has a pion mass of $m_\pi = 185$ MeV. An implementation of our full formalism on this much larger lattice would not be trivial though. We are giving a brief account on what would need to be done to get this to work in Appendix E.1.

Appendix A

Full energy spectrum

A.1 t_{\min} dependence of the fit

In the fit to obtain the energy levels from the time dependence of the eigenvalues from the GEVP we are varying the parameter t_{\min} in the fit interval $[t_{\min}, t_{\max}]$. The results for all energy levels in the two methods are shown in this appendix. In all plots the x-axis lists the t_{\min} values, the y-axis indicates the energy E and the error bars to the data points are the statistical uncertainty obtained via the jackknife routine. The black numbers next to each data point are the χ^2/dof values of the correlated fit.

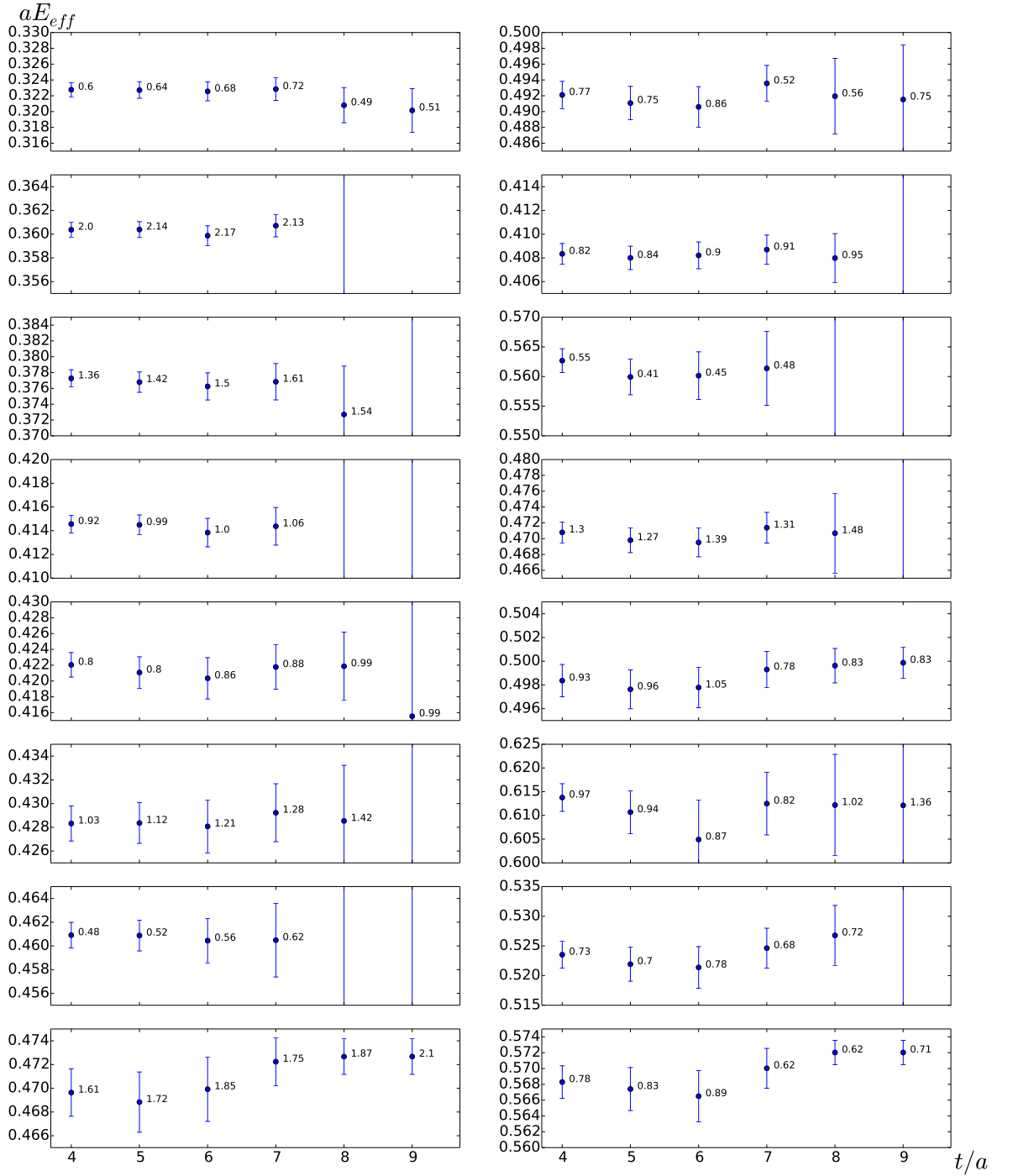


Figure A.1: Same as Figure 4.9 but for all irreps on the E5 lattice, using the fixed- t_0 method. Irreps from top to bottom: $(\mathbf{d}^2 = 0 : T_1)$, $(\mathbf{d}^2 = 1 : A_1)$, $(\mathbf{d}^2 = 1 : E_2)$, $(\mathbf{d}^2 = 2 : A_1)$, $(\mathbf{d}^2 = 2 : B_1)$, $(\mathbf{d}^2 = 2 : B_2)$, $(\mathbf{d}^2 = 3 : A_1)$, $(\mathbf{d}^2 = 3 : E_2)$

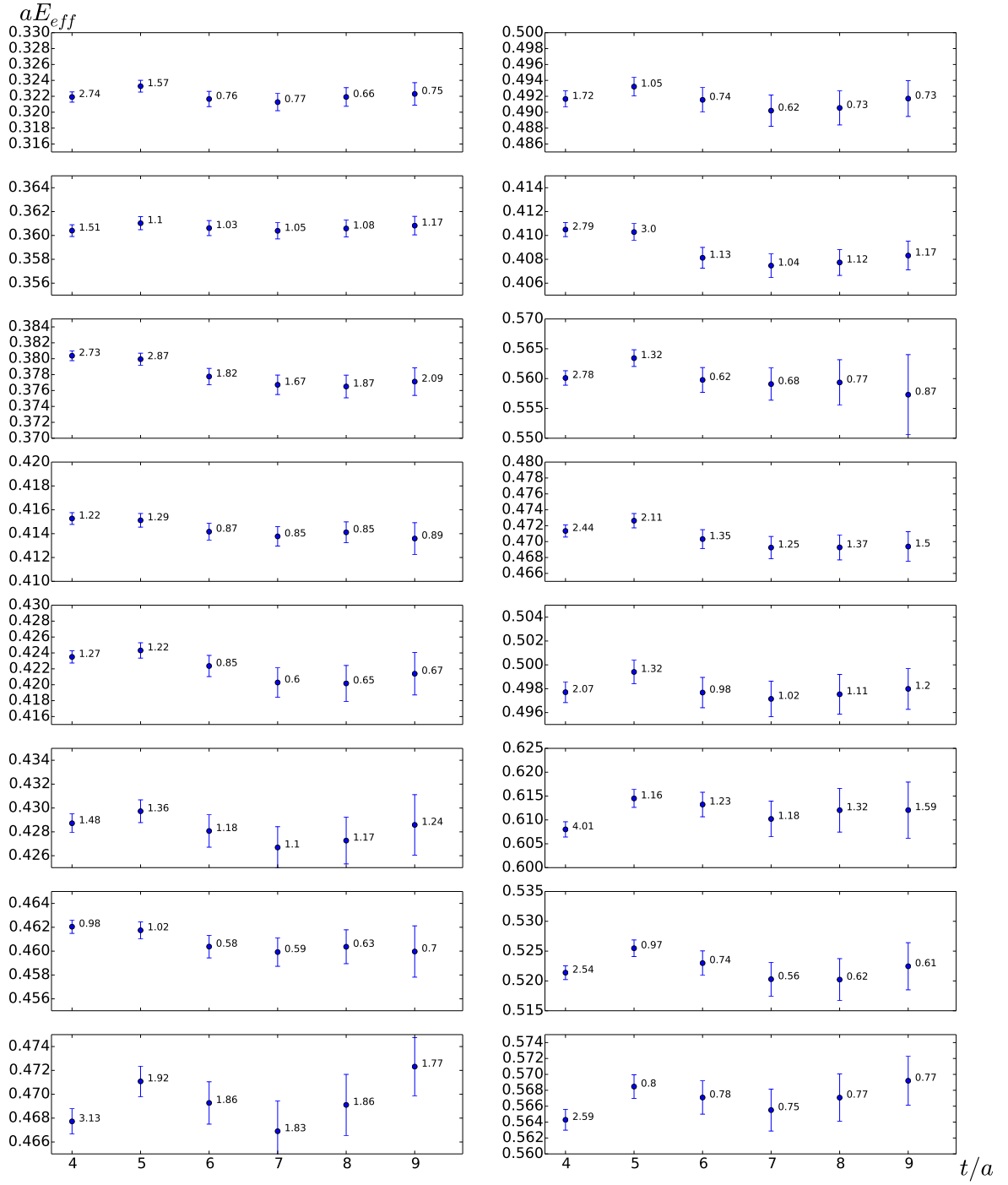


Figure A.2: Same as Figure 4.9 but for all irreps on the E5 lattice, using the window method. Irreps from top to bottom: $(\mathbf{d}^2 = 0 : T_1)$, $(\mathbf{d}^2 = 1 : A_1)$, $(\mathbf{d}^2 = 1 : E_2)$, $(\mathbf{d}^2 = 2 : A_1)$, $(\mathbf{d}^2 = 2 : B_1)$, $(\mathbf{d}^2 = 2 : B_2)$, $(\mathbf{d}^2 = 3 : A_1)$, $(\mathbf{d}^2 = 3 : E_2)$

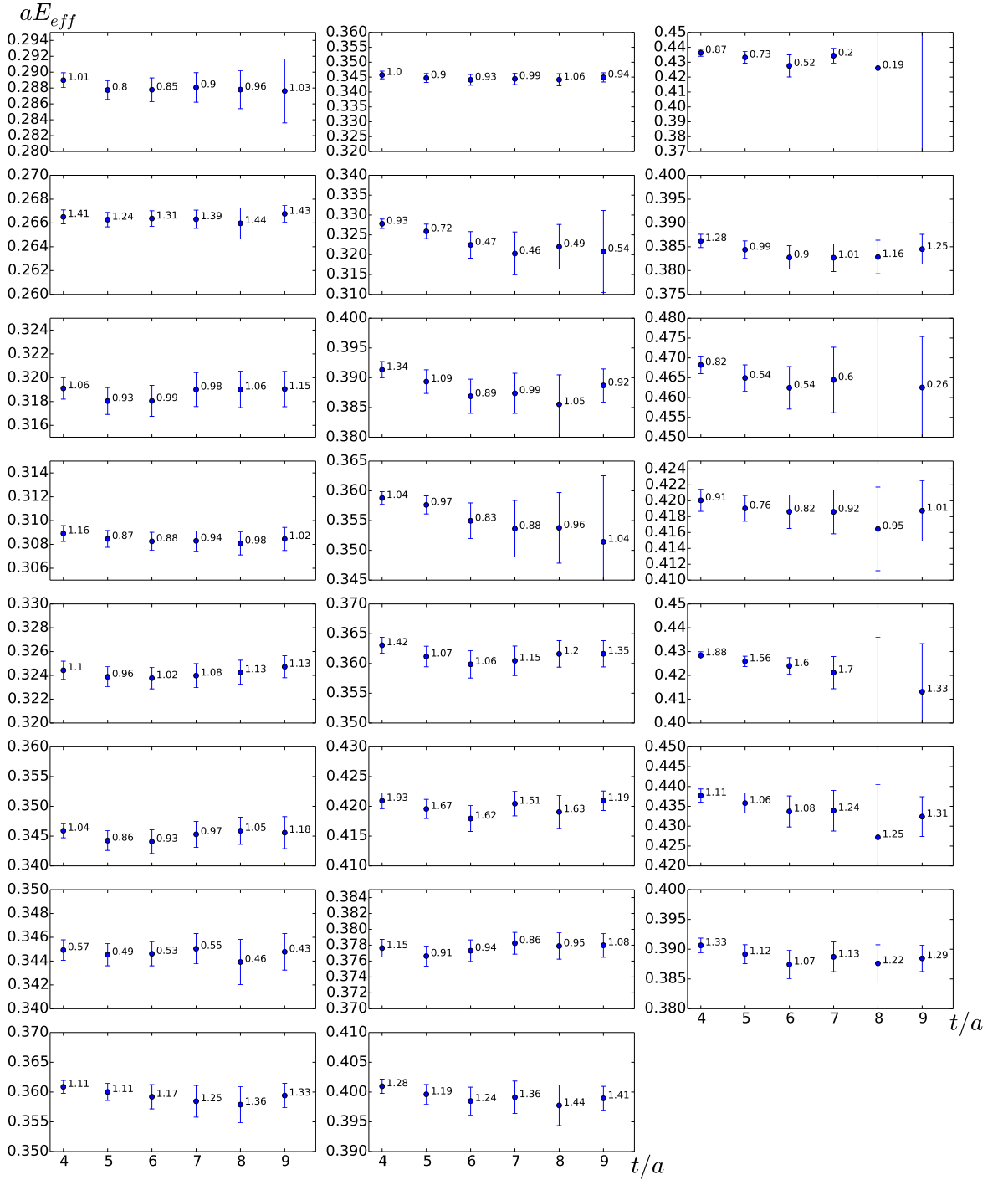


Figure A.3: Same as Figure 4.9 but for all irreps on the F6 lattice, using the fixed- t_0 method. Irreps from top to bottom: $(\mathbf{d}^2 = 0 : T_1)$, $(\mathbf{d}^2 = 1 : A_1)$, $(\mathbf{d}^2 = 1 : E_2)$, $(\mathbf{d}^2 = 2 : A_1)$, $(\mathbf{d}^2 = 2 : B_1)$, $(\mathbf{d}^2 = 2 : B_2)$, $(\mathbf{d}^2 = 3 : A_1)$, $(\mathbf{d}^2 = 3 : E_2)$

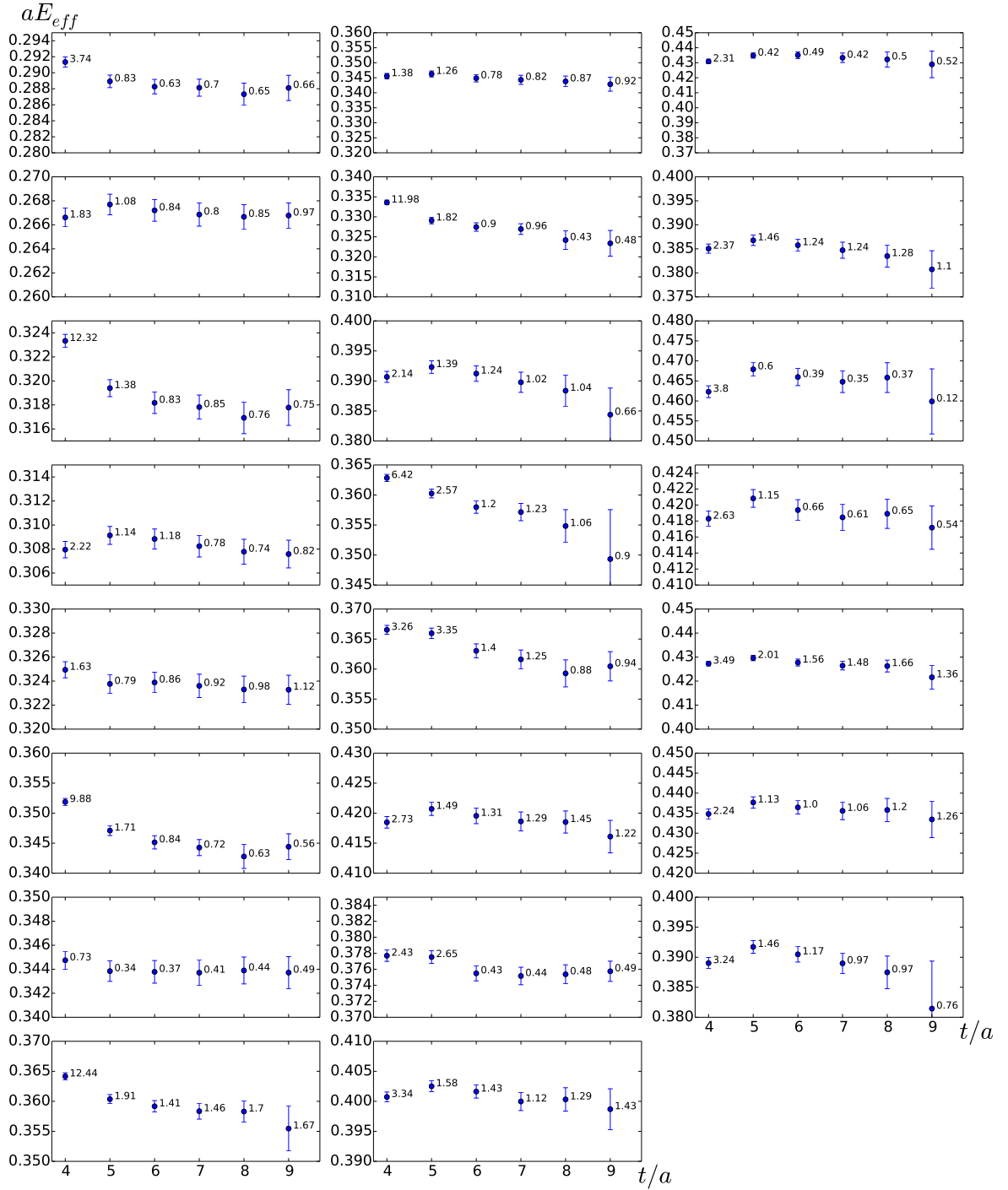


Figure A.4: Same as Figure 4.9 but for all irreps on the F6 lattice, using the window method. Irreps from top to bottom: $(\mathbf{d}^2 = 0 : T_1)$, $(\mathbf{d}^2 = 1 : A_1)$, $(\mathbf{d}^2 = 1 : E_2)$, $(\mathbf{d}^2 = 2 : A_1)$, $(\mathbf{d}^2 = 2 : B_1)$, $(\mathbf{d}^2 = 2 : B_2)$, $(\mathbf{d}^2 = 3 : A_1)$, $(\mathbf{d}^2 = 3 : E_2)$

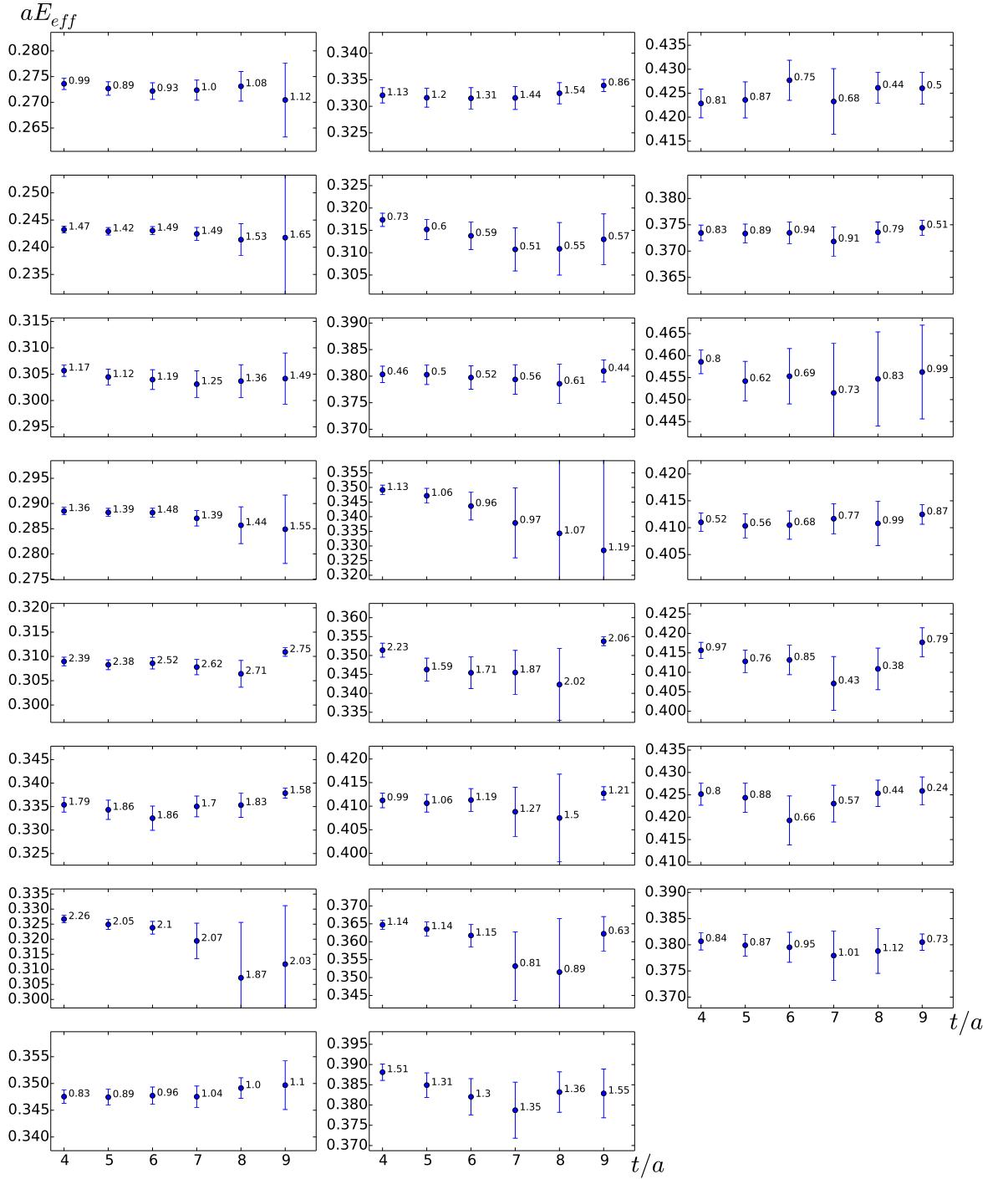


Figure A.5: Same as Figure 4.9 but for all irreps on the F7 lattice, using the fixed- t_0 method. Irreps from top to bottom: $(\mathbf{d}^2 = 0 : T_1)$, $(\mathbf{d}^2 = 1 : A_1)$, $(\mathbf{d}^2 = 1 : E_2)$, $(\mathbf{d}^2 = 2 : A_1)$, $(\mathbf{d}^2 = 2 : B_1)$, $(\mathbf{d}^2 = 2 : B_2)$, $(\mathbf{d}^2 = 3 : A_1)$, $(\mathbf{d}^2 = 3 : E_2)$

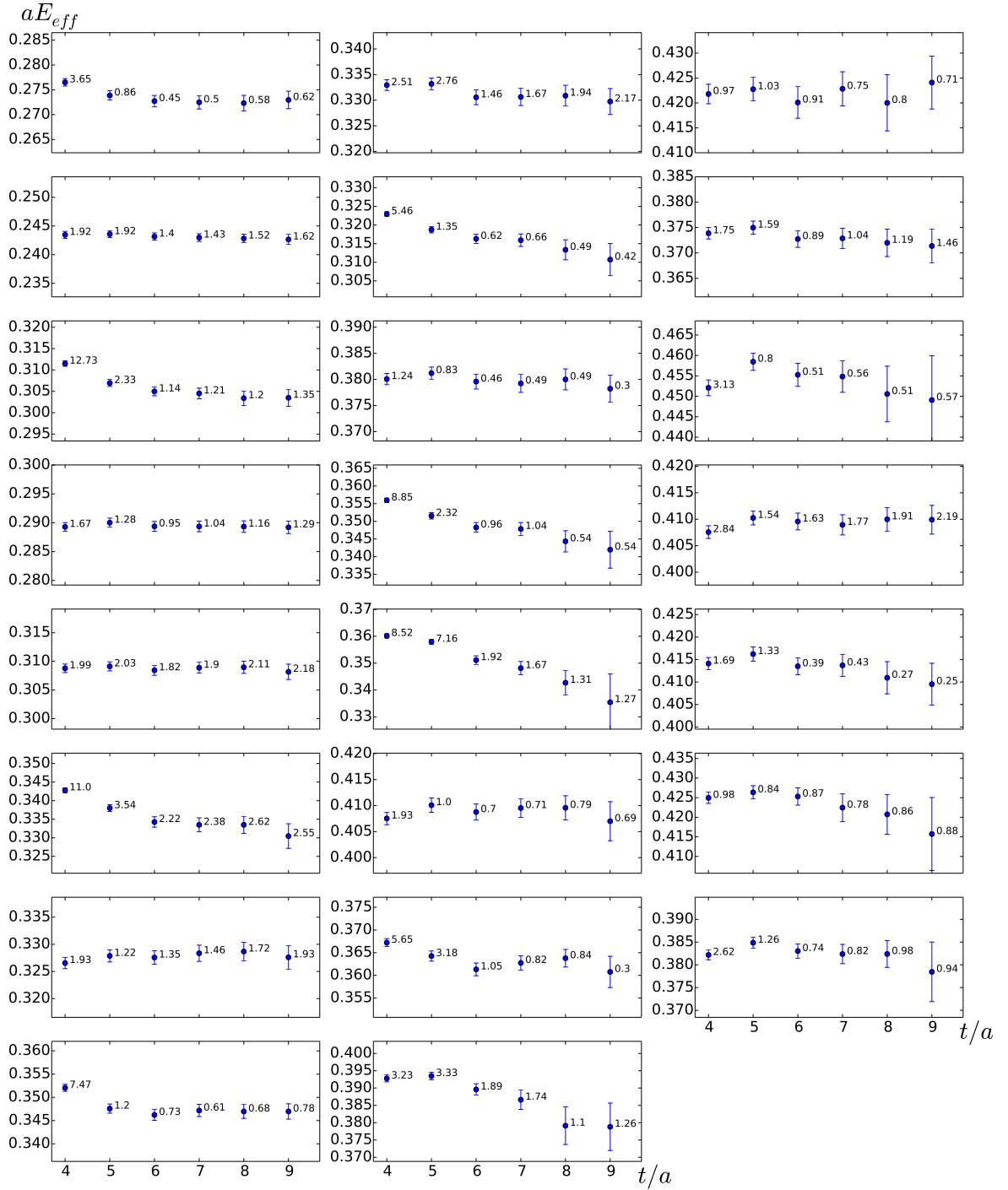


Figure A.6: Same as Figure 4.9 but for all irreps on the F7 lattice, using the window method. Irreps from top to bottom: $(\mathbf{d}^2 = 0 : T_1)$, $(\mathbf{d}^2 = 1 : A_1)$, $(\mathbf{d}^2 = 1 : E_2)$, $(\mathbf{d}^2 = 2 : A_1)$, $(\mathbf{d}^2 = 2 : B_1)$, $(\mathbf{d}^2 = 2 : B_2)$, $(\mathbf{d}^2 = 3 : A_1)$, $(\mathbf{d}^2 = 3 : E_2)$

A.2 Energy spectrum

We are showing here the full energy spectrum which we extracted in our work. The plots are similar to the ones shown in the main text in Figure 4.10 and Figure 4.13 but now show all levels in all irreps.

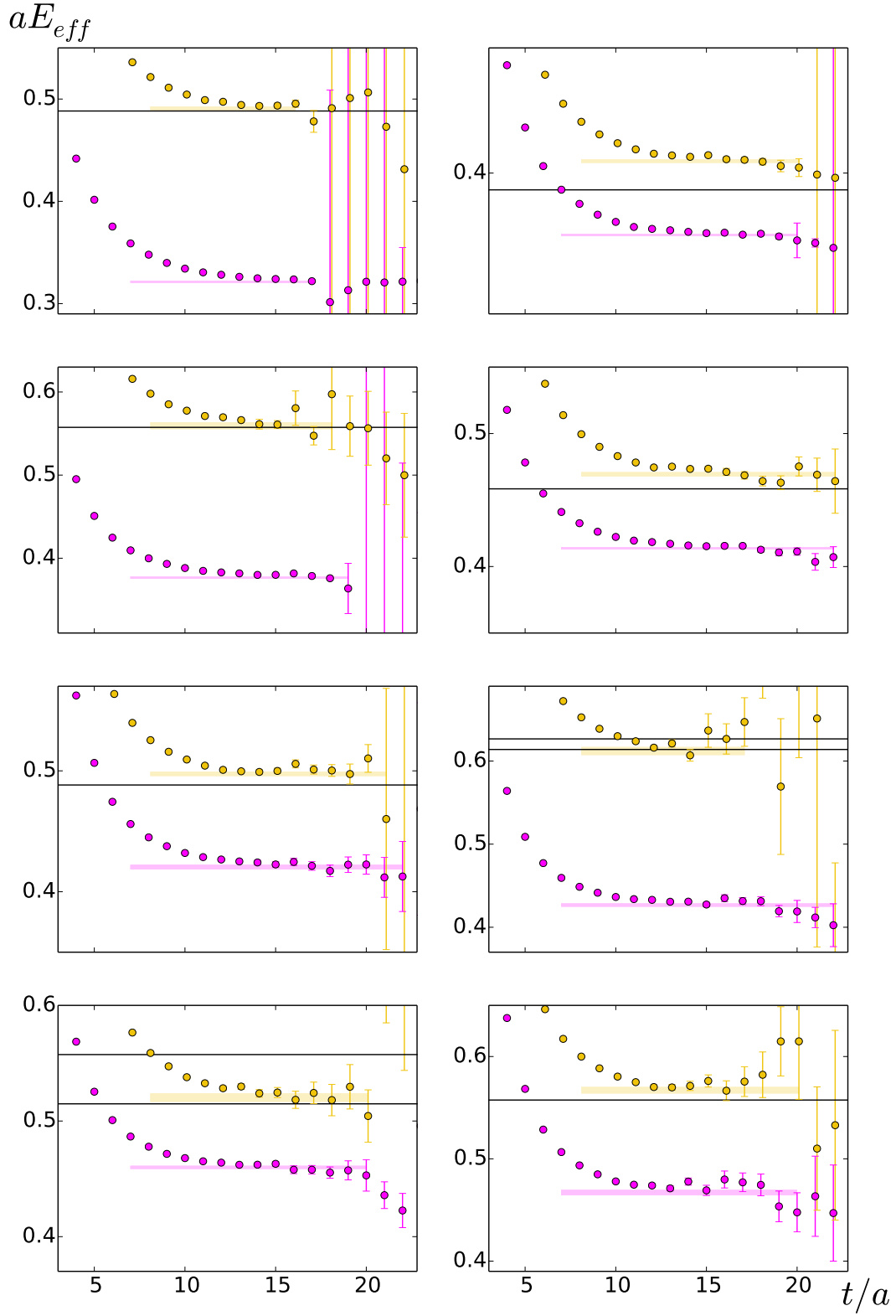


Figure A.7: Same as Figure 4.10 but for all irreps on the E5 lattice, using the window method. Irreps from top to bottom: $(\mathbf{d}^2 = 0 : T_1)$, $(\mathbf{d}^2 = 1 : A_1)$, $(\mathbf{d}^2 = 1 : E_2)$, $(\mathbf{d}^2 = 2 : A_1)$, $(\mathbf{d}^2 = 2 : B_1)$, $(\mathbf{d}^2 = 2 : B_2)$, $(\mathbf{d}^2 = 3 : A_1)$, $(\mathbf{d}^2 = 3 : E_2)$

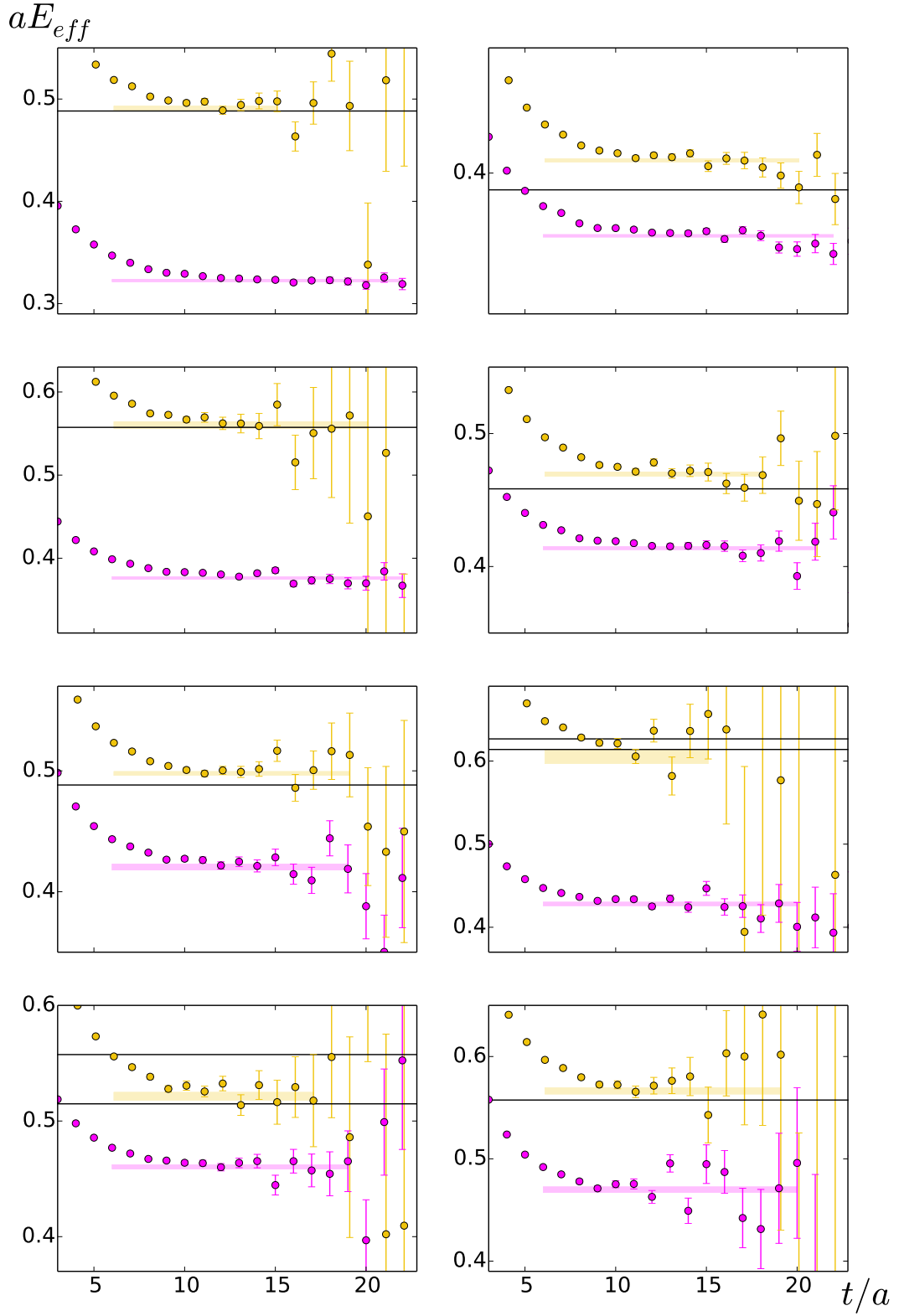


Figure A.8: Same as Figure 4.10 but for all irreps on the E5 lattice, using the fixed- t_0 method. Irreps from top to bottom: ($\mathbf{d}^2 = 0 : T_1$), ($\mathbf{d}^2 = 1 : A_1$), ($\mathbf{d}^2 = 1 : E_2$), ($\mathbf{d}^2 = 2 : A_1$), ($\mathbf{d}^2 = 2 : B_1$), ($\mathbf{d}^2 = 2 : B_2$), ($\mathbf{d}^2 = 3 : A_1$), ($\mathbf{d}^2 = 3 : E_2$)

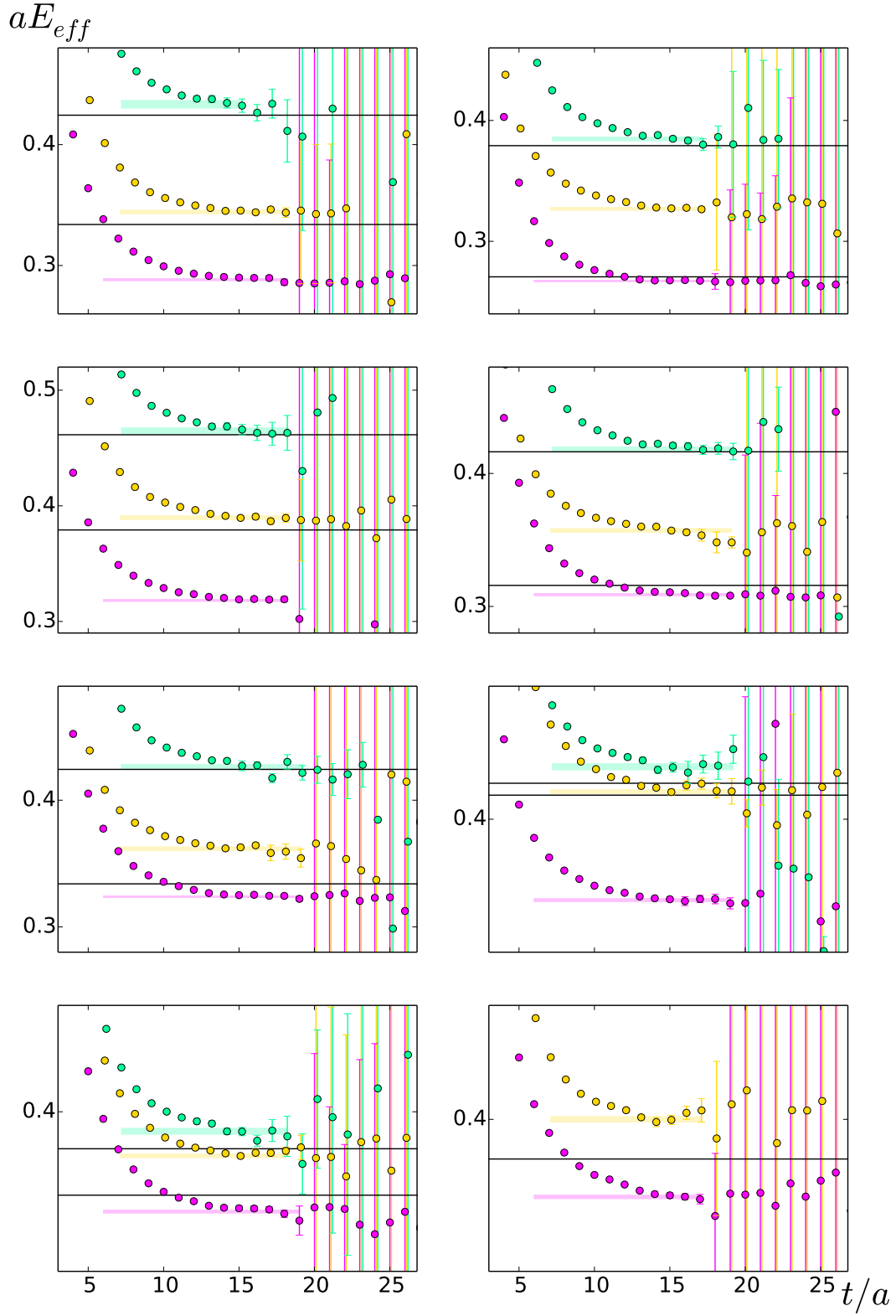


Figure A.9: Same as Figure 4.10 but for all irreps on the F6 lattice, using the window method. Irreps from top to bottom: $(\mathbf{d}^2 = 0 : T_1), (\mathbf{d}^2 = 1 : A_1), (\mathbf{d}^2 = 1 : E_2), (\mathbf{d}^2 = 2 : A_1), (\mathbf{d}^2 = 2 : B_1), (\mathbf{d}^2 = 2 : B_2), (\mathbf{d}^2 = 3 : A_1), (\mathbf{d}^2 = 3 : E_2)$

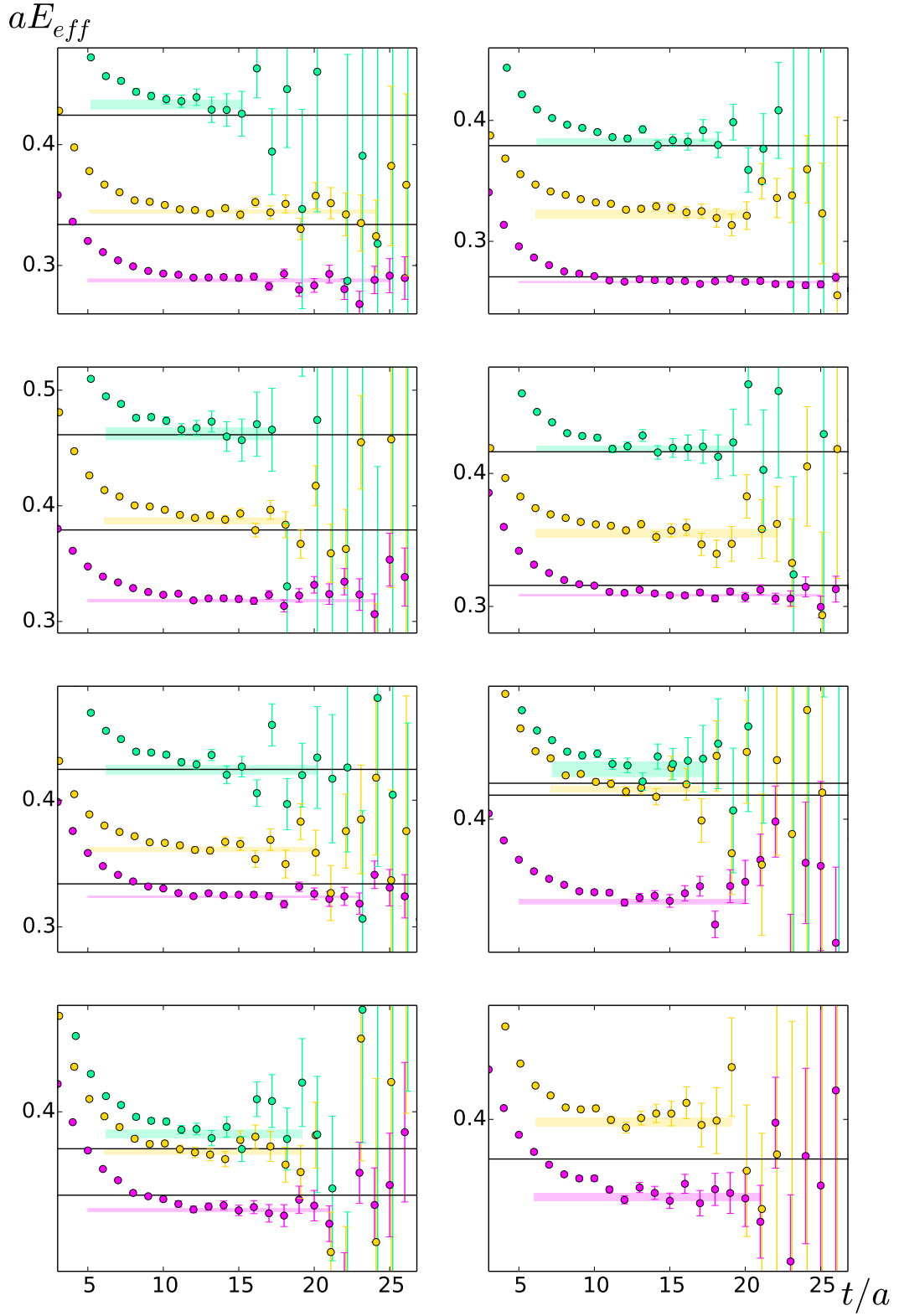


Figure A.10: Same as Figure 4.10 but for all irreps on the F6 lattice, using the fixed- t_0 method. Irreps from top to bottom: ($\mathbf{d}^2 = 0 : T_1$), ($\mathbf{d}^2 = 1 : A_1$), ($\mathbf{d}^2 = 1 : E_2$), ($\mathbf{d}^2 = 2 : A_1$), ($\mathbf{d}^2 = 2 : B_1$), ($\mathbf{d}^2 = 2 : B_2$), ($\mathbf{d}^2 = 3 : A_1$), ($\mathbf{d}^2 = 3 : E_2$)

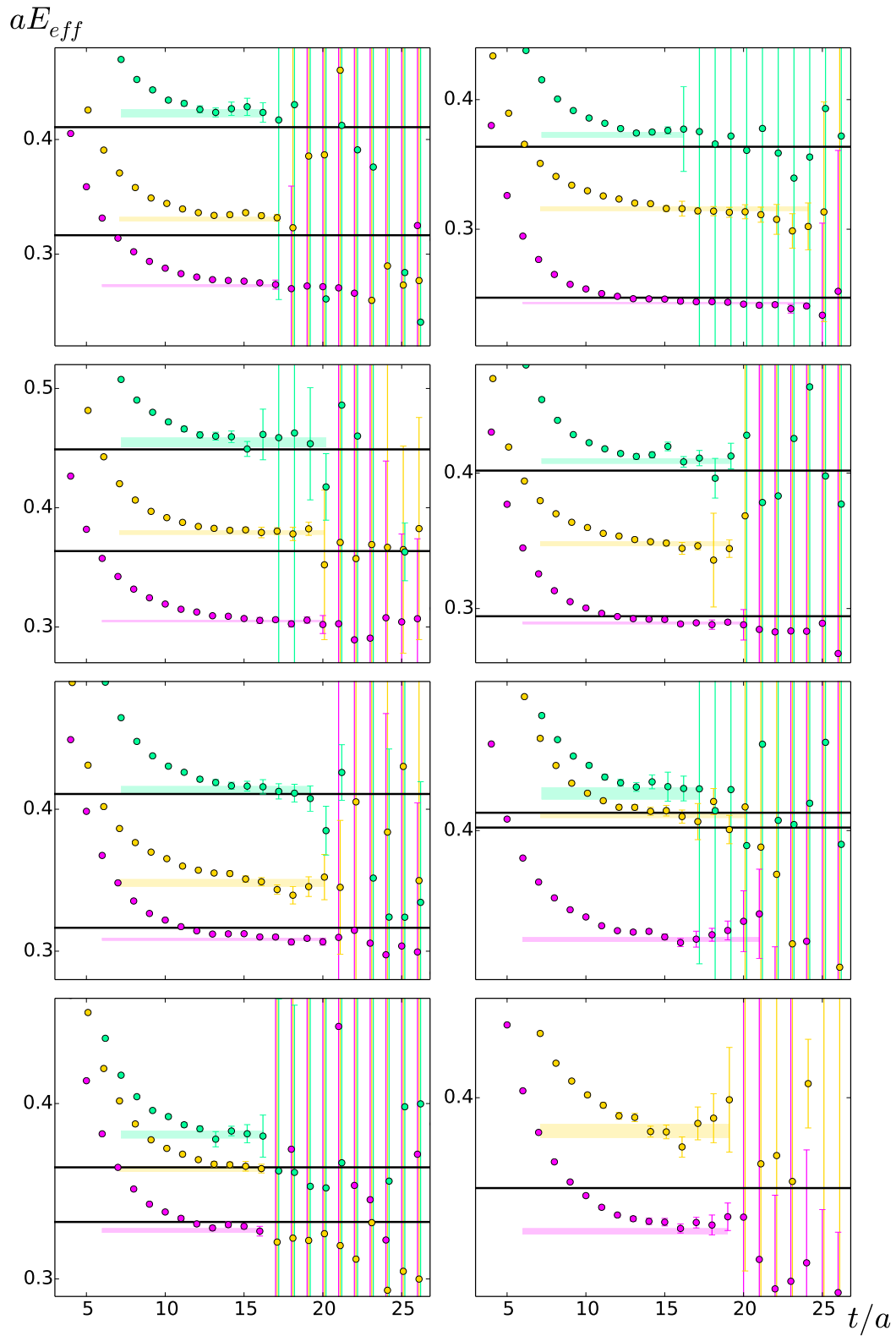


Figure A.11: Same as Figure 4.10 but for all irreps on the F7 lattice, using the window method. Irreps from top to bottom: $(\mathbf{d}^2 = 0 : T_1)$, $(\mathbf{d}^2 = 1 : A_1)$, $(\mathbf{d}^2 = 1 : E_2)$, $(\mathbf{d}^2 = 2 : A_1)$, $(\mathbf{d}^2 = 2 : B_1)$, $(\mathbf{d}^2 = 2 : B_2)$, $(\mathbf{d}^2 = 3 : A_1)$, $(\mathbf{d}^2 = 3 : E_2)$

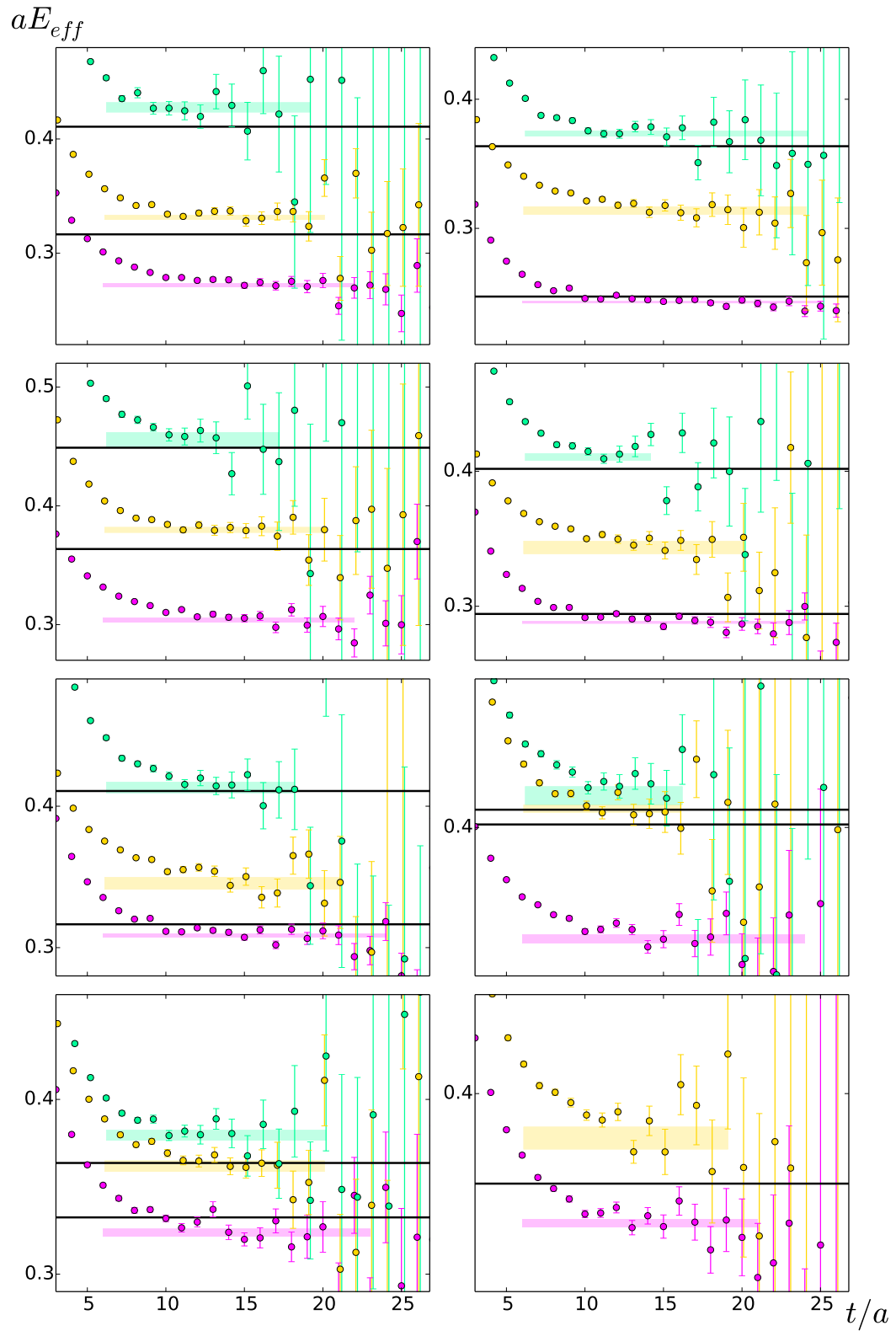


Figure A.12: Same as Figure 4.10 but for all irreps on the F7 lattice, using the fixed- t_0 method. Irreps from top to bottom: ($\mathbf{d}^2 = 0 : T_1$), ($\mathbf{d}^2 = 1 : A_1$), ($\mathbf{d}^2 = 1 : E_2$), ($\mathbf{d}^2 = 2 : A_1$), ($\mathbf{d}^2 = 2 : B_1$), ($\mathbf{d}^2 = 2 : B_2$), ($\mathbf{d}^2 = 3 : A_1$), ($\mathbf{d}^2 = 3 : E_2$)

Appendix B

Ratios

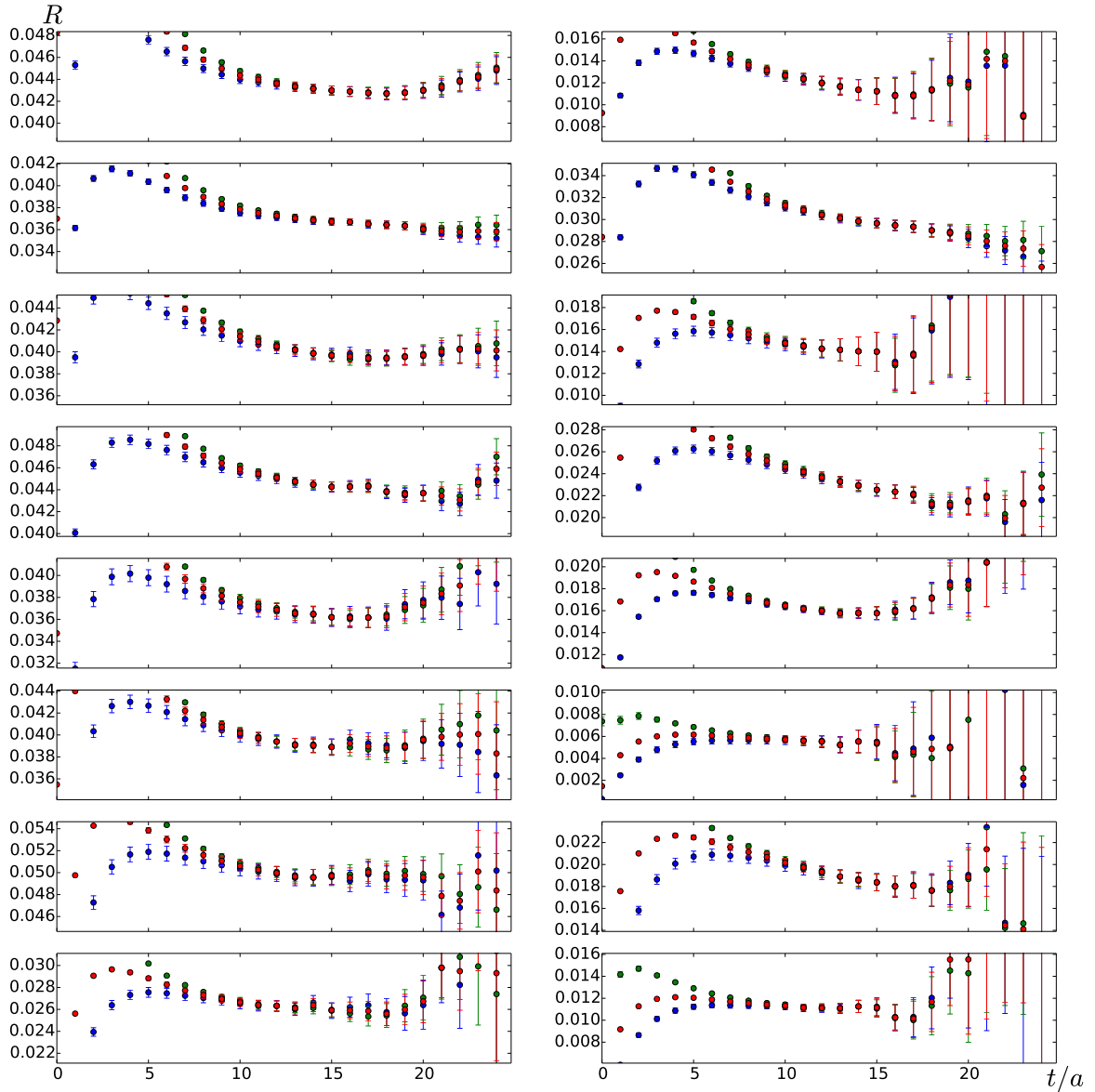


Figure B.1: The three different ratios R_1 (red) R_2 (blue) and R_3 (green) defined in Chapter 4.4 and used to extract the matrix elements $|A_\Psi|$ needed for the computation of F_π on E5, obtained using the fixed- t_0 method and a point-split (conserved) current.

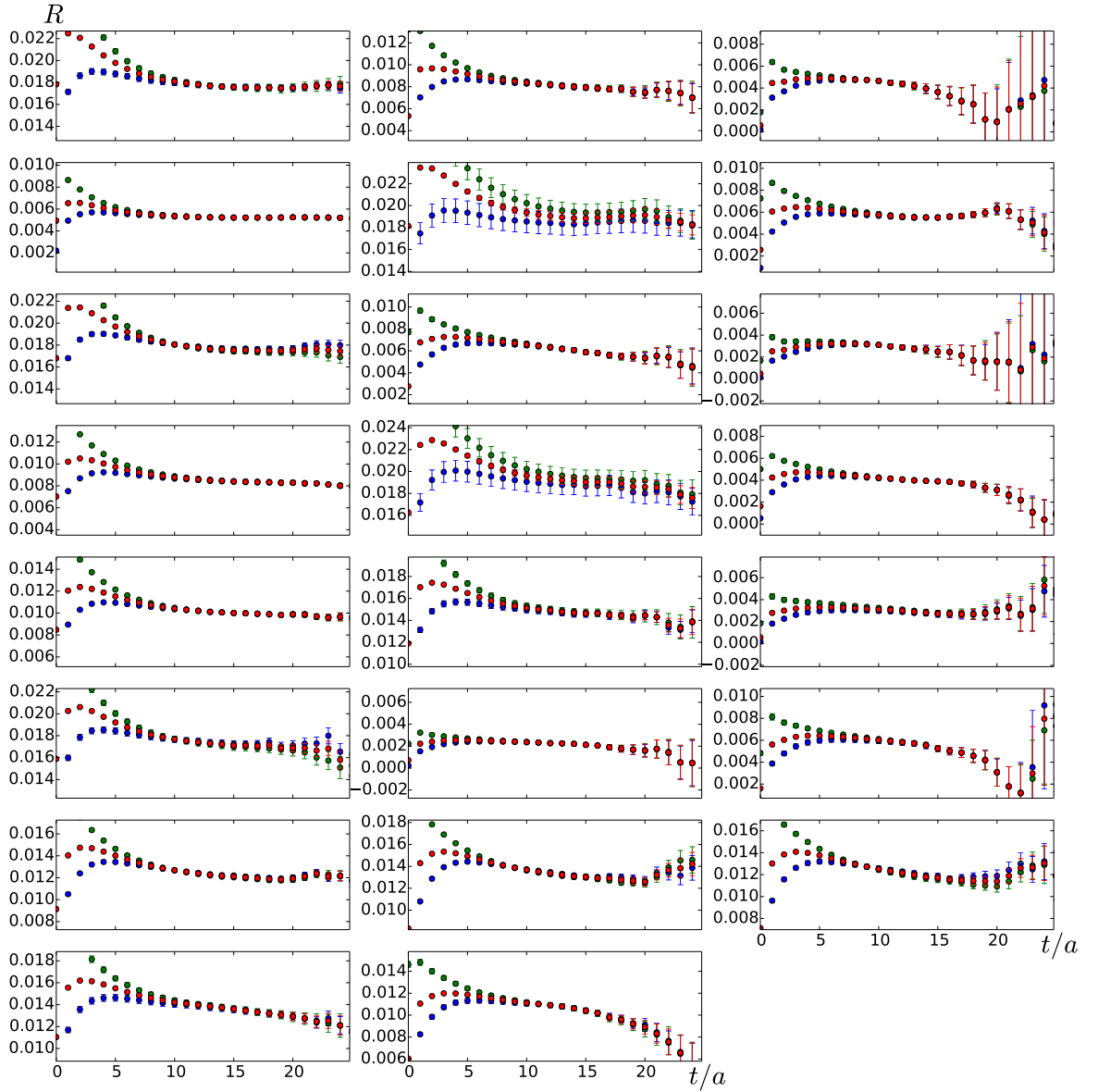


Figure B.2: Same as Figure B.1 but showing the ratios obtained using the point-split (conserved) current on F6 and in the fixed- t_0 method.

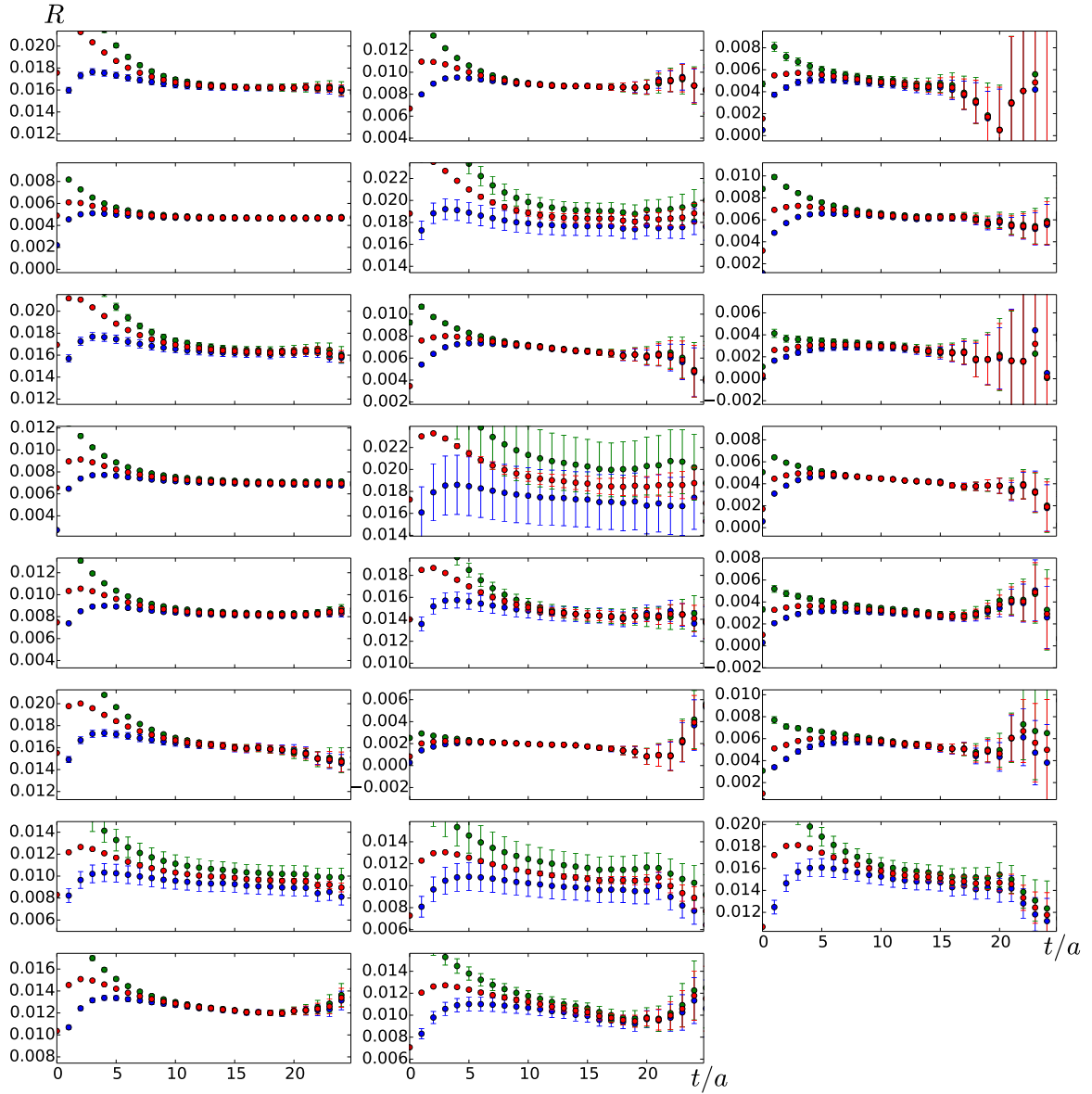


Figure B.3: Same as Figure B.1 but showing the ratios obtained using the point-split (conserved) current on F7 and in the fixed- t_0 method.

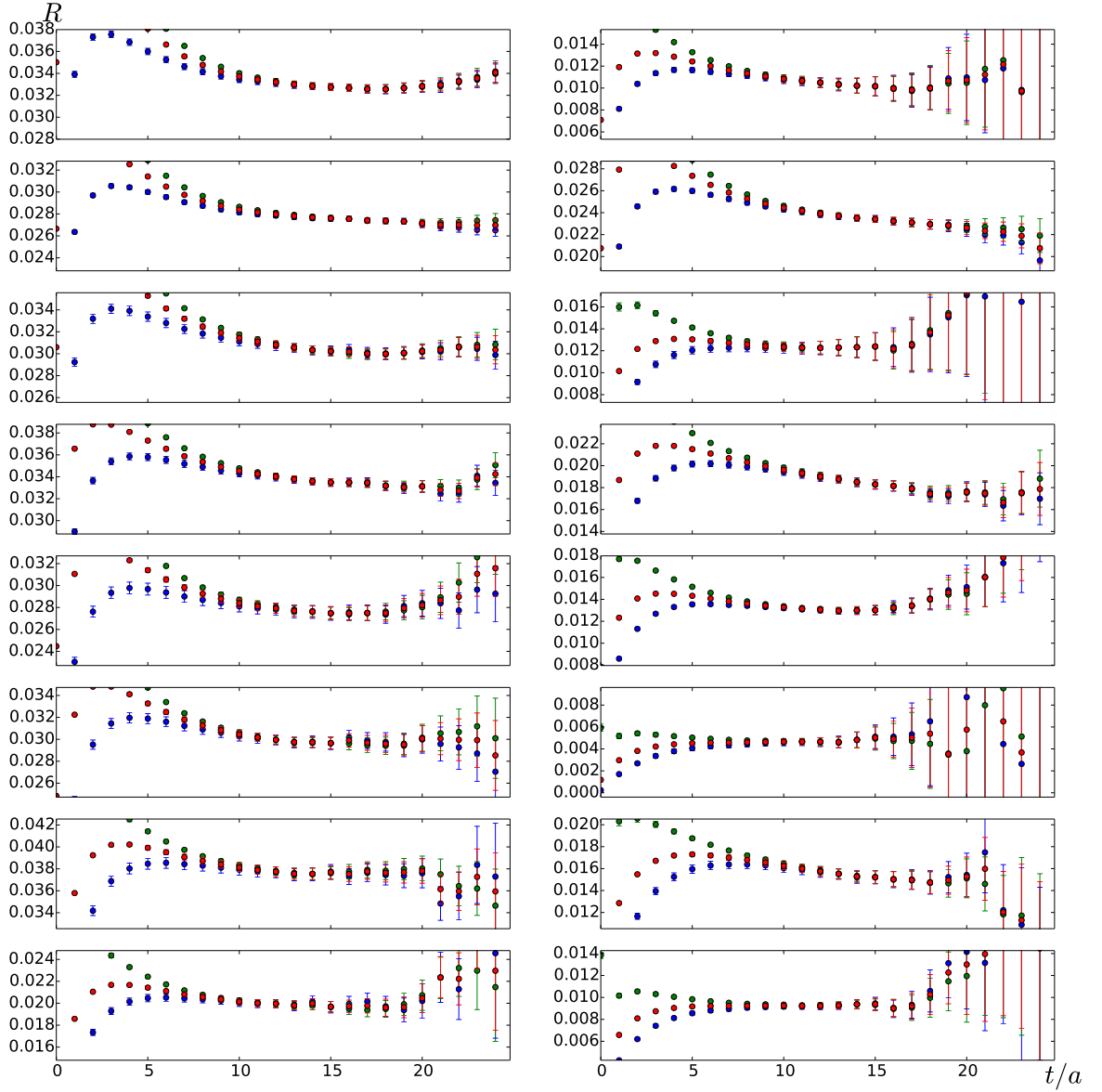


Figure B.4: Same as Figure B.1 but showing the ratios obtained using the pointlike (local) current on E5 and in the fixed- t_0 method. Not yet renormalised with Z_V .

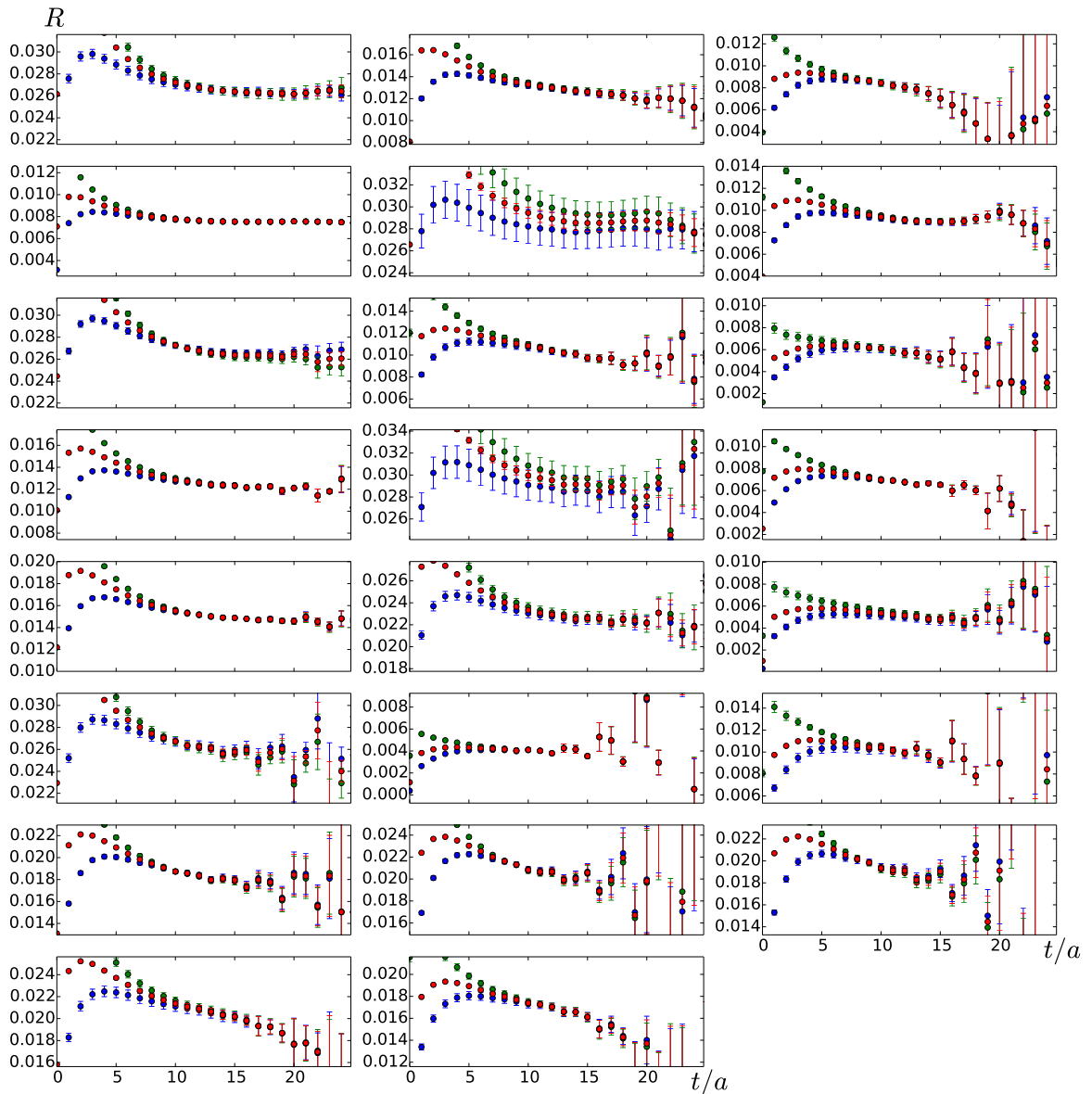


Figure B.5: Same as Figure B.1 but showing the ratios obtained using the pointlike (local) current on F6 and in the fixed- t_0 method. Not yet renormalised with Z_V .

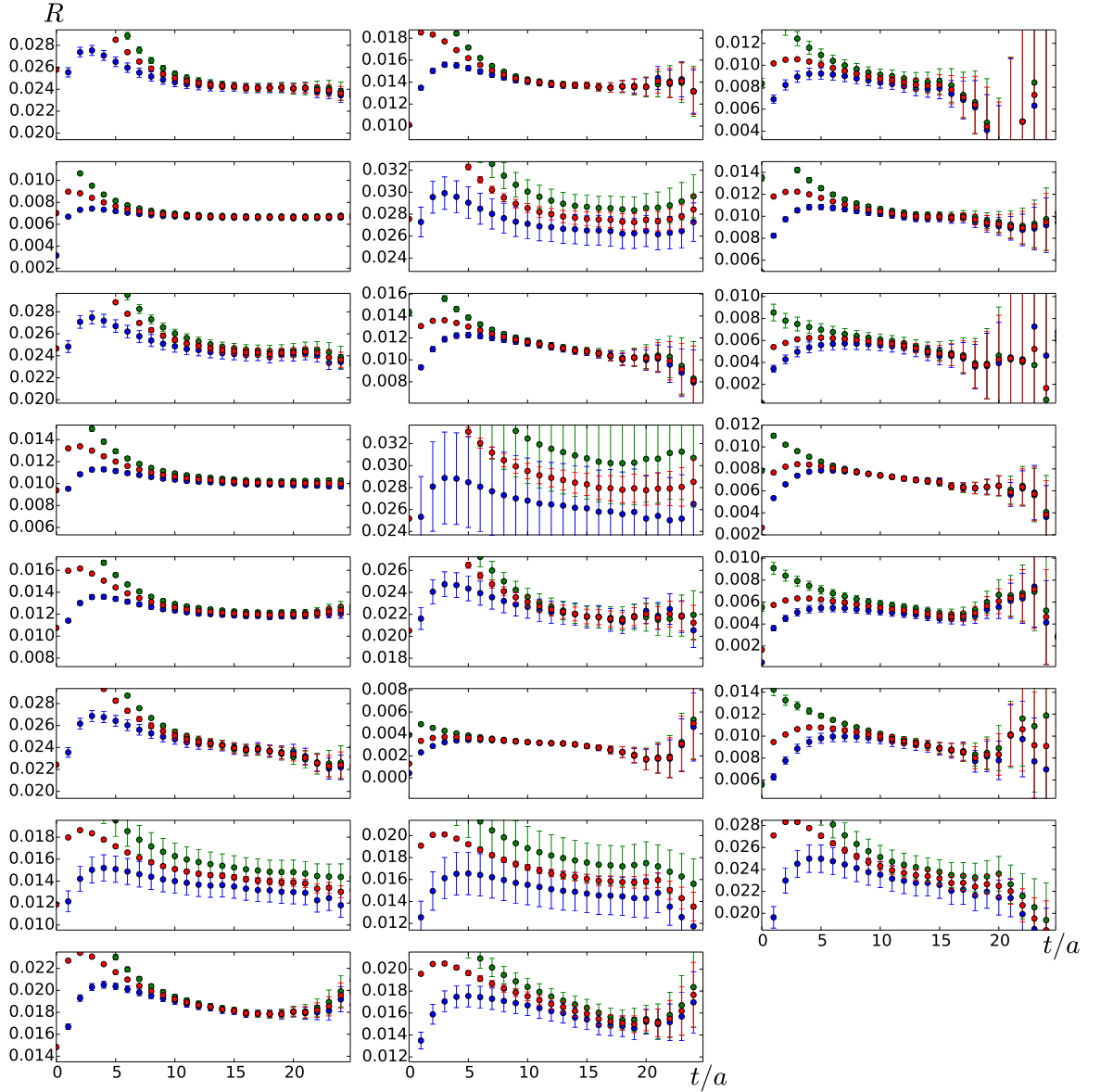


Figure B.6: Same as Figure B.1 but showing the ratios obtained using the pointlike (local) current on F7 and in the fixed- t_0 method. Not yet renormalised with Z_V .

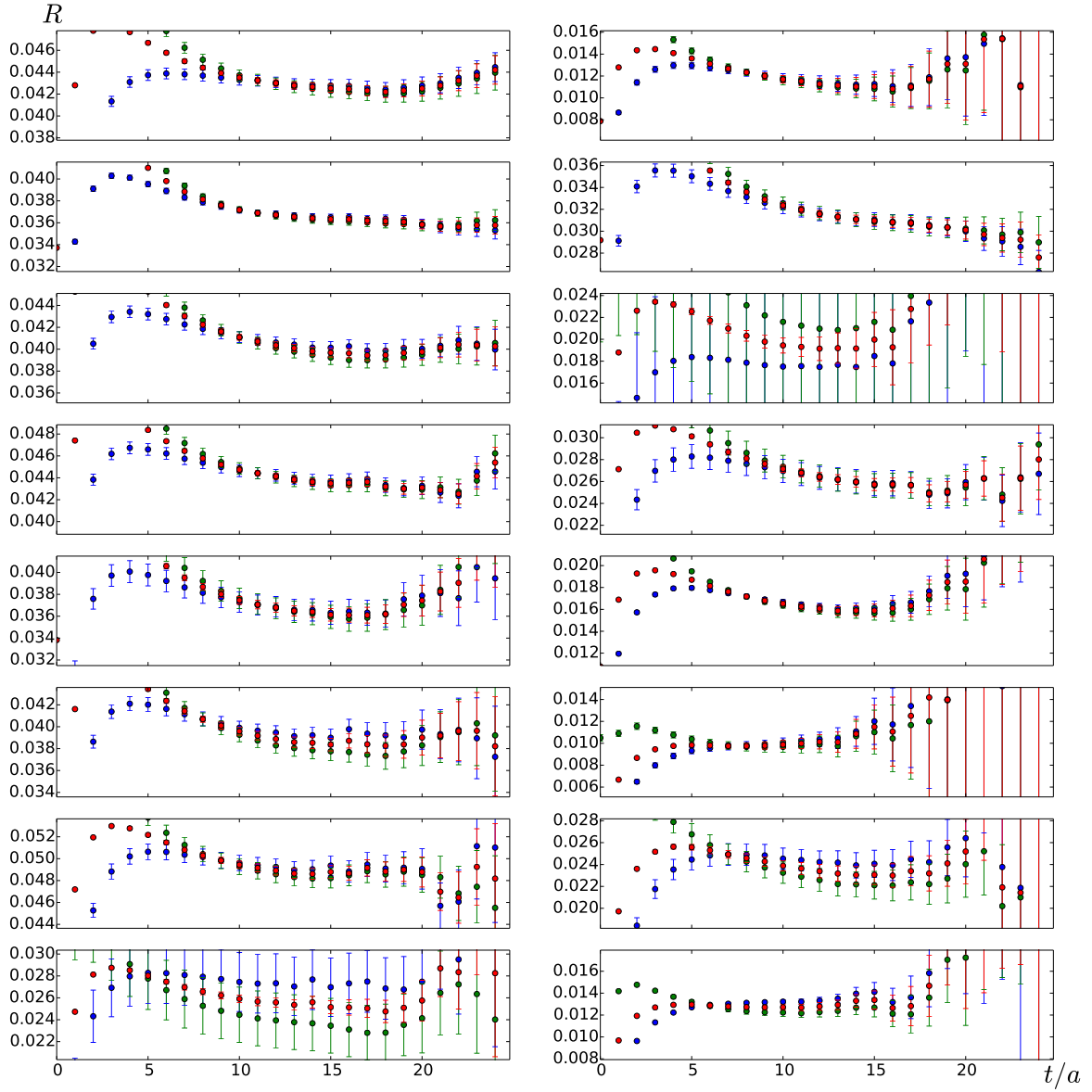


Figure B.7: Same as Figure B.1 but showing the ratios obtained using the point-split (conserved) current on E5 and in the window method.

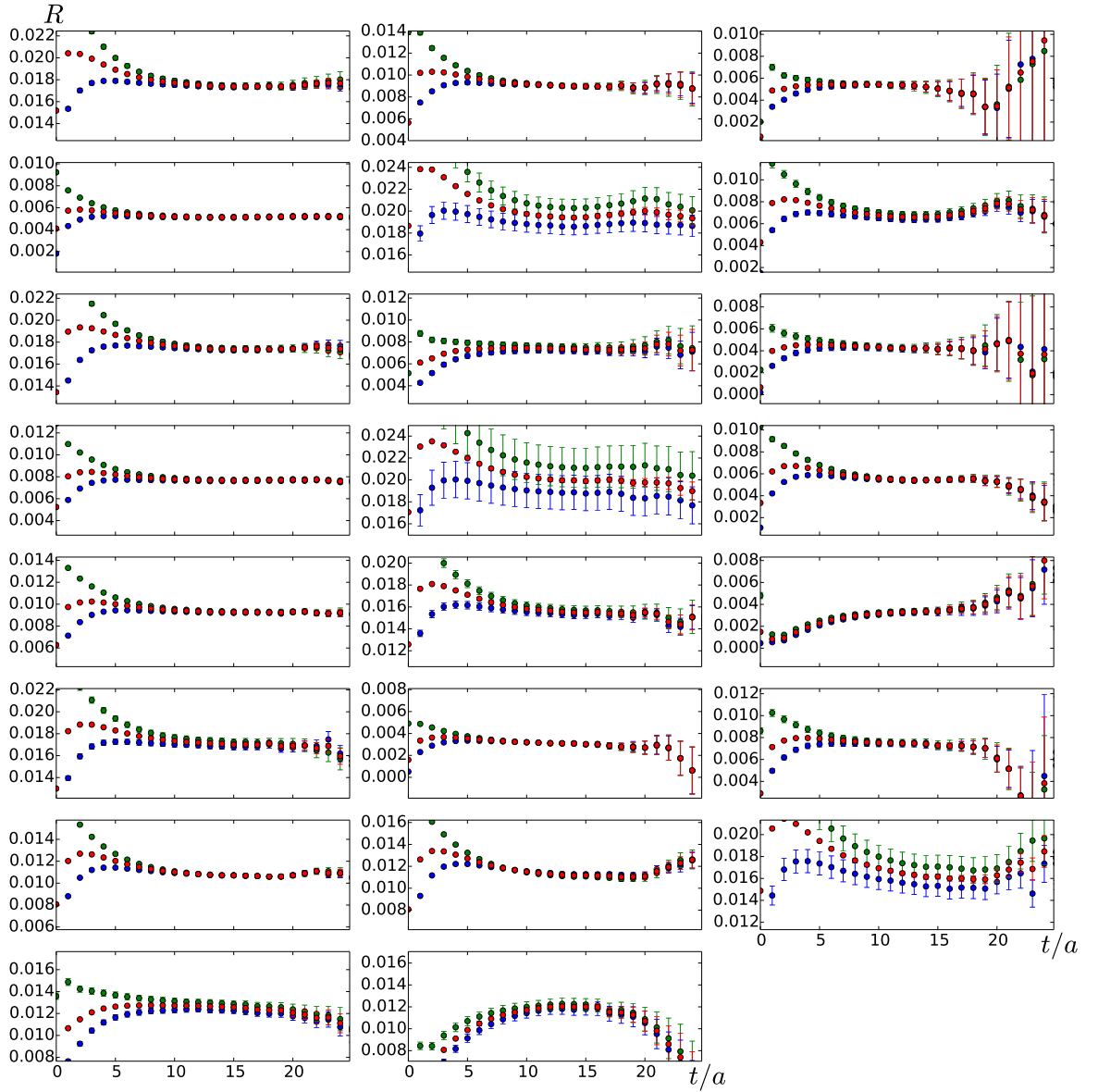


Figure B.8: Same as Figure B.1 but showing the ratios obtained using the point-split (conserved) current on F6 and in the window method.

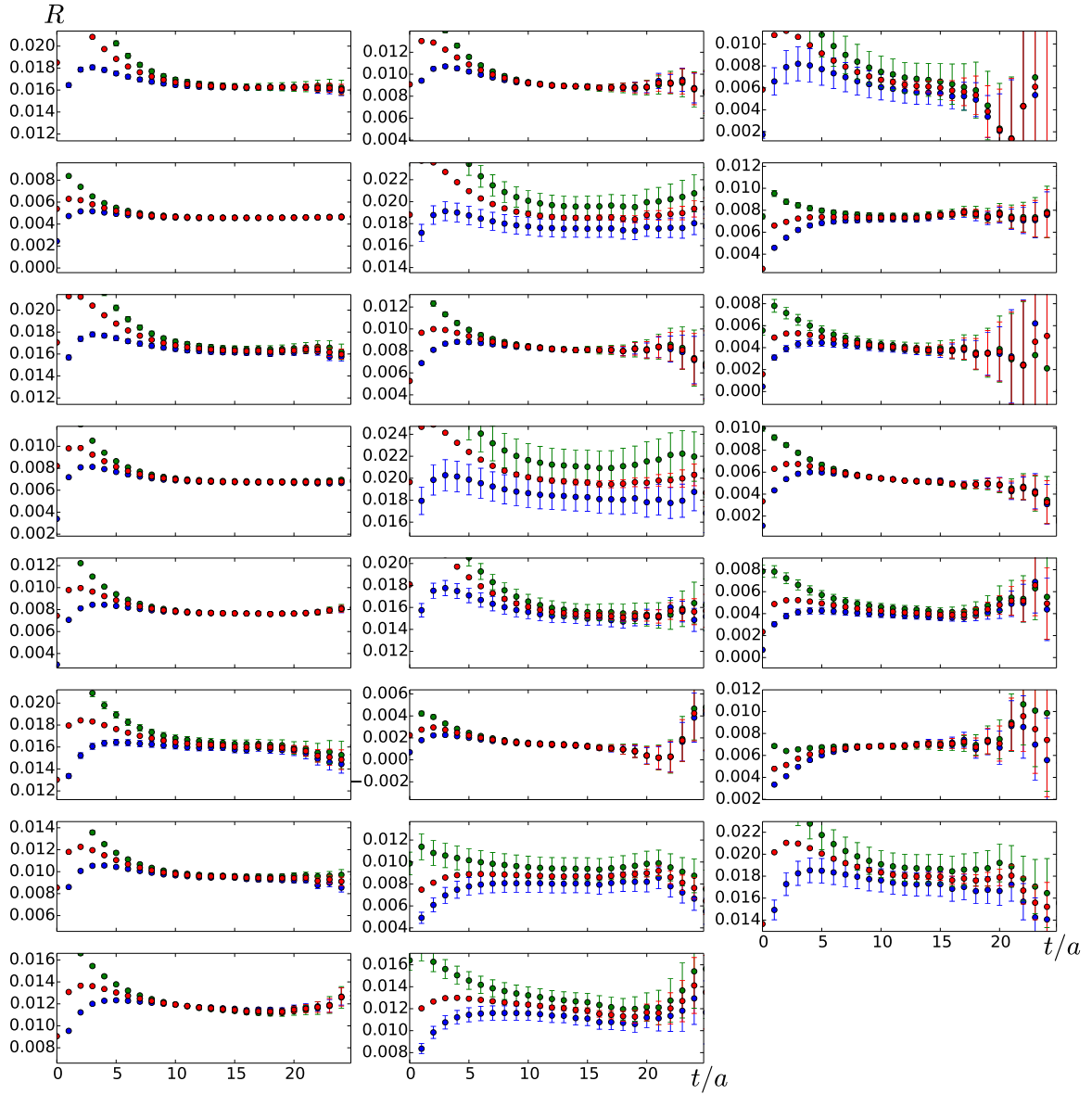


Figure B.9: Same as Figure B.1 but showing the ratios obtained using the point-split (conserved) current on F7 and in the window method.

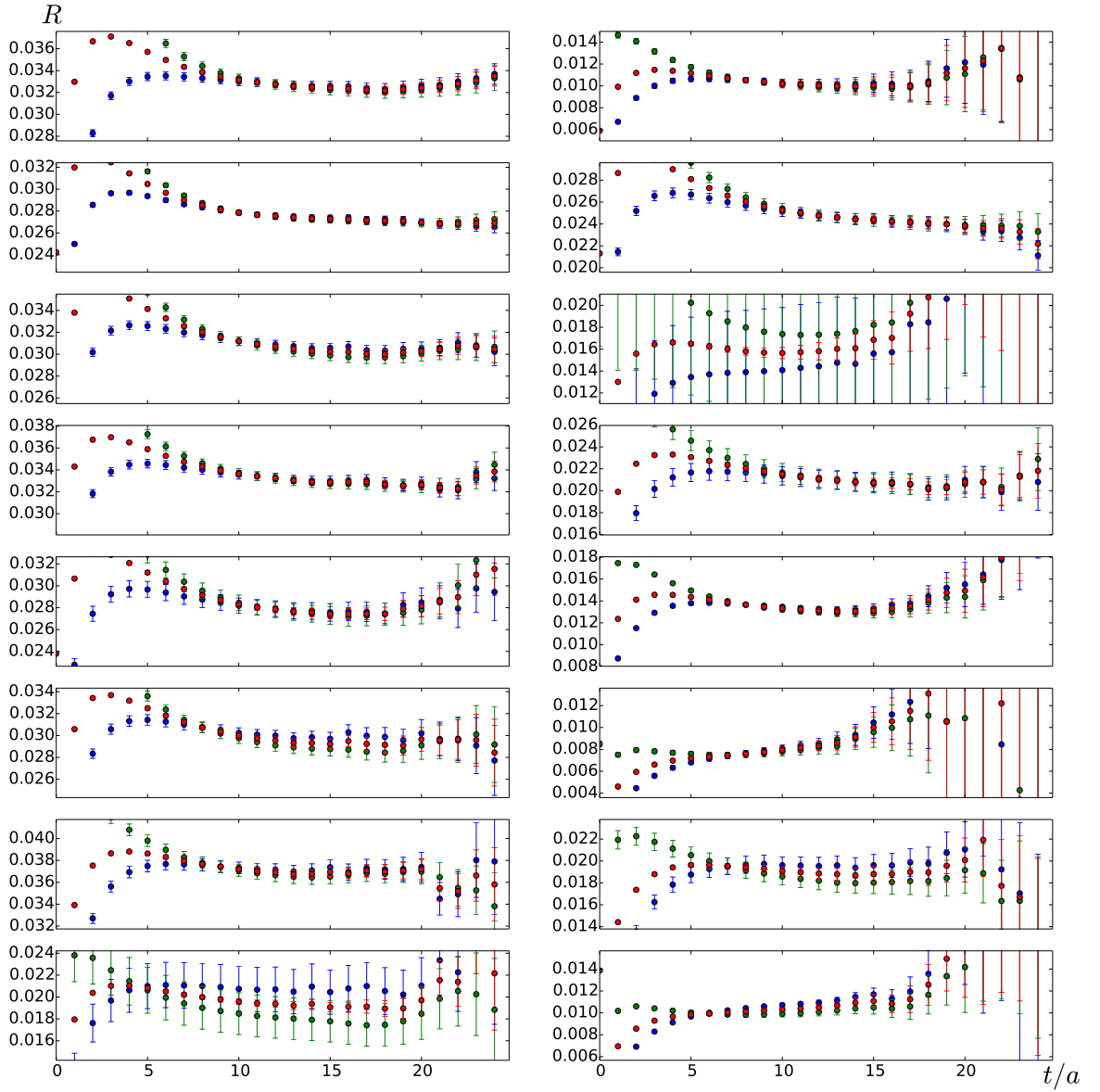


Figure B.10: Same as Figure B.1 but showing the ratios obtained using the pointlike (local) current on E5 and in the window method. Not yet renormalised with Z_V .

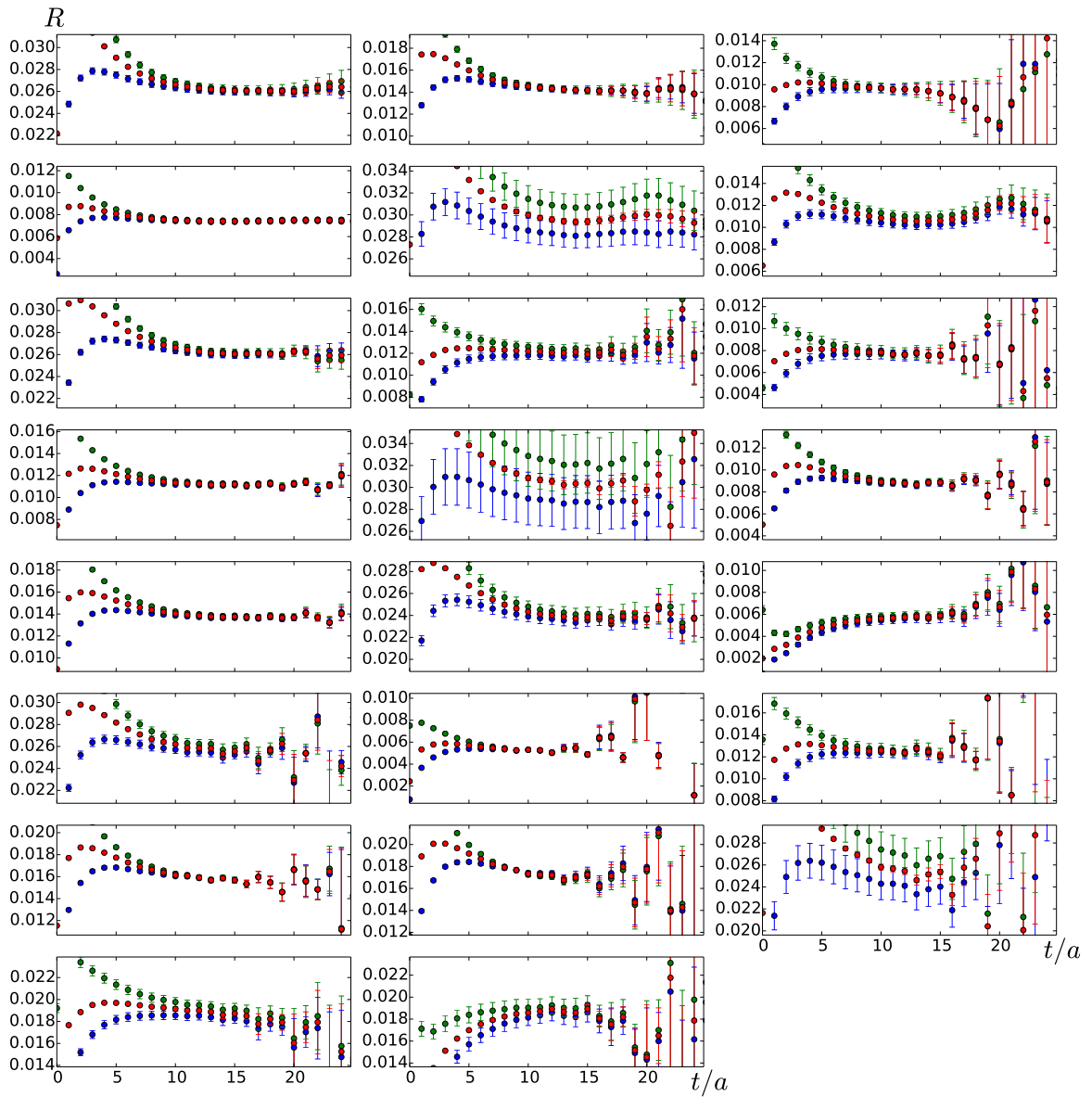


Figure B.11: Same as Figure B.1 but showing the ratios obtained using the pointlike (local) current on F6 and in the window method. Not yet renormalised with Z_V .

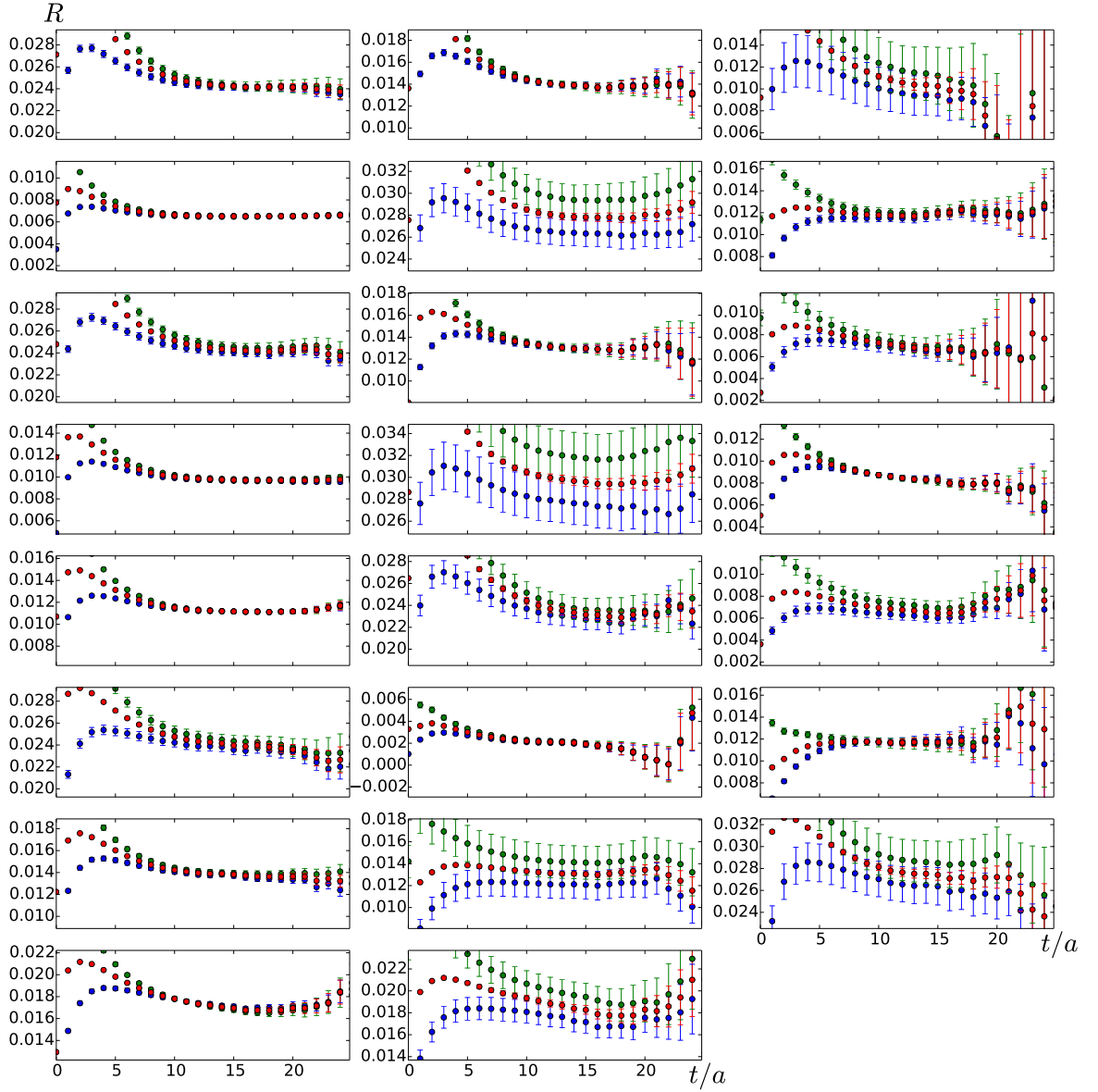


Figure B.12: Same as Figure B.1 but showing the ratios obtained using the pointlike (local) current on F7 and in the window method. Not yet renormalised with Z_V .

Appendix C

Derivatives

For the computation of the timelike pion for factor, using Equation (5.6), the computation of two derivatives is needed. It is possible to compute these derivatives numerically, but in particular the modified zeta-functions in $\phi(q)$ have some very steep sections where it is safer to compute the derivative explicitly.

The easier one of the derivatives is $\frac{\partial}{\partial k}\delta_1(k)$. Using $E_{cm} = 2\sqrt{k^2 + m_\pi^2}$ we can parametrise $\delta_1(k)$ via

$$\delta_1(k) = \operatorname{arccot} \left(\frac{6\pi}{g_{\rho\pi\pi}^2} \frac{(m_\rho^2 - 4(k^2 + m_\pi^2)) \cdot 2\sqrt{k^2 + m_\pi^2}}{k^3} \right). \quad (\text{C.1})$$

Taking the derivative with respect to k yields:

$$\frac{\partial}{\partial k}\delta_1(k) = \frac{2\frac{6\pi}{g_{\rho\pi\pi}^2}k^2}{\sqrt{k^2 + m_\pi^2}} \frac{2k^2(m_\rho^2 - 6m_\pi^2) + 3m_\pi^2(m_\rho^2 - 6m_\pi^2)}{D}, \quad (\text{C.2})$$

with the denominator

$$D = 4 \left(\frac{6\pi}{g_{\rho\pi\pi}^2} \right)^2 \left(16k^6 - 8k^4(m_\rho^2 - 6m_\pi^2) + k^2(m_\rho^4 - 16m_\rho^2 m_\pi^2 + 48m_\pi^4) + m_\pi^2(m_\rho^2 - 4m_\pi^2)^2 \right) + k^6. \quad (\text{C.3})$$

For the other derivative, $\frac{d}{dq}\phi(q)$, we are parametrisng ϕ via

$$\phi(q) = n\pi - \delta_1(k) = n\pi - \operatorname{arccot} \left(\sum_{l,m} \alpha_{lm} w_{lm}(q) \right), \quad (\text{C.4})$$

where we used $q = \frac{Lk}{2\pi}$ and

$$w_{lm}(q) = \frac{1}{\pi^{3/2}\sqrt{2l+1}\gamma} q^{-l-1} Z_{lm}(1, q^2). \quad (\text{C.5})$$

The derivative then is

$$\begin{aligned}\frac{\partial}{\partial q}\phi(q) &= \frac{1}{\left(\sum_{l,m}\alpha_{lm}w_{lm}(q)\right)^2 + 1} \left(\sum_{l,m}\alpha_{lm}\frac{\partial}{\partial q}w_{lm}(q)\right) \\ &= \frac{1}{\cot^2\delta_1(k) + 1} \left(\sum_{l,m}\alpha_{lm}\frac{\partial}{\partial q}w_{lm}(q)\right),\end{aligned}\quad (\text{C.6})$$

with

$$\begin{aligned}\frac{\partial}{\partial q}w_{lm}(q) &= \frac{1}{\pi^{3/2}\sqrt{2l+1}} \cdot \frac{\partial}{\partial q}(\gamma^{-1}q^{-l-1}Z_{lm}(1, q^2)) \\ &= \frac{q^{-l-2}}{\pi^{3/2}\sqrt{2l+1}} \left(\frac{\partial}{\partial q}(\gamma^{-1})qZ_{lm}(1, q^2) - \gamma^{-1}(l+1)Z_{lm}(1, q^2) \right. \\ &\quad \left. + \gamma^{-1}q\frac{\partial}{\partial q}Z_{lm}(1, q^2)\right),\end{aligned}\quad (\text{C.7})$$

and

$$\begin{aligned}\frac{\partial\gamma}{\partial q} &= \frac{\partial}{\partial q}\frac{E}{E_{cm}} \\ &= \frac{\partial}{\partial q}\frac{\sqrt{4\left(\left(\frac{2\pi}{L}\right)^2q^2 + m_\pi^2\right) + P^2}}{2\sqrt{\left(\frac{2\pi}{L}\right)^2q^2 + m_\pi^2}} \\ &= \frac{4\left(\frac{2\pi}{L}\right)^2qP^2}{\gamma E_{cm}^4},\end{aligned}\quad (\text{C.8})$$

$$\frac{\partial}{\partial q}\gamma^{-1} = \frac{-1}{\gamma^2}\frac{\partial\gamma}{\partial q}.\quad (\text{C.9})$$

$Z_{lm}^d(1, q^2)$ has the form [87]

$$Z_{lm}^d(1, q^2) = a + b\delta_{l,0}\delta_{m,0} + c,\quad (\text{C.10})$$

$$a = \gamma \int_0^1 dt e^{tq^2} \sum_{\mathbf{n}\in\mathbb{Z}^3, n\neq 0} e^{i\pi\mathbf{A}\mathbf{n}\cdot\mathbf{d}} (-i)^l \mathcal{Y}_{lm}\left(-\frac{\pi\hat{\gamma}n}{t}\right) \left(\frac{\pi}{t}\right)^{3/2} e^{-\frac{(\pi\hat{\gamma}\mathbf{n})^2}{t}},\quad (\text{C.11})$$

$$b = \frac{\gamma}{\sqrt{4\pi}} \int_0^1 dt (e^{tq^2} - 1) \left(\frac{\pi}{t}\right)^{3/2} - \gamma\pi,\quad (\text{C.12})$$

$$c = \sum_{r\in P_d} \mathcal{Y}_{lm}(r) \frac{e^{-(r^2-q^2)}}{r^2 - q^2}.\quad (\text{C.13})$$

Starting from this expression, $\frac{\partial}{\partial q}(Z_{lm}(1, q^2))$ can be derived via:

$$\frac{\partial}{\partial q}Z_{lm}^d(1, q^2) = \frac{\partial a}{\partial q} + \frac{\partial b}{\partial q}\delta_{l,0}\delta_{m,0} + \frac{\partial c}{\partial q},\quad (\text{C.14})$$

$$\begin{aligned}
\frac{\partial a}{\partial q} &= \gamma \int_0^1 dt 2tq e^{tq^2} \sum_{\mathbf{n} \in \mathcal{Z}^3, \mathbf{n} \neq 0} e^{i\pi \mathbf{A} \mathbf{n} \cdot \mathbf{d}} (-i)^l \mathcal{Y}_{lm} \left(-\frac{\pi \hat{\gamma} \mathbf{n}}{t} \right) \left(\frac{\pi}{t} \right)^{3/2} e^{-\frac{(\pi \hat{\gamma} \mathbf{n})^2}{t}} \\
&+ \frac{\partial \gamma}{\partial q} \int_0^1 dt e^{tq^2} \sum_{\mathbf{n} \in \mathcal{Z}^3, \mathbf{n} \neq 0} e^{i\pi \mathbf{A} \mathbf{n} \cdot \mathbf{d}} (-i)^l \mathcal{Y}_{lm} \left(-\frac{\pi \hat{\gamma} \mathbf{n}}{t} \right) \left(\frac{\pi}{t} \right)^{3/2} e^{-\frac{(\pi \hat{\gamma} \mathbf{n})^2}{t}} \\
&+ \gamma \int_0^1 dt e^{tq^2} \sum_{\mathbf{n} \in \mathcal{Z}^3, \mathbf{n} \neq 0} e^{i\pi \mathbf{A} \mathbf{n} \cdot \mathbf{d}} (-i)^l \frac{\partial}{\partial q} \left[\mathcal{Y}_{lm} \left(-\frac{\pi \hat{\gamma} \mathbf{n}}{t} \right) \right] \left(\frac{\pi}{t} \right)^{3/2} e^{-\frac{(\pi \hat{\gamma} \mathbf{n})^2}{t}} \\
&+ \gamma \int_0^1 dt e^{tq^2} \sum_{\mathbf{n} \in \mathcal{Z}^3, \mathbf{n} \neq 0} e^{i\pi \mathbf{A} \mathbf{n} \cdot \mathbf{d}} (-i)^l \mathcal{Y}_{lm} \left(-\frac{\pi \hat{\gamma} \mathbf{n}}{t} \right) \left(\frac{\pi}{t} \right)^{3/2} \frac{\partial}{\partial q} \left[e^{-\frac{(\pi \hat{\gamma} \mathbf{n})^2}{t}} \right],
\end{aligned} \tag{C.15}$$

$$\begin{aligned}
\frac{\partial b}{\partial q} &= \frac{\gamma}{\sqrt{4\pi}} \int_0^1 dt 2tq e^{tq^2} \left(\frac{\pi}{t} \right)^{3/2} \\
&+ \frac{\partial \gamma}{\partial q} \frac{1}{\sqrt{4\pi}} \int_0^1 dt (e^{tq^2} - 1) \left(\frac{\pi}{t} \right)^{3/2} \\
&- \frac{\partial \gamma}{\partial q} \pi,
\end{aligned} \tag{C.16}$$

$$\begin{aligned}
\frac{\partial c}{\partial q} &= \sum_{r \in P_d} \mathcal{Y}_{lm}(r) \left(2q - r \frac{\partial r}{\partial q} \right) e^{-(r^2 - q^2)} \frac{1 + r^2 - q^2}{(r^2 - q^2)^2} \\
&+ \sum_{r \in P_d} \frac{\partial}{\partial q} [\mathcal{Y}_{lm}(r)] \frac{e^{-(r^2 - q^2)}}{r^2 - q^2},
\end{aligned} \tag{C.17}$$

where

$$\frac{\partial}{\partial q} [\mathcal{Y}_{lm}(\mathbf{r})] = \frac{\partial \mathbf{r}}{\partial q} \cdot \nabla_r \mathcal{Y}_{lm}(\mathbf{r}), \tag{C.18}$$

$$\begin{aligned}
\frac{\partial}{\partial q} \left[e^{-\frac{(\pi \hat{\gamma} \mathbf{n})^2}{t}} \right] &= \frac{\partial}{\partial (\hat{\gamma} \mathbf{n})} \left[e^{-\frac{(\pi \hat{\gamma} \mathbf{n})^2}{t}} \right] \frac{\partial (\hat{\gamma} \mathbf{n})}{\partial q} \\
&= \frac{-2\pi^2 \hat{\gamma} \mathbf{n}}{t} e^{-\frac{(\pi \hat{\gamma} \mathbf{n})^2}{t}} \frac{\partial}{\partial q} (\gamma \mathbf{n}_{\parallel} + \mathbf{n}_{\perp}) \\
&= \frac{-2\pi^2 \hat{\gamma} \mathbf{n}}{t} e^{-\frac{(\pi \hat{\gamma} \mathbf{n})^2}{t}} \mathbf{n}_{\parallel} \frac{\partial \gamma}{\partial q},
\end{aligned} \tag{C.19}$$

$$\mathbf{n} = \mathbf{n}_{\parallel} + \mathbf{n}_{\perp}. \tag{C.20}$$

Appendix D

F_π and a_μ^{hvp} in the fixed- t_0 method

We briefly present here the same plots shown in Chapter 5, but for the fixed- t_0 method.

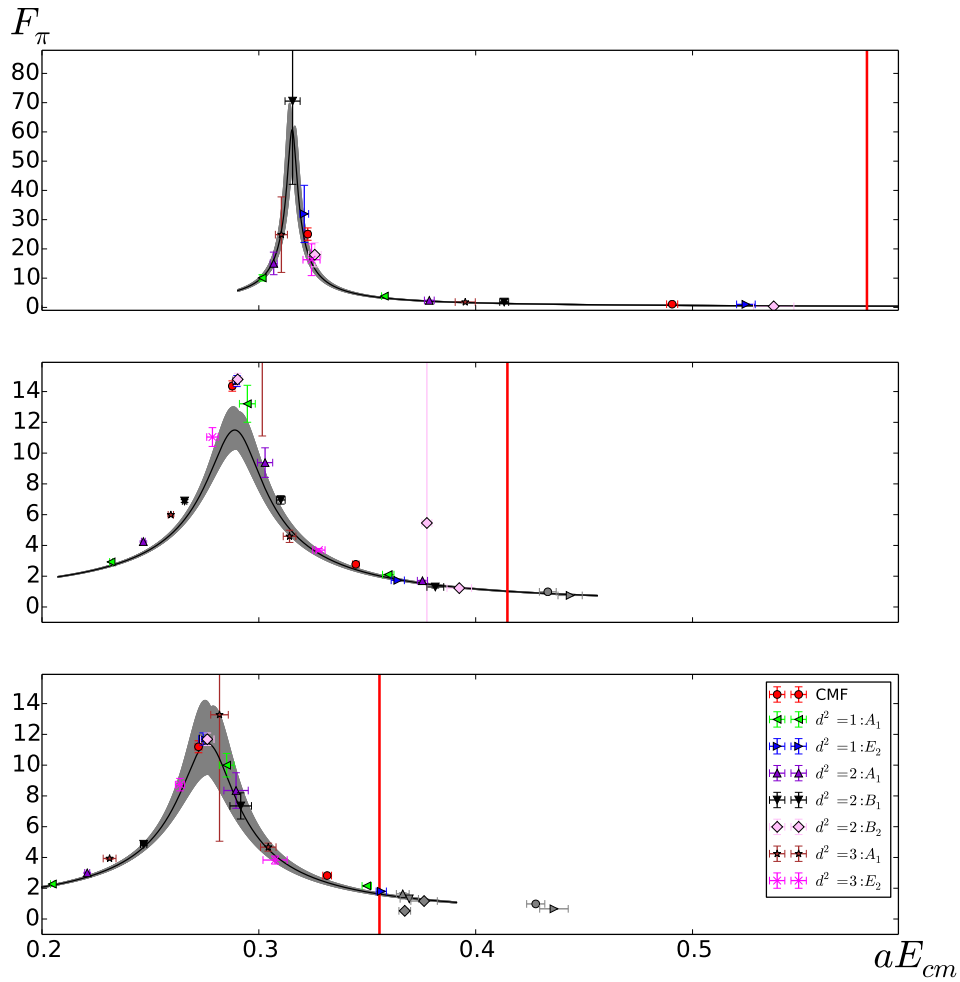


Figure D.1: Same as Figure 5.1 but using the fixed- t_0 method.

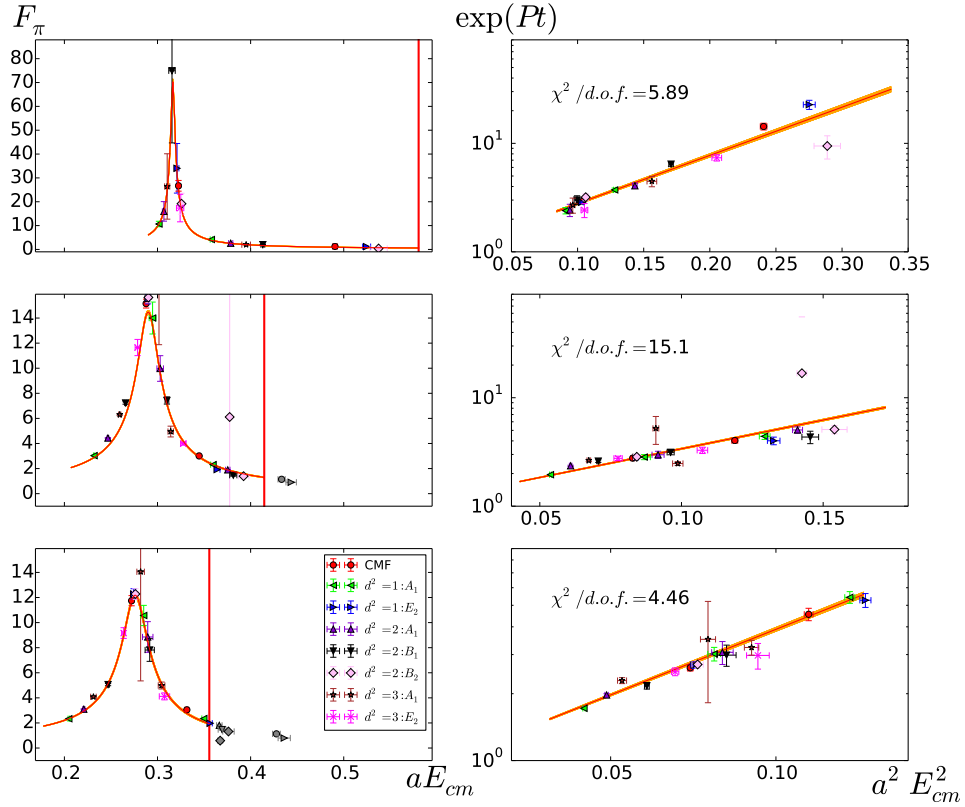


Figure D.2: Same as Figure 5.2 but using the fixed- t_0 method. The extremely large $\chi^2 / \text{d.o.f.}$ value on F6 comes from the tension of the two ground states, mostly from the $\mathbf{d}^2 = 1, A_1$ and $\mathbf{d}^2 = 2, A_1$ irreps. Removing the first one reduced the $\chi^2 / \text{d.o.f.}$ to 11 and removing the latter one reduces it to 10.

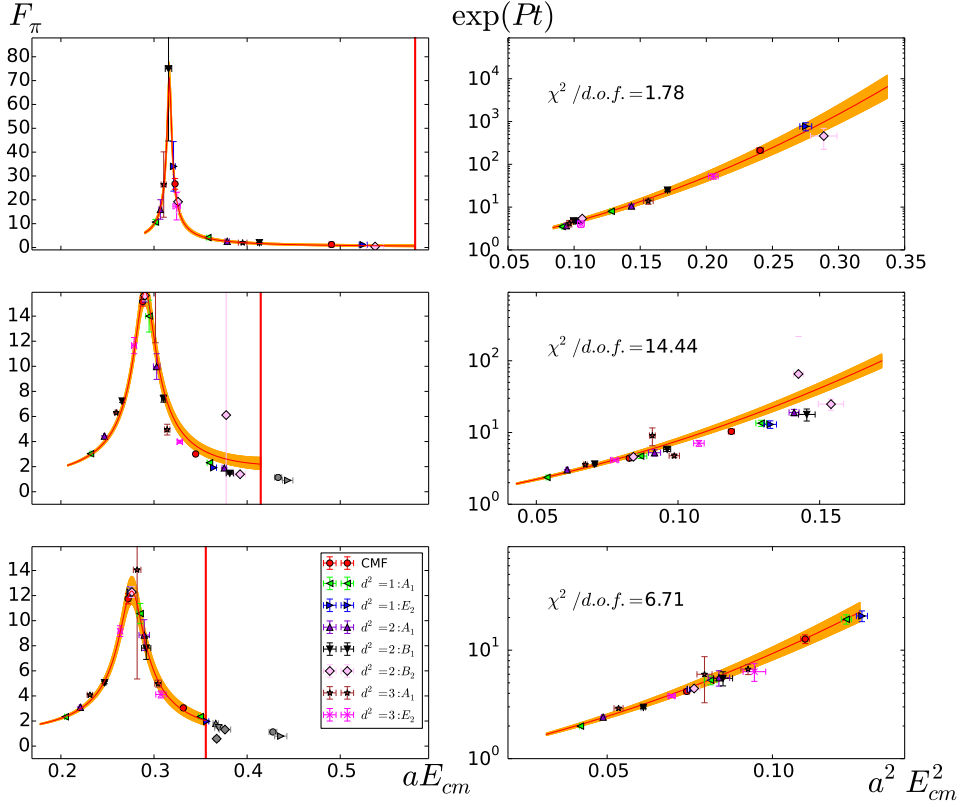


Figure D.3: Same as Figure 5.3 but using the fixed- t_0 method. The extremely large $\chi^2 / \text{d.o.f.}$ value on F6 comes from the tension of the two ground states, mostly from the $\mathbf{d}^2 = 1, A_1$ and $\mathbf{d}^2 = 2, A_1$ irreps. Removing the first one reduced the $\chi^2 / \text{d.o.f.}$ to 7 and removing the latter one reduces it to 9.

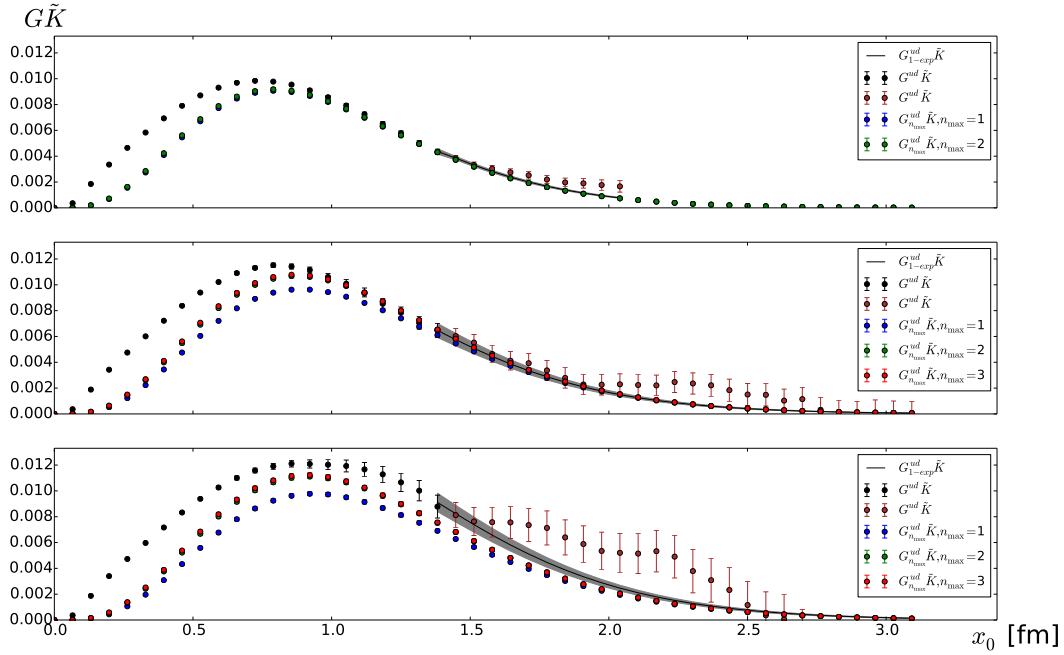


Figure D.4: Same as Figure 5.5 but using the fixed- t_0 method.

d^2	irrep	E5		F6		F7	
		$ A_\psi $	F_π	$ A_\psi $	F_π	$ A_\psi $	F_π
0	T_1	0.0214(32)	23.53(1.99)	0.0178(22)	13.61(32)	0.0162(26)	10.67(37)
		0.0061(18)	0.97(4)	0.0082(13)	2.56(3)	0.0088(15)	2.62(4)
1	A_1	0.0183(24)	9.55(1.01)	0.0053(5)	2.83(3)	0.0047(6)	2.21(3)
		0.0153(22)	3.56(4)	0.0191(40)	12.46(1.13)	0.0186(36)	9.46(72)
1	E_2	0.0198(34)	30.03(9.19)	0.0177(22)	13.90(34)	0.0163(28)	11.14(38)
		0.0072(23)	0.92(4)	0.0064(13)	1.57(3)	0.0069(13)	1.64(3)
2	A_1	0.0220(33)	14.17(3.64)	0.0085(9)	4.08(4)	0.0070(10)	2.91(3)
		0.0119(22)	2.19(3)	0.0193(38)	8.82(90)	0.0191(46)	7.88(1.09)
2	B_1	0.0182(40)	66.38(26.76)	0.0102(12)	6.56(9)	0.0082(12)	4.67(9)
		0.0081(15)	1.66(3)	0.0149(22)	6.51(25)	0.0147(33)	6.91(80)
2	B_2	0.0195(41)	16.91(3.89)	0.0173(25)	13.99(37)	0.0159(32)	11.12(39)
		0.0028(11)	0.32(3)	0.0023(5)	4.87(11.06)	0.0019(5)	0.48(11)
3	A_1	0.0249(48)	23.42(12.16)	0.0123(14)	5.70(7)	0.0097(19)	3.79(7)
		0.0097(22)	1.65(3)	0.0133(18)	16.40(6.00)	0.0110(22)	12.54(7.77)
3	E_1	0.0130(32)	15.31(5.11)	0.0121(21)	4.26(37)	0.0154(30)	4.38(24)
		0.0056(13)	0.94(2)	0.0138(22)	10.47(58)	0.0124(18)	8.32(39)
				0.0108(18)	3.43(10)	0.0107(25)	3.57(24)

Table D.1: Same as Table 5.1 but using the fixed- t_0 method.

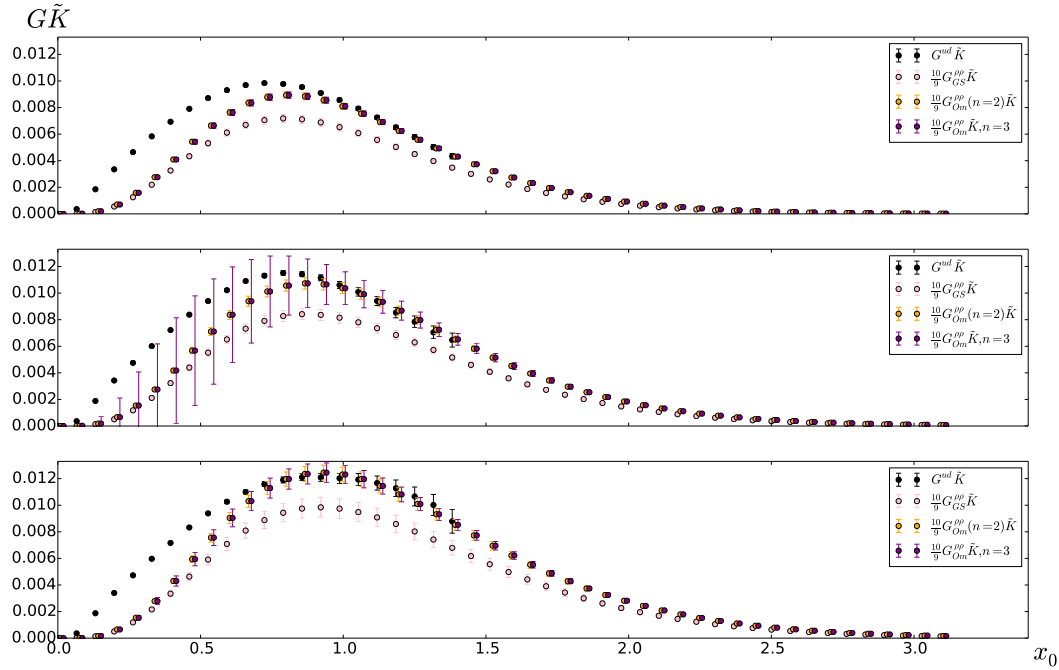


Figure D.5: Same as Figure 5.6 but using the fixed- t_0 method.

	E5	F6	F7
0 to x_0^{cut}	2.662(26)	3.131(52)	3.462(86)
x_0^{cut} to ∞ (1-exp/GS)	0.482(15)	0.818(52)	1.238(96)
x_0^{cut} to ∞ (G^{ud})	0.467(9)	0.839(16)	1.058(35)
x_0^{cut} to ∞ ($G^{\rho\rho}, n=2$)	0.476(15)	0.849(30)	1.234(56)
x_0^{cut} to ∞ ($G^{\rho\rho}, n=3$)	0.487(13)	1.027(45)	1.269(50)
0 to ∞ (1-exp/GS)	3.145(39)	3.949(99)	4.700(173)
0 to ∞ (G^{ud})	3.130(28)	3.970(59)	4.530(99)
0 to ∞ ($G^{\rho\rho}, n=2$)	3.138(31)	3.980(64)	4.696(105)
0 to ∞ ($G^{\rho\rho}, n=3$)	3.149(30)	4.158(74)	4.731(105)

Table D.2: Same as Table 5.4 but using the fixed- t_0 method.

n	E5	F6	F7
$\langle r^2 \rangle / r_0^2$ 2	1.14(2)	1.36(1)	1.51(2)
$\langle r^2 \rangle / r_0^2$ 3	1.15(5)	1.26(4)	1.48(5)
c_V / r_0^4 3	3.45(8)	5.15(8)	3.21(7)

Table D.3: Same as Table 5.2 but using the fixed- t_0 method.

n	E5	F6	F7
$\langle r^2 \rangle / r_0^2$ 2	1.20(2)	1.43(1)	1.59(2)
$\langle r^2 \rangle / r_0^2$ 3	1.23(5)	1.32(4)	1.55(5)
c_V / r_0^4 3	3.68(9)	5.43(7)	3.53(8)
$\langle r^2 \rangle / r_0^2$	1.18(5)	1.37(6)	1.61(10)

Table D.4: Same as Table 5.3 but using the fixed- t_0 method.

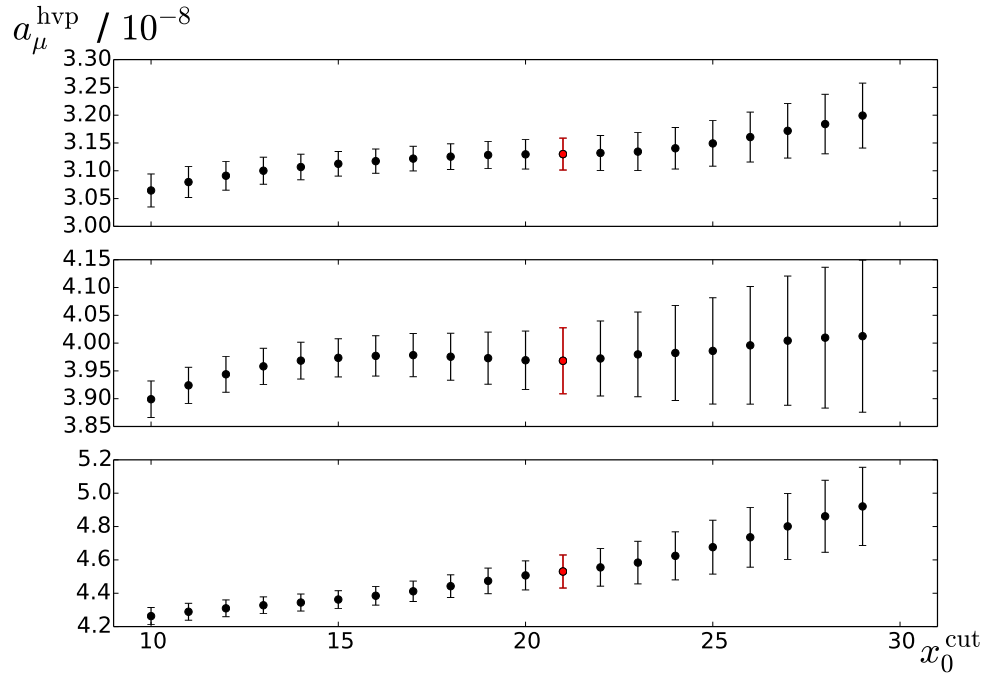


Figure D.6: Same as Figure 5.7 but using the fixed- t_0 method.

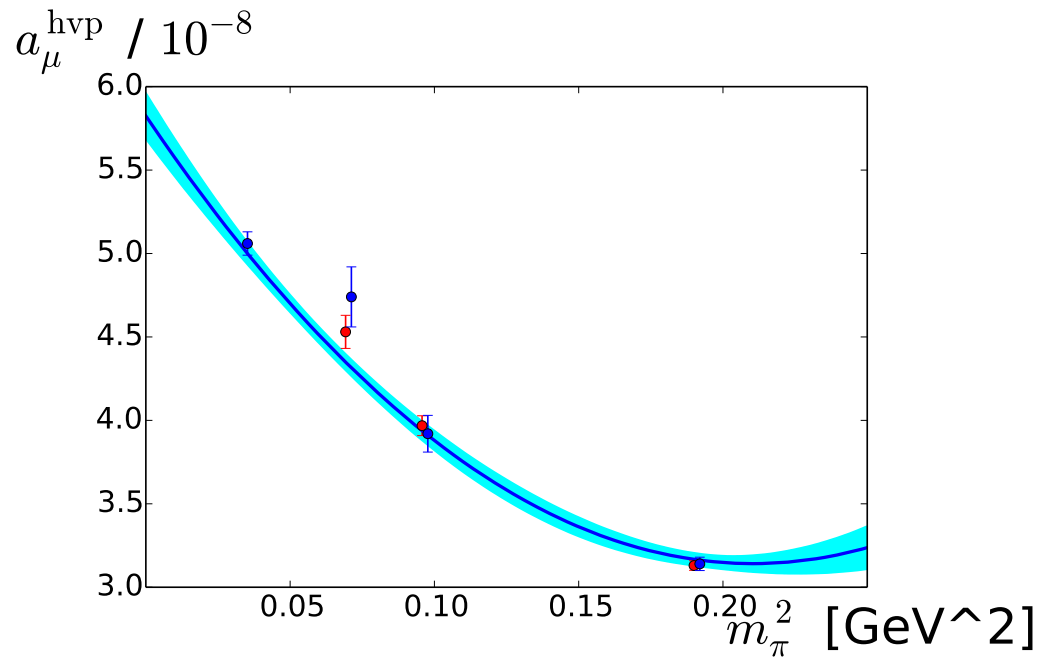


Figure D.7: Same as Figure 5.8 but using the fixed- t_0 method.

Appendix E

Next steps

E.1 Computation on a more chiral ensemble

It would be a logical next step of this work to perform the full analysis on the CLS ensemble G8, which shares the lattice spacing with all ensembles used in this work but has a lower pion mass. The G8 value for a_μ^{hvp} , computed in [92], was already shown in Figure 5.8. With a pion mass of $m_\pi = 185$ MeV and a lattice extent of $T \cdot L^3 = 128 \cdot 64^3$ this would cost a significant amount of computer time and we would have to tweak the code we used for this work due to the additional demand of memory required. When aiming for the same number of eigenmodes per physical volume, $N_{\text{ev}} = 464$ would have to be used. With a Laplace-interlaced dilution of 16 and a time-interlacing of 8, the current version of the production code can fit the required memory on the HPC Cluster 'Clover' only if 128 nodes with 16 processors (with a memory of 2GB per core) each are used, and takes $\sim 500s$ for the eigenvector computation, $\sim 500s$ per source timeslice for the perambulators used to build quark lines connected to the source timeslice and $\sim 1000s$ for the perambulators used for the sink-to-sink lines. If one wanted to compute perambulators on four source timeslices, this would amount to a total cost of about 2000 core-hours per configuration, of which there are 349 currently stored on Clover. This would be everything that is needed to extract the energy spectrum as well as the phase-shift information on G8. The real challenge though would be to compute the meson-sink functions, which are needed to compute the current elements used for the determination of the timelike pion form factor and the hadronic vacuum polarisation to $(g-2)_\mu$. The way the code is currently written, the perambulators (from which the pointlike sinks are computed) are stored in memory and then the pointlike sinks are computed in a loop over all lattice sites and momenta, with a subsequent Fourier transform acting on the object. This barely fits into Clover's memory and in order to compute the pointlike sinks efficiently, it would be desirable to fully reorganise the code so that the meson sinks are computed at the same time as the perambulators, so that memory can be released in the process, at

the cost of re-computing some objects. It would also be strongly desirable to have implement a Fast-Fourier Transform to speed up the computation.

E.2 Analysis for more chiral ensembles

It is already visible on F6 and F7 that the $4m_\pi$ threshold approaches the resonance region. Ensembles which are closer to the physical pion mass, where $m_\pi \approx 140$ MeV and $m_\rho \approx 770$ MeV will certainly suffer from this and it remains to be seen how well we will be able to resolve the phase shift $\delta(k)$ or the pion form factor F_π on more chiral ensembles. To get an idea of the uncertainty introduced by having only the lowest levels of the spectrum below the $4m_\pi$ threshold and thus available for a Lüscher analysis, we are comparing the fit results to the phase shift when only taking into account the lowest states on each lattice. The results are shown for the window-method in Table E.1 and for the fixed- t_0 method in Table E.2. We can clearly see from this that the

	E5		F6		F7	
levels:	all	gs only	all	gs only	all	gs only
m_ρ	0.3156(8)	0.3147(9)	0.2933(8)	0.2923(10)	0.2800(11)	0.2786(13)
$g_{\rho\pi\pi}$	5.70(9)	5.84(18)	6.08(13)	6.32(25)	5.90(21)	5.41(73)
χ^2/dof	1.47	1.02	0.75	0.97	1.57	1.47

Table E.1: Resonance parameters extracted from the fit to the energy levels using the Lüscher formalism. All levels are extracted using the window method with $t_w=3$, as described in Section 4.2.2. Compared are the fit results to all levels below the $4m_\pi$ threshold ('all') and fits only to the ground states of the spectrum ('gs only'). On a more chiral lattice like G8, the $4m_\pi$ threshold moves closer to the lower lying states of the spectrum and one would have to fit only to those parts, because the Lüscher theory only applies there.

	E5		F6		F7	
levels:	all	gs only	all	gs only	all	gs only
m_ρ	0.3168(9)	0.3157(12)	0.2923(12)	0.2919(13)	0.2784(17)	0.2786(19)
$g_{\rho\pi\pi}$	5.86(11)	6.12(22)	5.95(16)	6.32(37)	5.71(20)	5.56(58)
χ^2/dof	1.28	1.07	1.27	0.90	1.64	1.46

Table E.2: Same as Table E.1 but for the fixed- t_0 method.

error estimate on the result blows up, but that we still get an overall agreement within errors between the two determinations. In practice, the situation will not be quite as bad, because on a more chiral ensemble with a similar value of $m_\pi L$, there will be more levels available in the low-energy region, because the number of two-pion energy levels between $2m_\pi$ and $4m_\pi$ is the same on lattices which share the same $m_\pi L$.

Bibliography

- [1] M. Lüscher. Volume Dependence of the Energy Spectrum in Massive Quantum Field Theories. 1. Stable Particle States. *Commun. Math. Phys.*, 104:177, 1986.
- [2] M. Lüscher. Volume Dependence of the Energy Spectrum in Massive Quantum Field Theories. 2. Scattering States. *Commun. Math. Phys.*, 105:153–188, 1986.
- [3] Harvey B. Meyer. Lattice qcd and the timelike pion form factor. *Phys. Rev. Lett.*, 107:072002, Aug 2011.
- [4] Fred Jegerlehner and Andreas Nyffeler. The Muon $g-2$. *Phys. Rept.*, 477:1–110, 2009.
- [5] Particle Data Group C. Patrignani et al. Review of particle physics. *Chinese Physics C*, 40(10):100001, 2016.
- [6] S. Aoki et al. Lattice QCD Calculation of the rho Meson Decay Width. *Phys. Rev.*, D76:094506, 2007.
- [7] S. Aoki et al. ρ Meson Decay in 2+1 Flavor Lattice QCD. *Phys. Rev.*, D84:094505, 2011.
- [8] Xu Feng, Karl Jansen, and Dru B. Renner. Resonance Parameters of the rho-Meson from Lattice QCD. *Phys. Rev.*, D83:094505, 2011.
- [9] C. B. Lang, Daniel Mohler, Sasa Prelovsek, and Matija Vidmar. Coupled channel analysis of the rho meson decay in lattice QCD. *Phys. Rev.*, D84(5):054503, 2011. [Erratum: *Phys. Rev.* D89,no.5,059903(2014)].
- [10] Craig Pelissier and Andrei Alexandru. Resonance parameters of the rho-meson from asymmetrical lattices. *Phys. Rev.*, D87(1):014503, 2013.
- [11] Jozef J. Dudek, Robert G. Edwards, and Christopher E. Thomas. Energy dependence of the ρ resonance in $\pi\pi$ elastic scattering from lattice QCD. *Phys. Rev.*, D87(3):034505, 2013. [Erratum: *Phys. Rev.* D90,no.9,099902(2014)].

- [12] David J. Wilson, Raúl A. Briceño, Jozef J. Dudek, Robert G. Edwards, and Christopher E. Thomas. Coupled $\pi\pi, K\bar{K}$ scattering in P -wave and the ρ resonance from lattice QCD. *Phys. Rev.*, D92(9):094502, 2015.
- [13] Gunnar S. Bali, Sara Collins, Antonio Cox, Gordon Donald, Meinulf Göckeler, C. B. Lang, and Andreas Schäfer. ρ and K^* resonances on the lattice at nearly physical quark masses and $N_f = 2$. *Phys. Rev.*, D93(5):054509, 2016.
- [14] John Bulava, Brendan Fahy, Ben Hörz, Keisuke J. Juge, Colin Morningstar, and Chik Him Wong. $I = 1$ and $I = 2$ $\pi - \pi$ scattering phase shifts from $N_f = 2 + 1$ lattice QCD. *Nucl. Phys.*, B910:842–867, 2016.
- [15] Raúl A. Briceño, Jozef J. Dudek, and Ross D. Young. Scattering processes and resonances from lattice QCD. *Rev. Mod. Phys.*, 90(2):025001, 2018.
- [16] Michael Peardon, John Bulava, Justin Foley, Colin Morningstar, Jozef Dudek, Robert G. Edwards, Balint Joo, Huey-Wen Lin, David G. Richards, and Keisuke Jimmy Juge. A Novel quark-field creation operator construction for hadronic physics in lattice QCD. *Phys. Rev.*, D80:054506, 2009.
- [17] C. Morningstar, J. Bulava, J. Foley, K. J. Juge, D. Lenkner, M. Peardon, and C. H. Wong. Improved stochastic estimation of quark propagation with laplacian heaviside smearing in lattice qcd. *Phys. Rev. D*, 83:114505, Jun 2011.
- [18] I. Montvay and G. Münster. *Quarks, gluons and lattices*. Cambridge Univ. Press, 1997.
- [19] Paul A. M. Dirac. The Lagrangian in quantum mechanics. *Phys. Z. Sowjetunion*, 3:64–72, 1933.
- [20] R. P. Feynman. Space-time approach to non-relativistic quantum mechanics. *Rev. Mod. Phys.*, 20:367–387, Apr 1948.
- [21] David J. Gross and Frank Wilczek. Ultraviolet behavior of non-abelian gauge theories. *Phys. Rev. Lett.*, 30:1343–1346, Jun 1973.
- [22] LHCb Collaboration. Observation of $j/\psi p$ resonances consistent with pentaquark states in $\Lambda_b^0 \rightarrow j/\psi K^- p$ decays. *Phys. Rev. Lett.*, 115:072001, Aug 2015.
- [23] LHCb Collaboration. Observation of $j/\psi\phi$ structures consistent with exotic states from amplitude analysis of $B^+ \rightarrow j/\psi\phi K^+$ decays. *Phys. Rev. Lett.*, 118:022003, Jan 2017.

- [24] G. C. Wick. Properties of bethe-salpeter wave functions. *Phys. Rev.*, 96:1124–1134, Nov 1954.
- [25] F. J. Dyson. The s matrix in quantum electrodynamics. *Phys. Rev.*, 75:1736–1755, Jun 1949.
- [26] Julian Schwinger. On the euclidean structure of relativistic field theory. *Proceedings of the National Academy of Sciences*, 44(9):956–965, 1958.
- [27] K. Symanzik. Euclidean quantum field theory. i. equations for a scalar model. *Journal of Mathematical Physics*, 7(3):510–525, 1966.
- [28] Christof Gattringer and Christian B. Lang. *Quantum Chromodynamics on the Lattice*. Springer-Verlag Berlin, 2010.
- [29] M. Creutz. *Quarks, gluons and lattices*. Cambridge Univ. Press, 1985.
- [30] H. Wittig. *QCD on the lattice*. Springer-Verlag Berlin, 2008.
- [31] H.B. Nielsen and M. Ninomiya. Absence of neutrinos on a lattice: (i). proof by homotopy theory. *Nuclear Physics B*, 185(1):20 – 40, 1981.
- [32] H.B. Nielsen and M. Ninomiya. A no-go theorem for regularizing chiral fermions. *Physics Letters B*, 105(2):219 – 223, 1981.
- [33] H.B. Nielsen and M. Ninomiya. Absence of neutrinos on a lattice: (ii). intuitive topological proof. *Nuclear Physics B*, 193(1):173 – 194, 1981.
- [34] Kenneth G. Wilson. Confinement of quarks. *Phys. Rev. D*, 10:2445–2459, Oct 1974.
- [35] John Kogut and Leonard Susskind. Hamiltonian formulation of wilson’s lattice gauge theories. *Phys. Rev. D*, 11:395–408, Jan 1975.
- [36] Claude Bernard, Maarten Golterman, and Yigal Shamir. Observations on staggered fermions at non-zero lattice spacing. *Phys. Rev.*, D73:114511, 2006.
- [37] Roberto Frezzotti, Pietro Antonio Grassi, Stefan Sint, and Peter Weisz. A local formulation of lattice qcd without unphysical fermion zero modes. *Nuclear Physics B - Proceedings Supplements*, 83-84:941 – 946, 2000. Proceedings of the XVIIth International Symposium on Lattice Field Theory.
- [38] ALPHA Collaboration, Roberto Frezzotti, Pietro Antonio Grassi, Stefan Sint, and Peter Weisz. Lattice qcd with a chirally twisted mass term. *Journal of High Energy Physics*, 2001(08):058, 2001.

- [39] Roberto Frezzotti, Stefan Sint, and Peter Weisz. $O(a)$ improved twisted mass lattice qcd. *Journal of High Energy Physics*, 2001(07):048, 2001.
- [40] Paul H. Ginsparg and Kenneth G. Wilson. A remnant of chiral symmetry on the lattice. *Phys. Rev. D*, 25:2649–2657, May 1982.
- [41] David B. Kaplan. A method for simulating chiral fermions on the lattice. *Physics Letters B*, 288(3):342 – 347, 1992.
- [42] K. Symanzik. Continuum limit and improved action in lattice theories: (i). principles and 4 theory. *Nuclear Physics B*, 226(1):187 – 204, 1983.
- [43] K. Symanzik. Continuum limit and improved action in lattice theories: (ii). $o(n)$ non-linear sigma model in perturbation theory. *Nuclear Physics B*, 226(1):205 – 227, 1983.
- [44] B. Sheikholeslami and R. Wohlert. Improved continuum limit lattice action for qcd with wilson fermions. *Nuclear Physics B*, 259(4):572 – 596, 1985.
- [45] Francesco Knechtli, Tomasz Korzec, Björn Leder, and Graham Moir. Power corrections from decoupling of the charm quark. *Phys. Lett.*, B774:649–655, 2017.
- [46] Francesco Knechtli, Tomasz Korzec, Björn Leder, and Graham Moir. Decoupling of charm beyond leading order. *EPJ Web Conf.*, 175:10001, 2018.
- [47] B. Hu, R. Molina, M. Döring, and A. Alexandru. Two-flavor Simulations of the $\rho(770)$ and the Role of the $K\bar{K}$ Channel. *Phys. Rev. Lett.*, 117(12):122001, 2016.
- [48] Simon Duane, A.D. Kennedy, Brian J. Pendleton, and Duncan Roweth. Hybrid monte carlo. *Physics Letters B*, 195(2):216 – 222, 1987.
- [49] Martin Lüscher. Schwarz-preconditioned hmc algorithm for two-flavor lattice qcd. *Computer Physics Communications*, 165(3):199 – 220, 2005.
- [50] Martin Lüscher. Deflation acceleration of lattice qcd simulations. *Journal of High Energy Physics*, 2007(12):011, 2007.
- [51] Martin Hasenbusch. Speeding up the hybrid Monte Carlo algorithm for dynamical fermions. *Phys. Lett.*, B519:177–182, 2001.
- [52] Marina Marinkovic and Stefan Schaefer. Comparison of the mass preconditioned HMC and the DD-HMC algorithm for two-flavour QCD. *PoS, LATTICE2010:031*, 2010.

- [53] Patrick Fritzsche, Francesco Knechtli, Bjorn Leder, Marina Marinkovic, Stefan Schaefer, Rainer Sommer, and Francesco Virota. The strange quark mass and Lambda parameter of two flavor QCD. *Nucl. Phys.*, B865:397–429, 2012.
- [54] S. Capitani, M. Della Morte, D. Djukanovic, G. von Hippel, J. Hua, B. Jäger, B. Knippschild, H. B. Meyer, T. D. Rae, and H. Wittig. Nucleon electromagnetic form factors in two-flavor QCD. *Phys. Rev.*, D92(5):054511, 2015.
- [55] Karl Jansen and Rainer Sommer. $O(\alpha)$ improvement of lattice QCD with two flavors of Wilson quarks. *Nucl. Phys.*, B530:185–203, 1998. [Erratum: *Nucl. Phys.* B643,517(2002)].
- [56] Ulli Wolff. Monte Carlo errors with less errors. *Comput. Phys. Commun.*, 156:143–153, 2004. [Erratum: *Comput. Phys. Commun.* 176,383(2007)].
- [57] R. Sommer. A New way to set the energy scale in lattice gauge theories and its applications to the static force and alpha-s in SU(2) Yang-Mills theory. *Nucl. Phys.*, B411:839–854, 1994.
- [58] Patrick Fritzsche, Francesco Knechtli, Bjorn Leder, Marina Marinkovic, Stefan Schaefer, Rainer Sommer, and Francesco Virota. The strange quark mass and Lambda parameter of two flavor QCD. *Nucl. Phys.*, B865:397–429, 2012.
- [59] M. H. Quenouille. Notes on bias in estimation. *Biometrika*, 43(3-4):353–360, 1956.
- [60] J. W. Tukey. Bias and confidence in not quite large samples. *Annl. Math. Stat.*, 29, 1958.
- [61] C. Michael and I. Teasdale. Extracting glueball masses from lattice qcd. *Nuclear Physics B*, 215(3):433 – 446, 1983.
- [62] Christopher Michael. Adjoint Sources in Lattice Gauge Theory. *Nucl. Phys.*, B259:58–76, 1985.
- [63] Martin Lüscher and Ulli Wolff. How to Calculate the Elastic Scattering Matrix in Two-dimensional Quantum Field Theories by Numerical Simulation. *Nucl. Phys.*, B339:222–252, 1990.
- [64] Benoit Blossier, Michele Della Morte, Georg von Hippel, Tereza Mendes, and Rainer Sommer. On the generalized eigenvalue method for energies and matrix elements in lattice field theory. *JHEP*, 04:094, 2009.

- [65] M. Albanese et al. Glueball Masses and String Tension in Lattice QCD. *Phys. Lett.*, B192:163–169, 1987.
- [66] Colin Morningstar and Mike Peardon. Analytic smearing of SU(3) link variables in lattice qcd. *Phys. Rev. D*, 69:054501, Mar 2004.
- [67] Anna Hasenfratz and Francesco Knechtli. Flavor symmetry and the static potential with hypercubic blocking. *Phys. Rev.*, D64:034504, 2001.
- [68] Justin Foley, K. Jimmy Juge, Alan Cais, Mike Peardon, Sinad M. Ryan, and Jon-Ivar Skullerud. Practical all-to-all propagators for lattice qcd. *Computer Physics Communications*, 172(3):145 – 162, 2005.
- [69] Walter Wilcox. Noise methods for flavor singlet quantities. In *Numerical challenges in lattice quantum chromodynamics. Proceedings, Joint Interdisciplinary Workshop, Wuppertal, Germany, August 22-24, 1999*, pages 127–141, 1999.
- [70] M. Ablikim et al. Measurement of the $e^+e^- \rightarrow \pi^+\pi^-$ cross section between 600 and 900 MeV using initial state radiation. *Phys. Lett.*, B753:629–638, 2016.
- [71] Xu Feng, Karl Jansen, and Dru B. Renner. Resonance parameters of the ρ meson from lattice qcd. *Phys. Rev. D*, 83:094505, May 2011.
- [72] Martin Luscher, Stefan Sint, Rainer Sommer, and Peter Weisz. Chiral symmetry and $O(a)$ improvement in lattice QCD. *Nucl. Phys.*, B478:365–400, 1996.
- [73] Martin Luscher, Stefan Sint, Rainer Sommer, and Hartmut Wittig. Non-perturbative determination of the axial current normalization constant in $O(a)$ improved lattice QCD. *Nucl. Phys.*, B491:344–364, 1997.
- [74] Jozef J. Dudek, Robert G. Edwards, Michael J. Peardon, David G. Richards, and Christopher E. Thomas. Toward the excited meson spectrum of dynamical qcd. *Phys. Rev. D*, 82:034508, Aug 2010.
- [75] Jozef J. Dudek, Robert G. Edwards, and Christopher E. Thomas. *s*. *Phys. Rev. D*, 86:034031, Aug 2012.
- [76] David C. Moore and George T. Fleming. Angular momentum on the lattice: The case of nonzero linear momentum. *Phys. Rev. D*, 73:014504, Jan 2006.
- [77] Eugen Wigner. Gruppentheorie und ihre anwendung auf die quantenmechanik der atomspektren. 1931.

- [78] Christopher E. Thomas, Robert G. Edwards, and Jozef J. Dudek. Helicity operators for mesons in flight on the lattice. *Phys. Rev. D*, 85:014507, Jan 2012.
- [79] Jozef J. Dudek, Robert G. Edwards, and Christopher E. Thomas. Energy dependence of the ρ resonance in $\pi\pi$ elastic scattering from lattice qcd. *Phys. Rev. D*, 87:034505, Feb 2013.
- [80] C. Morningstar, J. Bulava, B. Fahy, J. Foley, Y. C. Jhang, K. J. Juge, D. Lenkner, and C. H. Wong. Extended hadron and two-hadron operators of definite momentum for spectrum calculations in lattice QCD. *Phys. Rev.*, D88(1):014511, 2013.
- [81] Konrad Osterwalder and Robert Schrader. Axioms for euclidean green’s functions. *Communications in Mathematical Physics*, 31(2):83–112, Jun 1973.
- [82] L. Maiani and M. Testa. Final state interactions from euclidean correlation functions. *Physics Letters B*, 245(3):585 – 590, 1990.
- [83] Laurent Lellouch and Martin Lüscher. Weak transition matrix elements from finite-volume correlation functions. *Communications in Mathematical Physics*, 219(1):31–44, May 2001.
- [84] K. Rummukainen and Steven A. Gottlieb. Resonance scattering phase shifts on a nonrest frame lattice. *Nucl. Phys.*, B450:397–436, 1995.
- [85] C. h. Kim, C. T. Sachrajda, and Stephen R. Sharpe. Finite-volume effects for two-hadron states in moving frames. *Nucl. Phys.*, B727:218–243, 2005.
- [86] Raúl A. Briceño and Maxwell T. Hansen. Multichannel $0 \rightarrow 2$ and $1 \rightarrow 2$ transition amplitudes for arbitrary spin particles in a finite volume. *Phys. Rev.*, D92(7):074509, 2015.
- [87] Luka Leskovec and Sasa Prelovsek. Scattering phase shifts for two particles of different mass and nonzero total momentum in lattice qcd. *Phys. Rev. D*, 85:114507, Jun 2012.
- [88] Xu Feng, Karl Jansen, and Dru B. Renner. A new moving frame to extract scattering phases in lattice QCD. *PoS*, LATTICE2010:104, 2010.
- [89] Colin Morningstar, John Bulava, Bijit Singha, Ruair Brett, Jacob Fallica, Andrew Hanlon, and Ben Hörz. Estimating the two-particle K -matrix for multiple partial waves and decay channels from finite-volume energies. *Nucl. Phys.*, B924:477–507, 2017.

- [90] T. Yamazaki et al. $I = 2$ $\pi\pi$ scattering phase shift with two flavors of $O(a)$ improved dynamical quarks. *Phys. Rev.*, D70:074513, 2004.
- [91] G. J. Gounaris and J. J. Sakurai. Finite-width corrections to the vector-meson-dominance prediction for $\rho \rightarrow e^+e^-$. *Phys. Rev. Lett.*, 21:244–247, Jul 1968.
- [92] M. Della Morte, A. Francis, V. Gülpers, G. Herdoíza, G. von Hippel, H. Horch, B. Jäger, H.B. Meyer, A. Nyffeler, and H. Wittig. The hadronic vacuum polarization contribution to the muon $g - 2$ from lattice qcd. *Journal of High Energy Physics*, 2017(10):20, Oct 2017.
- [93] John Bulava, Ben Hörz, Brendan Fahy, K. J. Juge, Colin Morningstar, and Chik Him Wong. Pion-pion scattering and the timelike pion form factor from $N_f = 2 + 1$ lattice QCD simulations using the stochastic LapH method. *PoS, LATTICE2015:069*, 2016.
- [94] D. Brommel et al. The Pion form-factor from lattice QCD with two dynamical flavours. *Eur. Phys. J.*, C51:335–345, 2007.
- [95] P. A. Boyle, J. M. Flynn, A. Jüttner, C. Kelly, H. Pedroso de Lima, C. M. Maynard, C. T. Sachrajda, and J. M. Zanotti. The Pion’s electromagnetic form-factor at small momentum transfer in full lattice QCD. *JHEP*, 07:112, 2008.
- [96] R. Frezzotti, V. Lubicz, and S. Simula. Electromagnetic form factor of the pion from twisted-mass lattice QCD at $N(f) = 2$. *Phys. Rev.*, D79:074506, 2009.
- [97] S. Aoki et al. Pion form factors from two-flavor lattice QCD with exact chiral symmetry. *Phys. Rev.*, D80:034508, 2009.
- [98] Oanh Hoang Nguyen, Ken-Ichi Ishikawa, Akira Ukawa, and Naoya Ukita. Electromagnetic form factor of pion from $N_f = 2 + 1$ dynamical flavor QCD. *JHEP*, 04:122, 2011.
- [99] Bastian B. Brandt, Andreas Jüttner, and Hartmut Wittig. Calculation of the pion electromagnetic form factor from lattice QCD. In *Proceedings, 14th International Conference on Hadron spectroscopy (Hadron 2011): Munich, Germany, June 13-17, 2011*, 2011.
- [100] Bastian B. Brandt, Andreas Jüttner, and Hartmut Wittig. The pion vector form factor from lattice QCD and NNLO chiral perturbation theory. *JHEP*, 11:034, 2013.
- [101] Xu Feng, Sinya Aoki, Shoji Hashimoto, and Takashi Kaneko. Timelike pion form factor in lattice qcd. *Phys. Rev. D*, 91:054504, Mar 2015.

- [102] Anthony Francis, Benjamin Jäger, Harvey B. Meyer, and Hartmut Wittig. A new representation of the Adler function for lattice QCD. *Phys. Rev.*, D88:054502, 2013.
- [103] Feng-Kun Guo, Christoph Hanhart, Felipe J. Llanes-Estrada, and Ulf-G. Meissner. Quark mass dependence of the pion vector form factor. *Phys. Lett.*, B678:90–96, 2009.
- [104] Francisco Guerrero. Study of the resummation of chiral logarithms in the exponentiated expression for the pion form-factor. *Phys. Rev.*, D57:4136–4141, 1998.
- [105] The quantum theory of the electron. *Proceedings of the Royal Society of London A: Mathematical, Physical and Engineering Sciences*, 117(778):610–624, 1928.
- [106] The quantum theory of the electron. part ii. *Proceedings of the Royal Society of London A: Mathematical, Physical and Engineering Sciences*, 118(779):351–361, 1928.
- [107] C. Gnendiger, D. Stöckinger, and H. Stöckinger-Kim. The electroweak contributions to $(g-2)_\mu$ after the higgs-boson mass measurement. *Phys. Rev. D*, 88:053005, Sep 2013.
- [108] Tatsumi Aoyama, Masashi Hayakawa, Toichiro Kinoshita, and Makiko Nio. Complete tenth-order qed contribution to the muon $g-2$. *Phys. Rev. Lett.*, 109:111808, Sep 2012.
- [109] M. Davier, A. Hoecker, B. Malaescu, and Z. Zhang. Reevaluation of the hadronic contributions to the muon g_2 and to $\alpha(m_Z^2)$. *The European Physical Journal C*, 71(1):1515, Jan 2011.
- [110] Kaoru Hagiwara, A. D. Martin, Daisuke Nomura, and T. Teubner. Improved predictions for $g-2$ of the muon and $\alpha(\text{QED})(M^{*2}(Z))$. *Phys. Lett.*, B649:173–179, 2007.
- [111] Joaquim Prades, Eduardo de Rafael, and Arkady Vainshtein. The Hadronic Light-by-Light Scattering Contribution to the Muon and Electron Anomalous Magnetic Moments. *Adv. Ser. Direct. High Energy Phys.*, 20:303–317, 2009.
- [112] G. W. et al. Bennett. Final report of the e821 muon anomalous magnetic moment measurement at bnl. *Phys. Rev. D*, 73:072003, Apr 2006.
- [113] David W. Hertzog. Next Generation Muon g_2 Experiments. *EPJ Web Conf.*, 118:01015, 2016.

- [114] Wesley Gohn. The Muon $g-2$ Experiment at Fermilab. 2017.
- [115] David Bernecker and Harvey B. Meyer. Vector correlators in lattice qcd: Methods and applications. *The European Physical Journal A*, 47(11):148, Nov 2011.
- [116] Anthony Francis, Benjamin Jäger, Harvey B. Meyer, and Hartmut Wittig. New representation of the adler function for lattice qcd. *Phys. Rev. D*, 88:054502, Sep 2013.
- [117] Xu Feng, Shoji Hashimoto, Grit Hotzel, Karl Jansen, Marcus Petschlies, and Dru B. Renner. Computing the hadronic vacuum polarization function by analytic continuation. *Phys. Rev. D*, 88:034505, Aug 2013.